Faculty of Science

Department of Physics

Noisy quantum metrology with mixed spin anticoherent states

Jérémy Dhyon

Supervisor:
Prof. John Martin

Reading Committee:
Prof. Ngoc Duy Nguyen
Dr. François Damanet
Dr. Eric Opsomer

Master's thesis presented in the partial fulfillment of the requirements for the master degree of Science in Physics.

Academic year 2025-2026

Acknowledgements

First and foremost, I would like to express my sincere gratitude to my supervisor, Prof. John Martin, for his invaluable guidance and continuous support throughout this academic year. His expertise, constructive feedback, and thoughtful advice have been essential in shaping the direction of this research and improving the quality of this manuscript. I am deeply grateful for the time he dedicated to discussing ideas, providing valuable insights, and guiding me through the challenges encountered in the course of preparing this master's thesis. His patience and academic rigor have greatly contributed to my learning experience and to the successful completion of this thesis.

I am immensely grateful to Dr. Serrano Ensástiga for his outstanding guidance and clinical expertise, as well as for his continuous interest in my academic progress and his close follow-up of my work throughout the development of this thesis. I am also particularly grateful for the resources and references he provided, which contained crucial information and significantly contributed to the depth and quality of this manuscript.

Appreciation is extended to the members of the reading committee, Prof. Ngoc Duy Nguyen, Dr. François Damanet and Dr. Eric Opsomer, for kindly accepting their role and for taking the time to carefully review this master's thesis.

Special thanks are due to my friends Simon, Floryan, Noah, Thomas and Yara, as well as my family, for their unwavering support, encouragement, and understanding throughout the duration of this work. Their continuous presence and moral support have been invaluable, providing strength and motivation during the most challenging moments of this academic journey. I am deeply grateful for their patience, care, and belief in my abilities, which have greatly contributed to the successful completion of this master's thesis.

Contents

Introduction

In recent years, the pursuit of ever-increasing measurement precision and the development of key emerging quantum technologies have continued to shape our understanding of how physical systems can be harnessed to encode, process, and securely transmit information through carefully engineered quantum protocols. Among the various branches stemming from the realm of quantum science, quantum metrology has recently emerged as a particularly active and promising field whose goal is to exploit uniquely quantum phenomena such as superposition, entanglement, and squeezing to enhance measurement precision beyond the limits imposed by classical physics. High-precision measurements play a fundamental role in advancing our understanding of nature. In particular, they enable increasingly stringent tests of physical theories, allowing scientists to probe the limits of existing models, search for new phenomena, and establish more accurate descriptions of the laws governing the universe.

The central objective of quantum metrology is the estimation of unknown parameters that encode measurable quantities within quantum states. Typical examples include the measurement of phases [1], frequencies [2], magnetic fields [3] and time intervals [4]. For N independent probes, the uncertainty typically scales as $1/\sqrt{N}$, which is known in quantum metrology as the standard quantum limit (SQL). On the other hand, quantum mechanics allows particles to be correlated through entanglement or prepared in squeezed states, whose uncertainty scales as $1/N$, thereby defining the Heisenberg limit (HL). This quadratic improvement over a classical scenario has since motivated extensive research into the identification, characterization, and practical implementation of quantum states capable of serving as metrological resources for quantum protocols.

A particularly important platform for quantum metrology is provided by systems that possess angular momentum degrees of freedom. Collective spin systems naturally arise in a wide variety of physical contexts and applications in quantum metrology, including atomic ensembles [5], trapped ions [6, 7], Bose–Einstein condensates [8] and ensembles of solid-state qubits [9]. The mathematical description of these systems is based on the theory of quantum angular momentum, where quantum states are represented within finite-dimensional Hilbert spaces and are associated with irreducible representations of the SU(2) Lie group. Moreover, quasi-probability distributions on the Bloch sphere, such as the Wigner function and the Husimi Q function, offer powerful insights into their symmetry properties. Consequently, spin systems constitute an ideal framework for studying the interplay between quantum correlations, symmetry, and parameter estimation in several situations, and will form the main physical framework of this work.

Prominent examples of spin states used in quantum metrology include Greenberger-Horne-Zeilinger (GHZ) states, which are used for Ramsey interferometry in atomic clock frequency metrology [10], quantum communication, and cryptography [11], as well as NOON states for Mach-Zehnder and Tweezer interferometry [12, 13] and quantum frequency up-conversion [14]. Spin squeezing, in particular, has become one of the most widely studied indicators of metrological usefulness, as it directly quantifies the redistribution of quantum fluctuations among collective spin components. A notable recent example is its application in gravitational-wave detection at the Laser Interferometer

Gravitational-Wave Observatory (LIGO), where frequency-dependent squeezed states were used to reduce quantum noise and surpass the standard quantum limit for the first time in this field [15], as shown in Figure 1.

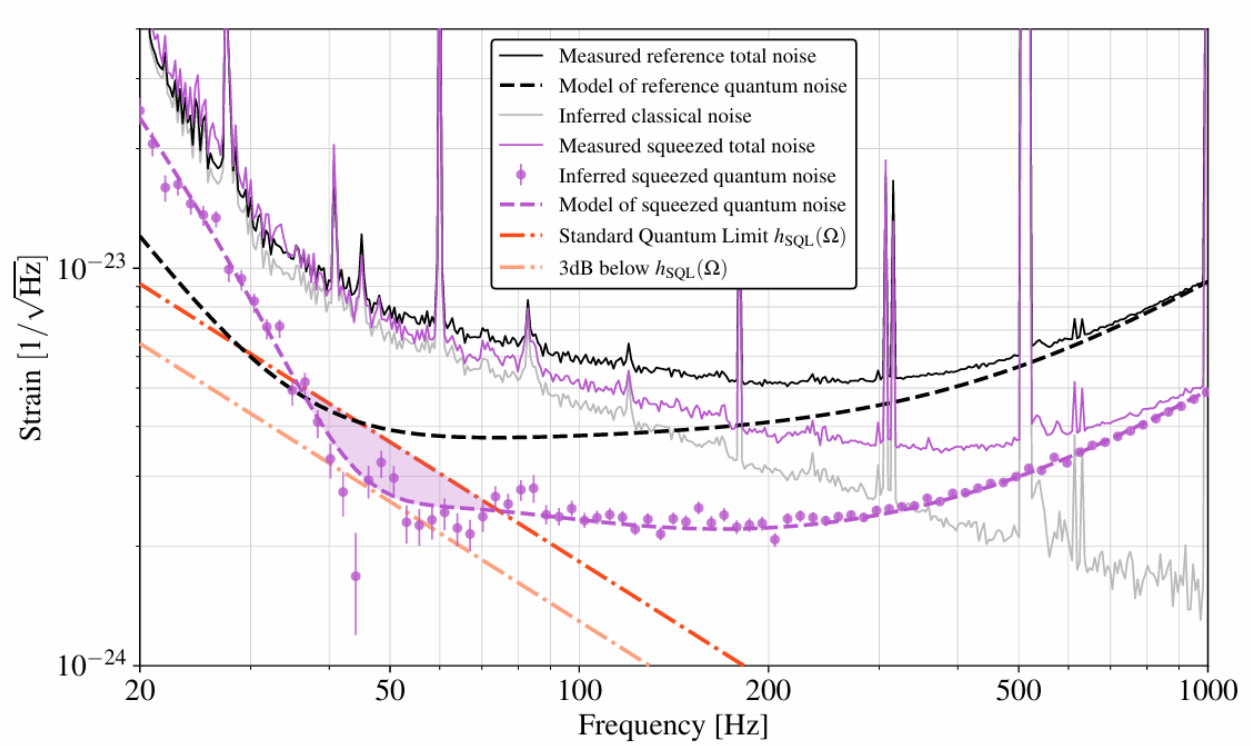

Figure 1: Strain sensitivity of the LIGO L1 interferometer. The total measured detector noise with frequency-dependent squeezing (solid purple) shows a broadband improvement over the unsqueezed reference (solid black). By subtracting the inferred classical noise (gray), the resulting squeezed quantum noise (purple dots) is shown to break the Standard Quantum Limit ($h_{\mathrm{SQL}}(\Omega)$, red dash-dot) by up to 3 dB in the 35–75 Hz band (shaded region). Dashed traces represent the respective quantum noise models, and error bars indicate 1-σ total uncertainty. This figure originates from the original paper of the LIGO collaboration [15].

Furthermore, certain highly symmetric quantum states possess remarkable properties that make them attractive candidates for precision measurements, despite exhibiting little or no conventional spin polarization. Among these states, anticoherent spin states occupy a unique and increasingly important position. These states exhibit an exceptional degree of isotropy, with statistical properties that remain invariant under rotations up to a specified order, implying that expectation values of spin observables do not single out any preferred direction. Beyond their mathematical elegance, anticoherent states possess several features that make them relevant for quantum metrology. In fact, their isotropic nature implies a sensitivity that is distributed uniformly over different spatial directions, contrasting with conventional metrological states that are optimized for estimating parameters along a single preferred axis. Such directional independence is particularly attractive for rotation sensing, specifically in situations where the orientation of the rotation axis is not known a priori [16]. Moreover, it has been shown that anticoherent states serve as optimal rotosensors for infinitesimal rotations in specific settings [17].

The theoretical framework of quantum metrology is fundamentally rooted in estimation the-

ory. The precision achievable in estimating a parameter is constrained by the Cramér–Rao bound (CRB), which relates the variance of an unbiased estimator to the Fisher information. In the quantum domain, the Fisher information is generalized through the quantum Fisher information (QFI), which quantifies the distinguishability of neighboring quantum states generated by infinitesimal parameter variations. The quantum Fisher information provides the ultimate limit achievable by any measurement strategy and serves as a key figure of merit for assessing metrological performance. Consequently, understanding the relationship between anticoherence and the quantum Fisher information has become a central topic in recent investigations.

Recent developments have shifted the focus of quantum metrology from the estimation of single parameters toward more complex tasks involving multiparameter estimation, spatial orientation sensing [18, 19], and high-precision magnetometry [20]. These applications require probe states that provide high sensitivity across multiple directions simultaneously while maintaining robustness against uncertainties in the measurement setting, often induced by various parasitic sources of noise such as decoherence and imperfect state preparation. In this context, the growing interest in anticoherent states has recently emerged as particularly promising resources due to their symmetry-protected structure, which may offer enhanced robustness while retaining significant metrological advantages.

The purpose of this master's thesis is to investigate the role of anticoherent spin states within the framework of noisy quantum metrology and single parameter estimation for rotation sensing problems and spin squeezing, and to establish a link with precision enhancement through the behavior of the quantum Fisher information, when such states are exploited as quantum resources in various configurations of ancilla-assisted protocols in the presence of noise. Although a master's thesis on noisy quantum metrology involving mixed spin states was completed in 2025 [21], the present work was conducted independently to ensure its originality. It focuses primarily on distinct unexplored areas or provides a deeper analysis of shared foundational elements. Furthermore, all numerical codes utilized throughout this study were developed exclusively using the Julia libraries provided by the supervisor at the beginning of the academic year 2025-2026.

This manuscript is organized as follows: Chapter 1 serves as a short reminder of basic concepts in quantum mechanics, notably the notion of quantum states using the density operator formalism. Linear maps and quantum channels are introduced as models to mathematically describe noise mechanisms in quantum protocols. Chapter 2 covers spin systems and spin states, which constitute the fundamental support of this master's thesis. A special treatment is reserved for anticoherence and the mathematical tools of angular momentum theory. Chapter 3 focuses on single parameter estimation theory, providing insight into estimator construction and the quantum Fisher information, as well as the quantum Cramér-Rao bound. Chapter 4 presents noisy quantum metrology, emphasizing the precise role of anticoherent states in this field, as well as optimal and sub-optimal measurement strategies. Chapter 5 aims to numerically investigate rotation sensing protocols and spin squeezing using anticoherent states as probes in order to link this concept to parameter sensitivity encapsulated in the QFI. Finally, chapter 6 addresses multi-parameter estimation with central concepts such as the incompatibility problem and the Holevo Cramér-Rao bound.

Chapter 1

Quantum states and Hilbert spaces

In this chapter, we recall the mathematical objects used in quantum mechanics to describe the quantum states of a multipartite quantum system, as well as operators and linear maps.

Let $\mathcal{H}$ be the Hilbert space associated with the multipartite physical system under investigation, with finite dimension $\dim(\mathcal{H}) \equiv d_{\mathcal{H}}$. This composite system is constructed by combining $N > 1$ subsystems, each endowed with their own Hilbert space $\mathcal{H}_i$ with dimension $\dim(\mathcal{H}_i) \equiv d_{\mathcal{H}_i}$ and $i = 1, \ldots, N$. Mathematically, $\mathcal{H}$ is defined by the tensor product of the Hilbert spaces of each subsystem:

$$\mathcal{H} = \bigotimes_{i=1}^{N} \mathcal{H}_i. \tag{1.0.1}$$

Since the tensor product is associative, one can group several Hilbert spaces appearing in this definition to form larger subsystems; for instance, to reduce the problem to a bipartite system. It is clear from (1.0.1) that the dimension of $\mathcal{H}$ satisfies the product rule $d_{\mathcal{H}} = \prod_{i=1}^{N} d_{\mathcal{H}_i}$. Depending on the value of the dimension $d_{\mathcal{H}}$ of the system, it will be referred to differently. For example, a quantum system with dimension $d_{\mathcal{H}} = 2$ is called a *qubit*, while for $d_{\mathcal{H}} = 3$ and $d_{\mathcal{H}} = 4$, it is respectively called a *qutrit* and a *ququart*. In the general case, a quantum system of finite dimension $d \geq 2$ is referred to as a *qudit*.

1.1 Pure states

A quantum system is said to occupy a *pure state* if it is described by a normalized ket vector $|\psi\rangle \in \mathcal{H}$. The state of a multipartite system can be classified into two categories depending on its nature. Indeed, $|\psi\rangle$ will be called *separable* or a *product state* if it can be brought to the form:

$$|\psi\rangle = |\psi_1\rangle \otimes \ldots \otimes |\psi_N\rangle\,. \qquad (N > 1) \tag{1.1.1}$$

In this specific configuration, it is possible to exclusively describe each of the N subsystems through its corresponding normalized ket vector $|\psi_i\rangle$ for $i = 1, \ldots, N$.

If the physical system under investigation occupies a pure quantum state that cannot be brought to the form (1.1.1), then the ket vector $|\psi\rangle$ is an *entangled* state. In this configuration, it is no longer possible to assign a ket vector to an individual subsystem, which implies that one must treat the entire system in terms of $|\psi\rangle$ instead. This quantum feature has tremendous consequences for the description of a quantum system and is unquestionably one of the most fundamental concepts of quantum mechanics, if not the most fundamental one, as Erwin Schrödinger pointed out in his

original work on quantum entanglement: *"Entanglement is not one but rather the characteristic trait of quantum mechanics."* [22].

1.2 Mixed states

The notion of pure states symbolized by ket vectors introduced in the previous section is entirely sufficient to describe either isolated quantum systems or systems about which we possess complete knowledge. However, in realistic situations, only partial statistical information about the quantum system under investigation is available. Indeed, this situation is frequently encountered in the multipartite setting when the system is embedded in a larger entangled system, and we only have access to a particular subsystem, or when the system is prepared in one of several possible pure states with a certain probability. In these cases, a single ket vector cannot adequately represent the statistical mixture involved, making the density-operator formalism the appropriate framework. Another central motivation stems from physical processes occurring in open quantum systems, which are characterized by interactions with the environment. For example, decoherence or imperfect state preparation naturally leads to a loss of information about the quantum state of the system of interest.

Hence, an alternative and often convenient description of a quantum system can be obtained by introducing the concept of *density operator*. Strictly speaking, a density operator defines any linear operator $\hat{\rho}$ that is semi-definite positive ($\hat{\rho} \geq 0$) and has unit trace ($\mathrm{Tr}(\hat{\rho}) = 1$). The set of density operators naturally defines a subset $\mathcal{D}(\mathcal{H})$ of the set of linear operators $\mathcal{L}(\mathcal{H})$ of the Hilbert space. Throughout this master's thesis, we will adopt the hat notation $\hat{A}$ for linear operators, whereas the notation A will symbolize their matrix representation in an arbitrary orthonormal basis. One can verify that the density operator defines a valid physical observable since its Hermitian nature is automatically granted by its semi-definite positivity condition[1]. Hence, we suppose that the quantum system is prepared in a state $|\psi_i\rangle$ with probability $p_i > 0$ for $i = 1, \ldots, n$, with integer $n > 1$ and probabilities $p_i \in]0, 1[$ such that $\sum_{i=1}^{n} p_i = 1$. The ket vectors $|\psi_i\rangle$ are general in the sense that they must be normalized, but they do not need to be orthogonal to each other. In such a situation, the system is said to occupy a *mixed state* or a *mixture*. The notion of pure states can be recovered simply by considering the case where $n = 1$ and $p_n = 1$. Formally, a mixture is described by a density operator of the form:

$$\hat{\rho} = \sum_{i=1}^{n} p_i \, |\psi_i\rangle \langle\psi_i| \, . \tag{1.2.1}$$

However, we should emphasize that the mixture defined by (1.2.1) is not unique. In fact, it is clear that given a set $\{(|\psi_i\rangle, p_i) \quad i = 1, \ldots, n\}$, a density operator of the form (1.2.1) can be derived effortlessly. On the other hand, it is not possible to map a general density operator to a unique set of pure states with distinct probabilities, as there exists an infinite number of sets that are suitable candidates. Hence, we say that there is no one-to-one correspondence between a set $\{(|\psi_i\rangle, p_i) \quad i = 1, \ldots, n\}$ and a general density operator. Nonetheless, given a density operator, it is always possible to find a generic set that represents the mixture. Additionally, it is worth stressing that computing the trace of $\hat{\rho}^2$ allows us to classify the quantum state depending on its nature. Indeed, let $\{|i\rangle, \quad i = 1, ..., d_{\mathcal{H}}\}$ be an orthonormal basis of $\mathcal{H}$. The *purity* of the state $\hat{\rho}$ is defined as:

$$\mathrm{Tr}(\hat{\rho}^2) = \sum_{i=1}^{n} \langle i|\hat{\rho}^2|i\rangle \leq 1, \tag{1.2.2}$$

[1] Indeed, semi-definite operators represent a subclass of Hermitian operators.

where $\mathrm{Tr}(\hat{\rho}^2) = 1$ holds for any pure state and $\mathrm{Tr}(\hat{\rho}^2) < 1$ for any mixture. The notion of separability of a quantum state is seamless using the density operator formalism. A mixture is called separable if its associated density operator can be written as a convex combination of mixed product states:

$$\hat{\rho} = \sum_{i=1}^{n} p_i \, \hat{\rho}_1^{(i)} \otimes \hat{\rho}_2^{(i)} \otimes \ldots \otimes \hat{\rho}_N^{(i)}, \qquad (N > 1) \tag{1.2.3}$$

with probabilities p_i that fulfill $0 < p_i < 1$ for all $i = 1, \ldots, n$ such that $\sum_{i=1}^{n} p_i = 1$. If we can identify for every component[2] $\hat{\rho}_k^{(i)} = |\psi_k^{(i)}\rangle \langle \psi_k^{(i)}|$, where $|\psi_k^{(i)}\rangle$ is a pure state of the subsystem k with label i, we can write the quantum system as a pure-product decomposition:

$$\hat{\rho} = \sum_{i=1}^{n} p_i \bigotimes_{k=1}^{N} |\psi_k^{(i)}\rangle \langle \psi_k^{(i)}| \,. \qquad (N > 1) \tag{1.2.4}$$

Moreover, the matrix representation of a density operator of a qudit in an arbitrary orthonormal basis $\{|i\rangle \,, \;\; i = 1, ..., d\}$ reads:

$$\rho = \begin{pmatrix} \rho_{11} & \rho_{12} & \rho_{13} & \cdots & \rho_{1d} \\ \rho_{21} & \rho_{22} & \rho_{23} & \cdots & \rho_{2d} \\ \rho_{31} & \rho_{32} & \rho_{33} & \cdots & \rho_{3d} \\ \vdots & \vdots & \vdots & \ddots & \vdots \\ \rho_{d1} & \rho_{d2} & \rho_{d3} & \cdots & \rho_{dd} \end{pmatrix}. \tag{1.2.5}$$

The diagonal entries of this matrix are called populations and they indicate the probability of finding the system in the state $|i\rangle$ for all $i = 1, \ldots, d$, whereas the off-diagonal entries of the matrix are called coherences, and they encode phase relations between basis states. Indeed, these elements are responsible for interference effects. Hence, if these terms vanish, the diagonal matrix represents a classical mixture in that basis.

1.2.1 The spectral decomposition

A canonical form of (1.2.1) can be derived by diagonalizing ρ in a given basis. Indeed, such a procedure yields the so-called *spectral decomposition*:

$$\hat{\rho} = \sum_{k=1}^{d_{\mathcal{H}}} \lambda_k \, |\Psi_k\rangle \langle \Psi_k| \,, \tag{1.2.6}$$

where $\lambda_k \geq 0$ is k-th eigenvalue of $\hat{\rho}$ and $|\Psi_k\rangle$ its corresponding eigenvector for all $k = 1, \ldots, d_{\mathcal{H}}$. The set of eigenvectors $\{|\Psi_k\rangle \,, \;\; k = 1 \ldots, d_{\mathcal{H}}\}$ forms an orthonormal basis of the Hilbert space $\mathcal{H}$ in which ρ is diagonal. By defining the rank $r = \mathrm{rank}(\rho) \leq d_{\mathcal{H}}$ of this state, which corresponds to the number of non-zero eigenvalues λ_k, one may restrict the sum to the range $k = 1, \ldots, r$. Let us now consider a unitary transformation mediated by a unitary operator $\hat{U}(\theta)$ parametrized by a continuous variable θ:

$$\hat{\rho}(\theta) = \hat{U}(\theta) \hat{\rho} \hat{U}^{\dagger}(\theta), \qquad \hat{U}^{\dagger}(\theta) = \hat{U}^{-1}(\theta). \tag{1.2.7}$$

[2] We should stress that this identification does not imply that every subsystem occupies a global pure state, since (1.2.4) defines a classical statistical mixture represented as a weighted sum with probabilities p_i.

Applying this unitary transformation on (1.2.6) yields:

$$\hat{\rho}(\theta) = \sum_{k=1}^{d_{\mathcal{H}}} \lambda_k \hat{U}(\theta) \left|\Psi_k\right\rangle \left\langle\Psi_k\right| \hat{U}^\dagger(\theta). \tag{1.2.8}$$

From this relation, we deduce that (1.2.6) and (1.2.8) share the exact same spectrum of eigenvalues, and that the eigenvectors of this density operator simply correspond to the unitarily transformed eigenvectors of $\hat{\rho}$, such that the spectral decomposition of $\hat{\rho}(\theta)$ reads:

$$\hat{\rho}(\theta) = \sum_{k=1}^{d_{\mathcal{H}}} \lambda_k \left|\Psi_k(\theta)\right\rangle \left\langle\Psi_k(\theta)\right|, \qquad \left|\Psi_k(\theta)\right\rangle = \hat{U}(\theta) \left|\Psi_k\right\rangle. \tag{1.2.9}$$

This result is tremendously useful in numerous cases, namely in parameter estimation theory, when one wishes to diagonalize a parameter family of states that depends on an unknown parameter θ.

1.2.2 The maximally mixed state

A particularly relevant example of a mixed state is the so-called *maximally mixed state* which appears in various analytical derivations in this work. It is defined as:

$$\hat{\rho}_{\mathrm{MM}} = \frac{1}{d_{\mathcal{H}}} \hat{\mathbb{1}}_{d_{\mathcal{H}}}, \tag{1.2.10}$$

where $\hat{\mathbb{1}}_{d_{\mathcal{H}}}$ represents the identity operator in $\mathcal{L}(\mathcal{H})$. This state can be constructed from (1.2.6) by setting $\lambda_k = 1/d_{\mathcal{H}}$ as a uniform weight for every eigenvector and using the completeness relation of the orthonormal basis:

$$\sum_{k=1}^{d_{\mathcal{H}}} \left|\Psi_k\right\rangle \left\langle\Psi_k\right| = \hat{\mathbb{1}}_{d_{\mathcal{H}}}. \tag{1.2.11}$$

In other words, the maximally mixed state is characterized by a total lack of knowledge about the quantum system studied due to high symmetry among all eigenstates. Any measurement outcome is equally probable (due to degeneracy between eigenvalues), regardless of the choice of the orthonormal basis used to represent this state. Additionally, this state has a minimal purity equal to the statistical weight between eigenvectors:

$$\mathrm{Tr}(\hat{\rho}_{\mathrm{MM}}^2) = \frac{1}{d_{\mathcal{H}}}. \tag{1.2.12}$$

Hence, it corresponds to the least pure, or equivalently, the most mixed quantum state in dimension $d_{\mathcal{H}}$, thereby justifying its name.

1.2.3 Reduced states

As previously stated in section 1.1, it is impossible to assign a ket vector to each subsystem of a multipartite system when the overall state is entangled. A key advantage of the density-operator formalism is that it makes it possible to determine the *reduced state* of any subsystem, irrespective of its nature. Indeed, if the multipartite quantum system under investigation occupies a quantum state $\hat{\rho}$, the reduced state of the party $k \in \{1, \ldots, N\}$ is defined as:

$$\hat{\rho}_k = \mathrm{Tr}_{\neg k}(\hat{\rho}) \equiv \mathrm{Tr}_{\{1,\ldots,k-1,k+1,\ldots,N\}}(\hat{\rho}), \tag{1.2.13}$$

where the trace is taken over each subsystem except the k-th party, which essentially means that we ignore the rest of the subsystems. Hence, this reduced state contains all information accessible by measurements strictly performed on the k-th subsystem, without access to any of the other parties. Let $\{|i\rangle_j : \quad i = 1, \ldots, d_{\mathcal{H}_j}\}$ be an orthonormal basis of the subsystem $j \in \{1, \ldots, k-1, k+1, \ldots, N\}$. The trace can be computed in the natural basis of $\mathcal{H}$ using the tensor product of the basis states of each subsystem involved by the partial trace:

$$\hat{\rho}_k = \sum_{i_1=1}^{d_{\mathcal{H}_1}} \cdots \sum_{i_{k-1}=1}^{d_{\mathcal{H}_{k-1}}} \sum_{i_{k+1}=1}^{d_{\mathcal{H}_{k+1}}} \cdots \sum_{i_N=1}^{d_{\mathcal{H}_N}} \langle i_1 \ldots i_{k-1} i_{k+1} \ldots i_N | \hat{\rho} | i_1 \ldots i_{k-1} i_{k+1} \ldots i_N \rangle \,. \tag{1.2.14}$$

However, a consequence of this result is that the reduced state will typically be mixed and thus fail to encode all the information contained in the global system. Moreover, if $\hat{\rho}$ defines a pure state of a multipartite system, the reduced states are generally mixed due to the presence of entanglement.

1.2.4 Mean value and variance of physical observables

According to the postulates of quantum mechanics, any physical observable is represented by a self-adjoint operator $\hat{\mathcal{O}}$. Let the quantum system of interest occupy a generic quantum state $\hat{\rho}$. The mean value of any physical observable $\hat{\mathcal{O}}$ acting on this multipartite system in this state can be defined as:

$$\langle \hat{\mathcal{O}} \rangle_\rho = \mathrm{Tr}(\hat{\mathcal{O}}\hat{\rho}). \tag{1.2.15}$$

This definition holds for any type of quantum state, whether it is pure or mixed. Additionally, the same formalism can be adopted for a *local observable*. The latter is represented by a Hermitian local operator $\hat{\mathcal{O}}_k$ acting solely on the k-th subsystem. The local operator can be written as a global operator using its linear extension acting on the entire system[3]:

$$\hat{\tilde{\mathcal{O}}}_k \equiv \hat{\mathbb{1}}_{\mathcal{H}_1} \otimes \ldots \otimes \hat{\mathbb{1}}_{\mathcal{H}_{k-1}} \otimes \hat{\mathcal{O}}_k \otimes \hat{\mathbb{1}}_{\mathcal{H}_{k+1}} \otimes \ldots \otimes \hat{\mathbb{1}}_{\mathcal{H}_N}, \tag{1.2.16}$$

where $\hat{\mathbb{1}}_{\mathcal{H}_j}$ is the usual identity operator acting on the j-th subsystem with Hilbert space $\mathcal{H}_j$. Thus, equation (1.2.15) can be adapted for local observables using the partial trace on the involved subsystem, as well as its corresponding reduced state $\hat{\rho}_k$:

$$\langle \hat{\mathcal{O}}_k \rangle_{\rho_k} = \mathrm{Tr}_k(\hat{\mathcal{O}}_k \hat{\rho}_k). \tag{1.2.17}$$

Using these definitions, we are now able to compute the variance of an observable in a quantum state $\hat{\rho}$ of the total system using the standard relation:

$$(\Delta_\rho \mathcal{O})^2 = \langle \hat{\mathcal{O}}^2 \rangle_\rho - \langle \hat{\mathcal{O}} \rangle_\rho^2 \,. \tag{1.2.18}$$

The analogous relation for a local observable can be readily derived:

$$(\Delta_{\rho_k} \mathcal{O}_k)^2 = \langle \hat{\mathcal{O}}_k^2 \rangle_{\rho_k} - \langle \hat{\mathcal{O}}_k \rangle_{\rho_k}^2 \,. \tag{1.2.19}$$

[3] We generally omit the tilde notation, as the local nature of the operator is readily deduced from the context.

1.2.5 Linear maps and quantum channels

Linear maps form the mathematical basis of quantum channels used in quantum metrology protocols to map an input state $\hat{\rho}_{in} \in \mathcal{D}(\mathcal{H}_{in})$ to an output state $\hat{\rho}_{out} \in \mathcal{D}(\mathcal{H}_{out})$, where $\mathcal{H}_{in}, \mathcal{H}_{out}$ refers to the Hilbert spaces of the input and output systems, respectively. The precise mathematical structure of this mapping defines the noise mechanism modeled by the channel. Common examples of quantum noise channels include the depolarizing, dephasing, amplitude damping, and bit flip channels [23, 24]. The following material is based on [25].

A *linear map* $\mathcal{E}$ is defined as a linear application:

$$\mathcal{E} : \mathcal{L}(\mathcal{H}_{\text{in}}) \to \mathcal{L}(\mathcal{H}_{\text{out}}) : \hat{A}_{\text{in}} \to \hat{A}_{\text{out}} \equiv \mathcal{E}(\hat{A}_{\text{in}}), \tag{1.2.20}$$

that maps linear operators $\hat{A}_{\text{in}} \in \mathcal{L}(\mathcal{H}_{\text{in}})$ of the input system to linear operators of the output system. This mathematical object is often referred to as a *superoperator* due to its nature. By definition, this linear application verifies:

$$\mathcal{E}(a\hat{A}_{\text{in}} + b\hat{B}_{\text{in}}) = a\mathcal{E}(\hat{A}_{\text{in}}) + b\mathcal{E}(\hat{B}_{\text{in}}), \tag{1.2.21}$$

for all complex scalars $a, b \in \mathbb{C}$ and all linear operators $\hat{A}, \hat{B} \in \mathcal{L}(\mathcal{H})$. Since we will model noise acting on a quantum state of a system, we will now restrict ourselves to the special case where $\mathcal{H}_{in} = \mathcal{H}_{out} = \mathcal{H}$. In order to ensure that the output density operator obtained remains semi-definite positive, we require that linear maps conserve positivity. Hence, a *positive linear map* is defined as:

$$\mathcal{E} : \mathcal{D}(\mathcal{H}) \to \mathcal{D}(\mathcal{H}) : \hat{\rho} \geq 0 \Rightarrow \mathcal{E}(\hat{\rho}) \geq 0, \qquad \forall \hat{\rho} \in \mathcal{D}(\mathcal{H}). \tag{1.2.22}$$

However, this condition is not sufficient to guaranty that quantum states remain semi-definite positive in a multipartite setting. Indeed, this fact can be highlighted using the concept of local linear maps. Let $\mathcal{H} = \bigotimes_{i=1}^{N} \mathcal{H}_i$ be the Hilbert space of an N-partite quantum system. A *local linear map* acting on subsystem k is defined as a linear map $\mathcal{E}_k : \mathcal{L}(\mathcal{H}_k) \to \mathcal{L}(\mathcal{H}_k)$. The corresponding global map $\mathcal{E}^{(k)} : \mathcal{L}(\mathcal{H}) \to \mathcal{L}(\mathcal{H})$ is defined as:

$$\mathcal{E}^{(k)} = \mathcal{I}_1 \otimes \cdots \otimes \mathcal{E}_k \otimes \cdots \otimes \mathcal{I}_N, \tag{1.2.23}$$

where $\mathcal{I}_i$ denotes the identity map acting on $\mathcal{L}(\mathcal{H}_i)$. If $\mathcal{E}_k$ is a positive map, then:

$$\hat{\rho}_k \geq 0 \quad \Rightarrow \quad \mathcal{E}_k(\hat{\rho}_k) \geq 0, \tag{1.2.24}$$

for all $\hat{\rho}_k \in \mathcal{D}(\mathcal{H}_k)$. However, the positivity of the local map $\mathcal{E}_k$ does not imply the positivity of its global counterpart $\mathcal{E}^{(k)}$. Indeed, in general,

$$\hat{\rho} \geq 0 \quad \not\Rightarrow \quad \mathcal{E}^{(k)}(\hat{\rho}) \geq 0, \tag{1.2.25}$$

for $\hat{\rho} \in \mathcal{D}(\mathcal{H})$, since $\hat{\rho}$ may be entangled across subsystems. A key example that highlights this transgression is the *transpose map* $\mathcal{T}$. Indeed, one can verify that this map is positive (since it preserves eigenvalues):

$$\hat{\rho} \geq 0 \quad \Rightarrow \quad \mathcal{T}(\hat{\rho}) \equiv \hat{\rho}^T \geq 0, \tag{1.2.26}$$

but is not necessarily positive since, for example,:

$$(\mathcal{T} \otimes \mathcal{I})(\hat{\rho}_{\Phi_+}) \ngeq 0, \tag{1.2.27}$$

for the Bell state $\hat{\rho}_{\Phi_+} = |\Phi_+\rangle \langle\Phi_+|$, where:

$$|\Phi_+\rangle = \frac{|00\rangle + |11\rangle}{\sqrt{2}}, \tag{1.2.28}$$

in the natural basis formed by the tensor product of the computational bases of the two qubits involved. Therefore, we require that the linear maps applied onto quantum states in a multipartite system satisfy a stronger condition called complete positivity.

A linear map $\mathcal{E} : \mathcal{L}(\mathcal{H}) \to \mathcal{L}(\mathcal{H})$ is *completely positive (CP)* if, for every auxiliary Hilbert space $\mathcal{H}_{\mathrm{R}}$, the extended map $\mathcal{E} \otimes \mathcal{I}_{\mathrm{R}}$ is positive:

$$(\mathcal{E} \otimes \mathcal{I}_{\mathrm{R}})(\hat{\rho}) \geq 0, \qquad \forall \hat{\rho} \geq 0. \tag{1.2.29}$$

Finally, we require linear maps to be trace preserving to ensure that mapped quantum states retain unit trace. Hence, a linear map $\mathcal{E} : \mathcal{L}(\mathcal{H}) \to \mathcal{L}(\mathcal{H})$ is *trace preserving (TP)* if:

$$\mathrm{Tr}(\mathcal{E}(\hat{\rho})) = \mathrm{Tr}(\hat{\rho}), \quad \forall \hat{\rho} \in \mathcal{D}(\mathcal{H}). \tag{1.2.30}$$

A *quantum channel* $\mathcal{E} : \mathcal{L}(\mathcal{H}) \to \mathcal{L}(\mathcal{H})$ is a completely positive and trace preserving linear map (CPTP). These two conditions ensure that quantum channels are physically implementable transformations relating density operators, and they provide the fundamental framework for describing information loss in quantum protocols.

Chapter 2

Spin systems, spin states and angular momentum theory

In 1922, the famous Stern-Gerlach experiment [26] provided the first direct experimental evidence for angular momentum quantization. The experiment showed that a beam of silver atoms passing through a non-uniform magnetic field split into two distinct beams instead of spreading continuously, as classical physics predicted. While originally interpreted as proof of quantized orbital angular momentum, this experiment was later recognized as definitive proof that electrons possess an intrinsic angular momentum called *spin*, independent of any actual motion in space.

The spin of a particle arises from how quantum states transform under the SU(2) symmetry group representations associated with rotational symmetry. It can be understood as an internal degree of freedom that determines how particles interact with each other or with an external magnetic field. According to the spin-statistics theorem, integer values of spin correspond to bosons, whereas half-integer values correspond to fermions.

A *spin system* is a collection of interacting spins that serves as a fundamental model primarily used to explain magnetism and many-body quantum phenomena. Their application in quantum metrology is particularly beneficial, as such systems provide highly sensitive probes of physical quantities such as magnetic fields [27], rotation angles [17], and frequencies [28]. The key idea is to use the dynamics of spin states that are strongly influenced by the surrounding environment. Minor variations in the external environment can produce measurable changes in the collective quantum state. Moreover, correlations and entanglement between spin states enable measurements with unprecedented precision, allowing sensitivities that surpass the so-called shot-noise limit of classical systems and the standard quantum limit for uncorrelated quantum probes [29].

2.1 The qubit

The *qubit* is the fundamental two-level quantum system characterized by a 2-dimensional Hilbert space $\mathcal{H} = \mathbb{C}^2$ and serves as the basic unit of information in quantum computing. It is arguably the simplest imaginable spin system characterized by the smallest spin value $j = 1/2$ and its two possible projections for the magnetic quantum number $m = \pm 1/2$. The most famous example of a qubit in the literature is arguably the electron, which possesses two state configurations for its spin (spin "up" and spin "down", often symbolized by $|\uparrow\rangle$ and $|\downarrow\rangle$). However, a qubit can generally be encoded in a variety of physical systems, including trapped ions [30], superconducting circuits [31], electron spins in quantum dots [32], and neutral atoms [33]. Despite their different physical realizations, these platforms can be engineered to exhibit two-level configurations, commonly labeled

by the computational basis states $|0\rangle$ and $|1\rangle$ in quantum information. The most general pure state describing this two-level system is a superposition of both qubit states:

$$|\phi_{qubit}\rangle = \alpha\,|0\rangle + \beta\,|1\rangle\,, \tag{2.1.1}$$

where $\alpha, \beta \in \mathbb{C}$ both represent the statistical weights associated with each configuration, satisfying the normalization condition $|\alpha|^2 + |\beta|^2 = 1$. Moreover, the Bloch sphere provides a convenient geometric representation of a qubit state and serves as a powerful visualization tool. In such a framework, one often uses the convenient parametrization:

$$|\phi(\theta,\varphi)\rangle = \cos\left(\frac{\theta}{2}\right)|0\rangle + e^{i\varphi}\sin\left(\frac{\theta}{2}\right)|1\rangle\,, \tag{2.1.2}$$

in terms of the polar angle $\theta \in [0,\pi]$ and the azimuthal angle $\varphi \in [0,2\pi]$. Consequently, every qubit state corresponds to a unique point (θ,φ) on the Bloch sphere, as shown in Figure 2.1.

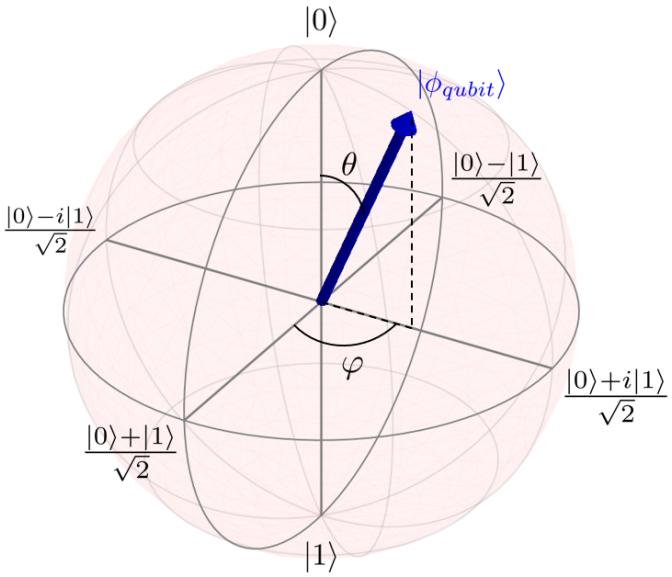

Figure 2.1: Visualization of a qubit state parametrized by the angular values $\theta = \pi/8$ and $\varphi = \pi/2$ on the Bloch sphere, represented by a blue arrow. The north and south poles correspond to the basis states of the computational basis.

Furthermore, the spin observables of this system are described by a set of Hermitian angular momentum operators $\hat{J}_x, \hat{J}_y, \hat{J}_z$ that can be written as:

$$\hat{J}_\alpha = \frac{\hbar}{2}\hat{\sigma}_\alpha, \qquad (\alpha = x, y, z) \tag{2.1.3}$$

using the famous Pauli matrices:

$$\sigma_x = \begin{pmatrix} 0 & 1 \\ 1 & 0 \end{pmatrix}, \qquad \sigma_y = \begin{pmatrix} 0 & -i \\ i & 0 \end{pmatrix}, \qquad \sigma_z = \begin{pmatrix} 1 & 0 \\ 0 & -1 \end{pmatrix}. \tag{2.1.4}$$

From (2.1.3), it can be seen that the angular momentum operators are quantized by units of the reduced Planck constant. Moreover, these operators satisfy the commutation relations:

$$[\hat{J}_\alpha, \hat{J}_\beta] = i\hbar\epsilon_{\alpha\beta\gamma}\hat{J}_\gamma, \tag{2.1.5}$$

for $\alpha, \beta, \gamma = x, y, z$, where $\epsilon_{\alpha\beta\gamma}$ denotes the Levi-Civita symbol. Thus, the angular momentum operators provide a representation of the Lie algebra *su(2)*. Any element of the SU(2) Lie group can be written as:

$$\hat{U}(\mathbf{n}, \theta) = \exp\left(-\frac{i}{\hbar}\theta\, \mathbf{n} \cdot \hat{\mathbf{J}}\right) = \exp\left(-i\frac{\theta}{2}\, \mathbf{n} \cdot \hat{\boldsymbol{\sigma}}\right), \tag{2.1.6}$$

which is a unitary operator describing a rotation of a qubit state with angle θ around an axis $\mathbf{n} \in \mathbb{R}^3$. One can expand the exponential using Taylor series and use the fact that $(\mathbf{n} \cdot \hat{\boldsymbol{\sigma}})^2 = \hat{\mathbb{1}}$ to obtain the simplified form [34]:

$$\hat{U}(\mathbf{n}, \theta) = \cos\left(\frac{\theta}{2}\right)\hat{\mathbb{1}} - i \sin\left(\frac{\theta}{2}\right)(\mathbf{n} \cdot \hat{\boldsymbol{\sigma}}). \tag{2.1.7}$$

From this relation, we deduce that a rotation of angle $\theta = 2\pi$ yields $\hat{U}(\mathbf{n}, 2\pi) = -\hat{\mathbb{1}}$. Consequently, this rotation does not reproduce the original qubit state exactly but instead introduces a global phase factor. However, this has no observable effect since expectation values of physical observables are invariant under global phase transformations. *M.C. Escher's Möbius Strip II*, represented in Figure 2.2, provides a visual analogy for this non-trivial topology elegantly, where a traversal of a non-orientable surface necessitates a double cycle to recover the initial configuration up to orientation.

Figure 2.2: Möbius Strip II by M. C. Escher. In analogy with an ant on a Möbius strip, which must complete two full circuits to recover its initial configuration, a spin-$\frac{1}{2}$ state exhibits 4π periodicity, returning to its original state only after a double rotation [35].

2.2 Spin states in spin-j systems

We now shift our focus towards spin systems with a generic value of the spin j, which will serve as the mathematical support throughout this master's thesis. Unlike a spin-1/2 system such as the qubit, which has only two possible measurement outcomes along a defined axis, a spin-j system has $2j+1$ possible projections of angular momentum, reflecting the dimension of its quantum state space. Hence, these systems naturally generalize qubits to *qudits*, providing higher-dimensional quantum states that can encode more information and exhibit entanglement as well as convoluted dynamics. Physical implementations of spin-j systems are well documented in the literature, with examples including ultracold atomic gases such as spinor Bose–Einstein condensates of rubidium atoms that realize effective spin-1 or spin-2 systems with tunable interactions [36], magnetic ions in materials in condensed matter physics (such as transition metal ions in crystals [37]) that form lattice spin-j systems underpinning phenomena like magnetism, quantum phase transitions, and exotic quantum phases studied in quantum spin models.

2.2.1 The standard angular momentum basis

In the same spirit as for the qubit, spin-j systems are described by angular momentum operators $\hat{J}_x, \hat{J}_y, \hat{J}_z$ that satisfy the commutation relations (2.1.5). Additionally, we can define the total angular momentum operator using these quantities [38]:

$$\hat{J}^2 = \hat{J}_x^2 + \hat{J}_y^2 + \hat{J}_z^2. \tag{2.2.1}$$

One can readily check using (2.1.5) that this operator commutes with every cartesian component $\hat{J}_\alpha$ for $\alpha = x, y, z$:

$$[\hat{J}^2, \hat{J}_\alpha] = 0. \tag{2.2.2}$$

Consequently, the total spin operator $\hat{J}^2$ and one of its components (conventionally $\hat{J}_z$) can be simultaneously diagonalized, thereby sharing eigenstates that compose an orthonormal basis of the Hilbert space of the spin j system, called the *standard angular momentum basis* [38]:

$$\big\{|j,m\rangle\,, \quad \forall m = -j, -j+1, \ldots, j-1, j\big\}, \tag{2.2.3}$$

where j labels the total spin of the system and m its projection along a chosen axis (conventionally z), called the *magnetic quantum number*. Thus, the eigenvalue equations of $\hat{J}_z$ and $\hat{J}^2$ featuring this set of spin states are [38]:

$$\begin{cases} \hat{J}_z\,|j,m\rangle = \hbar m\,|j,m\rangle \\ \hat{J}^2\,|j,m\rangle = \hbar^2 j(j+1)\,|j,m\rangle \end{cases} \tag{2.2.4}$$

for all values of j and m within $-j, \ldots, j$. The standard angular momentum basis states naturally verify the completeness relation:

$$\sum_{m=-j}^{j} |j,m\rangle\,\langle j,m| = \hat{\mathbb{1}}_{2j+1}. \tag{2.2.5}$$

Additionally, using the cartesian components $\hat{J}_x$ and $\hat{J}_y$, it is often convenient to define the following ladder operators as complex linear combinations of both components [38]:

$$\hat{J}_\pm = \hat{J}_x \pm i\hat{J}_y. \tag{2.2.6}$$

Both of these ladder operators are used to interconnect two neighboring states of the standard angular momentum basis by either raising or lowering their magnetic quantum number m by one unit:

$$\hat{J}_{\pm} |j, m\rangle = \hbar\sqrt{j(j+1) - m(m \pm 1)}\, |j, m \pm 1\rangle \,. \tag{2.2.7}$$

2.2.2 Symmetric Dicke states

The *Dicke basis* offers a way to describe a system composed of N spin-$\frac{1}{2}$ particles collectively by grouping them according to their total spin rather than treating each spin individually. Indeed, the Dicke states themselves correspond to highly symmetric configurations with a fixed number of excitations (e.g., a fixed number k of spins pointing "up"), making them especially convenient for describing permutation-invariant systems. Using this approach, many-body problems in quantum mechanics can be greatly simplified by reducing the Hilbert space size from an exponential size of 2^N to a linear size $N+1$. For example, symmetric Dicke states are important in quantum information and metrology due to their multipartite entanglement, which enables enhanced measurement precision [39]. Moreover, symmetric Dicke states provide a natural basis for symmetric spin systems, which could be understood via the Majorana representation. In this framework, spin-j states are associated with sets of points on the Bloch sphere, which can be mapped to complex numbers via stereographic projection. This mapping identifies points on the Bloch sphere with the extended complex plane and is particularly useful for studying anticoherent states through the geometric symmetries of their Majorana constellations.

The symmetric Dicke states were first introduced by Robert H. Dicke in 1954 [40] and correspond to equal superpositions of all N-qubit computational basis states with a fixed number k of excitations. These states are invariant under any particle exchange, and they belong to the fully symmetric subspace of dimension $N+1$. Formally, their definition reads [41–43]:

$$|D_N^{(k)}\rangle = \frac{1}{\sqrt{\binom{N}{k}}} \sum_{\pi \in \mathcal{S}_N} \pi \left(|0\rangle^{\otimes k} |1\rangle^{\otimes (N-k)} \right), \tag{2.2.8}$$

where $\pi \in \mathcal{S}_N$ denotes a permutation of qubits within the permutation group of N particles $\mathcal{S}_N$. The connection between a single spin-j system and a collection of N qubits stems from how angular momentum adds in quantum mechanics. Since each one of the qubits represents a spin-1/2 system on their own, combining N qubits yields a total multipartite Hilbert space $\mathcal{H} = (\mathbb{C}^2)^{\otimes N}$. The latter is decomposed into irreducible subspaces of finite total spin number, ranging either from $j = 0$ or $j = \frac{1}{2}$ up to the maximal value $j = \frac{N}{2}$, which corresponds to a distinguished subspace known as the *fully symmetric subspace* [34]. This particular subspace has dimension $2j + 1 = N + 1$, therefore matching the Hilbert space of a single spin-j particle. Consequently, the key isomorphism arises when one restricts to this fully symmetric subspace, composed of states that are invariant under permutations of qubits, which is exactly isomorphic to the Hilbert space of a single spin-$N/2$ system [34], as shown in Figure 2.3. More concretely, this isomorphism is established by identifying the standard angular momentum basis (2.2.3) with the symmetric Dicke states composed of N qubits (2.2.8). As a matter of fact, the correspondence is made through the identification $m = k - \frac{N}{2}$ between the quantum magnetic number m and the number of excitations k of the Dicke states [34], such that:

$$|D_N^{(k)}\rangle = |j = \frac{N}{2}, m = k - \frac{N}{2}\rangle \,. \tag{2.2.9}$$

This truly establishes a one-to-one correspondence between the set of $N+1$ symmetric Dicke states and the $2j+1$ magnetic sublevels of a single spin-j system. The fully symmetric subspace realizes the irreducible spin-j representation of SU(2), in which the standard commutation relations (2.1.5)

are preserved. The induced representation of the rotation group is generated by the *collective spin operators* [34] that are given by:

$$\hat{J}_x = \frac{\hbar}{2}\sum_{i=1}^{N}\hat{\sigma}_x^{(i)}, \qquad \hat{J}_y = \frac{\hbar}{2}\sum_{i=1}^{N}\hat{\sigma}_y^{(i)}, \qquad \hat{J}_z = \frac{\hbar}{2}\sum_{i=1}^{N}\hat{\sigma}_z^{(i)}. \tag{2.2.10}$$

Within the fully symmetric subspace, the collective spin operators act as the angular momentum operators of a single spin $j = N/2$. The ladder operators $\hat{J}_\pm$ raise and lower the magnetic quantum number m exactly as they do in the standard angular momentum basis.

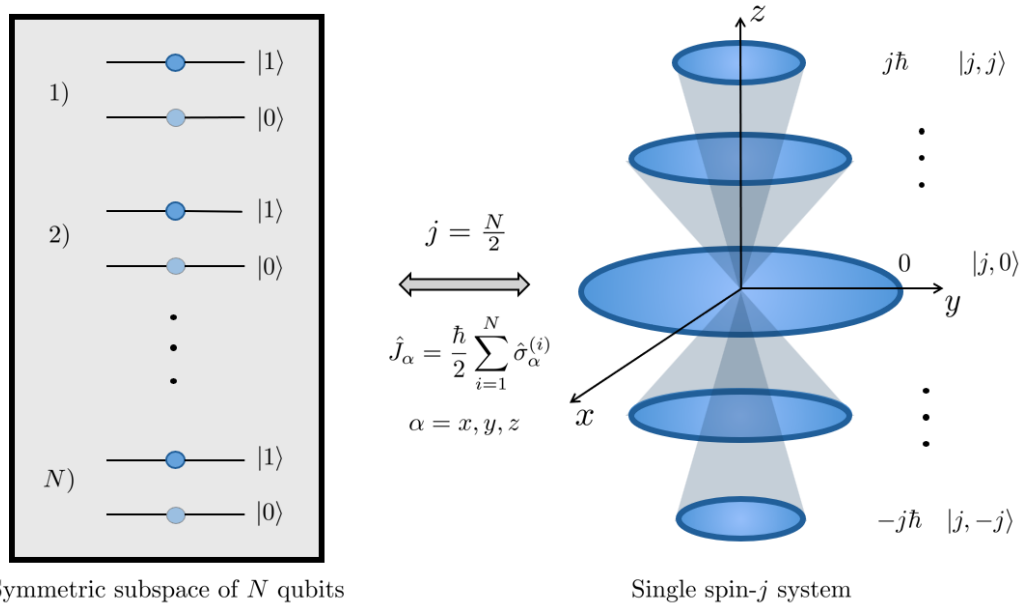

Symmetric subspace of N qubits — Single spin-j system

Figure 2.3: Illustration of the isomorphism between the fully symmetric subspace of a system of N qubits and a single spin-j system. This figure is inspired from [34].

2.2.3 Spin coherent states

Coherent spin states are particular pure quantum states of spin-j systems whose mean value of the spin operator $\hat{\mathbf{J}}$ projection along a given unitary axis $\mathbf{n} \in \mathbb{R}^3$ is maximal. These quantum states are widely used in quantum optics and quantum information and contribute to the definition of the Husimi Q function, as well as their natural opposite counterpart, called anticoherent states. A coherent state $|\mathbf{n}\rangle$ of a spin-j system is defined by the relation [34]:

$$(\mathbf{n}\cdot\hat{\mathbf{J}})\,|\mathbf{n}\rangle = j\,|\mathbf{n}\rangle\,, \qquad |\mathbf{n}| = 1, \tag{2.2.11}$$

where $\mathbf{n} \in \mathbb{R}^3$ is a unit vector defining a chosen axis. The subset of all spin coherent states $\mathcal{S}_{coh} = \{|\mathbf{n}\rangle : \mathbf{n} \in \mathbb{R}^3\}$ forms an overcomplete basis of the Hilbert space $\mathcal{H} = \mathbb{C}^{2j+1}$, which means that coherent states are not-necessarily orthogonal and hence cannot be perfectly distinguished from one another. In fact, their overlap is given by [34]:

$$|\langle\mathbf{n}_1|\mathbf{n}_2\rangle| = \left(\frac{1+\mathbf{n}_1\cdot\mathbf{n}_2}{2}\right)^j. \tag{2.2.12}$$

Additionally, the subset $\mathcal{S}_{coh}$ contains more elements than a regular orthogonal basis of the Hilbert space $\mathcal{H}$. We should emphasize that the definition (2.2.11) for coherent states is not unique. In fact, these states can also be defined using the mean value of angular momentum operators. Indeed, a spin coherent state is a state that satisfies:

$$\langle \hat{J}_x \rangle_{\mathbf{n}}^2 + \langle \hat{J}_y \rangle_{\mathbf{n}}^2 + \langle \hat{J}_z \rangle_{\mathbf{n}}^2 = \hbar^2 j^2, \qquad \langle \hat{J}_\alpha \rangle_{\mathbf{n}} = \langle \mathbf{n} | \hat{J}_\alpha | \mathbf{n} \rangle \,. \tag{2.2.13}$$

Alternatively, we can formulate these relations using the variance of angular momentum operators instead:

$$(\Delta_{\mathbf{n}} J_x)^2 + (\Delta_{\mathbf{n}} J_y)^2 + (\Delta_{\mathbf{n}} J_z)^2 = \hbar^2 j, \qquad (\Delta_{\mathbf{n}} J_\alpha)^2 = \langle \hat{J}_\alpha^2 \rangle_{\mathbf{n}} - \langle \hat{J}_\alpha \rangle_{\mathbf{n}}^2 \,. \tag{2.2.14}$$

Hence, based on (2.2.13) and (2.2.14), it is clear that spin coherent states are specific states of spin-j systems that maximize the angular momentum operator $\hat{\mathbf{J}}$ and minimize the variance along a specific direction $\mathbf{n}$. Moreover, we can show that coherent states saturate the Heisenberg uncertainty relation for a triad of angular momentum operators oriented in a particular frame, thereby attaining the minimum uncertainty $\frac{1}{2}\hbar^2 j$. This result, combined with (2.2.13) and (2.2.14), highlight the fact that spin coherent states are generally regarded as the "most classical" pure quantum states for a spin system.

We can take advantage of the fact that the highest-weight state $|j, j\rangle$ points in the z-axis direction in order to construct any spin coherent state. Indeed, in the spherical coordinate system, the unit vector $\mathbf{n} = (\sin\theta\cos\varphi, \sin\theta\sin\varphi, \cos\theta)$ is specified by the polar and azimuthal angles (θ, φ). Hence, in this coordinate system, we can map $|j, j\rangle$ to any coherent spin state $|\mathbf{n}\rangle \equiv |\theta, \varphi\rangle$ simply by applying a rotation:

$$|\theta, \varphi\rangle = e^{-\frac{i}{\hbar}\theta(\mathbf{n}_\perp \cdot \hat{\mathbf{J}})} \, |j, j\rangle \,, \qquad (\mathbf{n}_\perp \cdot \mathbf{e}_z) = 0. \tag{2.2.15}$$

This transformation is visually represented in Figure 2.4:

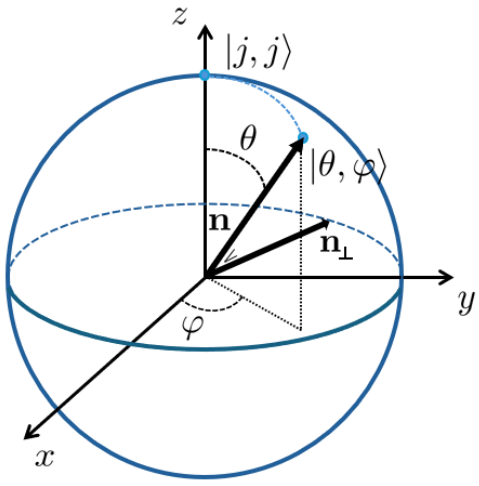

Figure 2.4: Visualization of the coherent spin state $|\theta, \varphi\rangle$ on the unit sphere $\mathcal{S}^2$, resulting from a rotation of angle θ of the highest-weight spin state $|j, j\rangle$ around the axis $\mathbf{n}_\perp$.

where $\mathbf{n}_\perp \in \mathbb{R}^3$ is a unit vector orthogonal to the z-axis (and to $\mathbf{n}$), which specifies the axis about which the system is rotated by an angle θ. Moreover, any coherent spin state can be expanded in the standard angular momentum basis [34]:

$$|\theta,\varphi\rangle = \sum_{m=-j}^{j} \binom{2j}{j+m}^{1/2} \left(\cos\frac{\theta}{2}\right)^{j+m} \left(\sin\frac{\theta}{2}\right)^{j-m} e^{-i(j-m)\varphi} |j,m\rangle\,. \tag{2.2.16}$$

Finally, these states satisfy the completeness relation:

$$\frac{2j+1}{4\pi}\int_{\mathcal{S}^2} |\theta,\varphi\rangle\langle\theta,\varphi| \sin\theta\, d\theta\, d\varphi = \hat{\mathbb{1}}_d, \tag{2.2.17}$$

where $d = 2j+1$ denotes the dimension of the Hilbert space $\mathcal{H} = \mathbb{C}^{2j+1}$. Spin coherent states may also be denoted as $|\Omega\rangle \equiv |\theta,\varphi\rangle$ using the solid angle Ω. A famous example in literature that represents a superposition of spin coherent states is the *spin cat state* [34]:

$$|\psi_{cat}\rangle = \frac{1}{\sqrt{2}}\left(|\Omega\rangle \ + |\overline{\Omega}\rangle\right), \tag{2.2.18}$$

where $|\overline{\Omega}\rangle \equiv |\pi-\theta,\varphi+\pi\rangle$ denotes the antipodal point of $|\Omega\rangle$, which corresponds to the state pointing in the opposite direction $-\mathbf{n}$ on the $\mathcal{S}^2$ sphere.

2.3 Mathematical tools of angular momentum theory

This section introduces and defines several mathematical tools that will simplify the otherwise cumbersome expressions appearing in the intensive derivation of the quantum Fisher information in ancilla-assisted quantum protocols in the presence of noise, and that will further be used to define, visualize, and characterize the concept of anticoherence and its symmetries, which constitute a central theme of this master's thesis.

2.3.1 The Wigner D-matrix

The *Wigner D-matrix* was introduced by Eugene Wigner [44, 45] to describe rotations in irreducible representations of SU(2) and SO(3) groups, providing a means to compute the transformation of the standard angular momentum basis states $|j,m\rangle$ under Euler angle rotations. The letter "D" appearing in the appellation refers to *Darstellung*, which is the German term for "representation". In this context, we consider a global rotation operator with Euler angles (α,β,γ) formally defined as [46]:

$$\hat{\mathcal{R}}(\alpha,\beta,\gamma) = \hat{R}_z(\alpha)\hat{R}_y(\beta)\hat{R}_z(\gamma) = e^{-\frac{i}{\hbar}\alpha\hat{J}_z} e^{-\frac{i}{\hbar}\beta\hat{J}_y} e^{-\frac{i}{\hbar}\gamma\hat{J}_z}, \tag{2.3.1}$$

where $\hat{R}_z(\alpha), \hat{R}_y(\beta)$ and $\hat{R}_z(\gamma)$ define unitary standard rotation operators. This choice of ordering for rotation operators defines the so-called ZYZ convention of the D-matrix. The Euler angles are taken to lie in the following ranges:

$$0 \le \alpha < 2\pi, \qquad 0 \le \beta < \pi, \qquad 0 \le \gamma < 2\pi. \tag{2.3.2}$$

Using the global rotation operator (2.3.1), one can define the D-matrix by its elements $D^{j}_{m',m}(\alpha,\beta,\gamma)$ in the standard angular momentum basis[1]:

$$D^{(j)}_{m',m}(\alpha,\beta,\gamma) = \langle j,m'|\hat{\mathcal{R}}(\alpha,\beta,\gamma)|j,m\rangle = e^{-im'\alpha} d^{(j)}_{m',m}(\beta) e^{-im\gamma}, \tag{2.3.3}$$

[1]Note that, in the general case of different total spin quantum numbers $j \neq j'$, an additional constraint appears in the form of a Kronecker delta: $\langle j',m'|\hat{\mathcal{R}}(\alpha,\beta,\gamma)|j,m\rangle = \delta_{j,j'} D^{(j)}_{m',m}(\alpha,\beta,\gamma)$.

where $d^{j}_{m',m}(\beta) = D^{j}_{m',m}(0,\beta,0)$ denotes the *small d-matrix* [47]:

$$d^{(j)}_{m',m}(\beta) = \langle j, m'|e^{-\frac{i}{\hbar}\beta \hat{J}_y}|j,m\rangle\,. \tag{2.3.4}$$

The elements of this matrix can be written using Wigner's formula (We refer the reader to the Appendix A for a detailed derivation of this formula)[47]:

$$d^{(j)}_{m',m}(\beta) = \sum_{k=k_{min}}^{k_{max}} c^{(j,k)}_{m',m} \left(\cos\frac{\beta}{2}\right)^{2j-2k+m-m'} \left(\sin\frac{\beta}{2}\right)^{2k-m+m'}, \tag{2.3.5}$$

where we defined the real coefficients:

$$c^{(j,k)}_{m',m} = (-1)^{k-m+m'} \frac{\sqrt{(j+m)!(j-m)!(j+m')!(j-m')}}{(j+m-k)!(j-k-m')!(k-m+m')!k!}. \tag{2.3.6}$$

The range of the index k appearing in the sum of (2.3.5) for the matrix elements is determined by the maximum and minimum values:

$$k_{min} = \max(0, m-m'), \qquad k_{max} = \min(j+m, j-m'). \tag{2.3.7}$$

From (2.3.5) and (2.3.6), we deduce that the d-matrix has only real elements for all values of the spin number j and magnetic quantum numbers m, m'. This is a direct consequence of the application of (2.2.6) and (2.2.7). Moreover, the small d-matrix exhibits several additional interesting properties [46, 47]:

1. Angle inversion symmetry: $d^{(j)}_{m',m}(-\beta) = d^{(j)}_{m,m'}(\beta)$
2. Magnetic parity: $d^{(j)}_{m',m}(\beta) = d^{(j)}_{-m',-m}(\beta)$
3. Transpose symmetry: $d^{(j)}_{m',m}(\beta) = (-1)^{m-m'} d^{(j)}_{m,m'}(\beta)$
4. Reflection symmetry: $d^{(j)}_{m',m}(\pi-\beta) = (-1)^{j-m} d^{(j)}_{m',-m}(\beta)$
5. Evaluation at $\beta = 0$: $d^{(j)}_{m',m}(0) = \delta_{m,m'}$

for all values of the spin number j and magnetic quantum numbers m, m'.

The inverse of the collective rotation operator $\hat{\mathcal{R}}(\alpha,\beta,\gamma)$ can be easily computed since it defines a unitary operator:

$$\hat{\mathcal{R}}^{-1}(\alpha,\beta,\gamma) = \hat{\mathcal{R}}^{\dagger}(\alpha,\beta,\gamma). \tag{2.3.8}$$

Hence, we deduce the following relation for the elements of the D-matrix:

$$(D^{-1})^{(j)}_{m',m}(\alpha,\beta,\gamma) = D^{(j)*}_{m,m'}(\alpha,\beta,\gamma). \tag{2.3.9}$$

Furthermore, the Wigner D-matrix verifies several properties [46]:

1. Orthogonality relation:

$$\int_0^{2\pi} d\alpha \int_0^{\pi} \sin\beta d\beta \int_0^{2\pi} d\gamma D^{(j)*}_{m',m}(\alpha,\beta,\gamma) D^{(j')}_{k',k}(\alpha,\beta,\gamma) = \frac{8\pi^2}{2j+1}\delta_{m,k}\delta_{m',k'}\delta_{j,j'}. \tag{2.3.10}$$

2. Unitarity relation:

$$\sum_{m''=-j}^{j} D^{(j)}_{m',m''}(\alpha,\beta,\gamma)D^{(j)*}_{m,m''}(\alpha,\beta,\gamma) = \delta_{m,m'}, \qquad \det||D^{(j)}_{m',m}(\alpha,\beta,\gamma)|| = 1. \tag{2.3.11}$$

3. Complex conjugation:

$$D^{(j)*}_{m',m'}(\alpha,\beta,\gamma) = (-1)^{m'-m} D^{(j)}_{-m',-m}(\alpha,\beta,\gamma). \tag{2.3.12}$$

4. Relation to spherical harmonics:

$$D^{(l)}_{m',0}(\alpha,\beta,0) = \sqrt{\frac{4\pi}{2l+1}} Y_l^{(m')*}(\beta,\alpha), \qquad -l \leq m \leq l \quad (l \in \mathbb{N}). \tag{2.3.13}$$

A particularly important case, which will prove useful in the analytical derivations of Chapter 5, corresponds to setting all three Euler angles equal to zero:

$$D^{(j)}_{m',m}(0,0,0) = \delta_{m,m'}, \tag{2.3.14}$$

which is a direct consequence of the orthogonality property of the standard spin basis.

2.3.2 The Majorana representation

The *Majorana representation* [48] provides a geometric visualization on the Bloch sphere of symmetric states composed of N qubits. It maps pure states of a spin-j system (equivalent to the fully symmetric subspace of $N = 2j$ qubits), to a constellation (known as the *Majorana constellation*) of N points called *Majorana stars*. For spin states, and in particular anticoherent states, the Majorana representation provides a powerful geometric reformulation of otherwise abstract constraints on angular momentum moments, mapping them to a problem on the sphere and enabling a clear visualization of their symmetries. This construction relies on the fact that any symmetric N-qubit state $|\psi_N^{\text{sym}}\rangle$ can be written as [49]:

$$|\psi_N^{\text{sym}}\rangle = \mathcal{N} \sum_{k=1}^{N_P} (|\phi_{\pi_k(1)}\rangle \otimes |\phi_{\pi_k(2)}\rangle \otimes \ldots \otimes |\phi_{\pi_k(N)}\rangle), \tag{2.3.15}$$

where $N_P = N!$ is the total number of permutations π_k $(\forall k \in \{1,\ldots,N_P\})$ of the symmetric permutation group $\mathcal{S}_N$ of N elements, and the ket vectors $|\phi_j\rangle$ $(\forall j \in \{1,\ldots,N\})$ represent qubit states with the same parametrization as (2.1.2). Hence, each of the N qubit states appearing in (2.3.15) unequivocally defines a point $\Omega_j \equiv (\theta_j, \varphi_j)$ on the Bloch sphere. In other words, the symmetric state considered can be represented by a set of N points $\{\Omega_j,\ \forall j = 1,\ldots,N\}$ on the Bloch sphere called Majorana stars, which together form the Majorana constellation. In order to gain insight into the intrinsic geometric properties of the Majorana representation, we first expand the symmetric state $|\psi_N^{\text{sym}}\rangle$ in the Dicke basis composed of N qubits:

$$|\psi_N^{\text{sym}}\rangle = \sum_{l=0}^{N} c_l \, |D_N^{(l)}\rangle = \sum_{l=0}^{N} c_l \, |\frac{N}{2}, l - \frac{N}{2}\rangle \, . \tag{2.3.16}$$

Hence, this state is completely defined by the set of complex coefficients $\{c_l,\ \forall l \in \{0,\ldots,N\}\}$. A key idea underlying this concept is the equivalence between the set of coefficients c_l in (2.3.16) and

the set of points $\Omega_j \equiv (\theta_j, \varphi_j)$ in (2.3.15). Finding an adequate mapping can be done in an elegant manner through the following process, which is based on [34, 49]. First, we note from (2.3.15) that symmetric spin states can be mapped to each other by applying identical rotations of angle $\Omega = (\theta, \varphi)$ on the qubit states composing them, using a rotation operator $\hat{R}(\Omega)$, which ultimately amounts to an equivalent collective rotation mediated by an operator $\hat{\mathcal{R}}(\Omega)$ on the state (2.3.16) in the corresponding $(N+1)$-dimensional symmetric subspace:

$$\hat{\mathcal{R}}(\Omega) = \underbrace{\hat{R}(\Omega) \otimes \hat{R}(\Omega) \otimes \ldots \otimes \hat{R}(\Omega)}_{N \text{ times}} \equiv \bigotimes_{j=1}^{N} \hat{R}(\Omega). \tag{2.3.17}$$

For each of the N qubit states, there exists a corresponding rotation $\hat{R}^{-1}(\Omega_j)$ that maps the j-th qubit state to the north pole state of the Bloch sphere, indicated by the ket vector $|0\rangle$:

$$\hat{R}^{-1}(\Omega_j)\,|\phi_j(\Omega_j)\rangle = |0\rangle\,, \qquad j \in \{1, \ldots, N\}. \tag{2.3.18}$$

Hence, one can rotate, for example, the k-th qubit in (2.3.15), such that the overlap of the rotated symmetric spin state with the Dicke state $|D_N^{(N)}\rangle = |\frac{N}{2}, \frac{N}{2}\rangle$ with N excitations vanishes due to orthogonality:

$$\langle D_N^{(N)}|\hat{\mathcal{R}}(\Omega)|\psi_N^{\text{sym}}\rangle = 0, \qquad |D_N^{(N)}\rangle \equiv |1\rangle^{\otimes N}\,. \tag{2.3.19}$$

Hence, using the expansion (2.3.16) of $|\psi_N^{\text{sym}}\rangle$ in the standard angular momentum basis, we obtain:

$$\langle D_N^{(N)}|\hat{\mathcal{R}}^{-1}(\Omega)|\psi_N^{\text{sym}}\rangle = \sum_{l=0}^{N} c_l\, \langle \frac{N}{2}, \frac{N}{2}|\hat{\mathcal{R}}^{-1}(\Omega)|\frac{N}{2}, l - \frac{N}{2}\rangle\,. \tag{2.3.20}$$

We can now make use of the general form of the collective rotation operator $\hat{\mathcal{R}}(\Omega) = \hat{\mathcal{R}}_z(\varphi)\hat{\mathcal{R}}_y(\theta)$ and its unitary property in order to obtain:

$$\langle D_N^{(N)}|\hat{\mathcal{R}}^{-1}(\Omega)|\psi_N^{\text{sym}}\rangle = \sum_{l=0}^{N} c_l\, \langle \frac{N}{2}, \frac{N}{2}|\hat{\mathcal{R}}_y(-\theta)\hat{\mathcal{R}}_z(-\varphi)|\frac{N}{2}, l - \frac{N}{2}\rangle\,, \tag{2.3.21}$$

from which we can identify the Wigner D-matrix:

$$\begin{aligned} D^{N/2}_{N/2,l-N/2}(0, -\theta, -\varphi) &= \langle \frac{N}{2}, \frac{N}{2}|\hat{\mathcal{R}}_y(-\theta)\hat{\mathcal{R}}_z(-\varphi)|\frac{N}{2}, l - \frac{N}{2}\rangle \\ &= d^{N/2}_{N/2,l-N/2}(-\theta)e^{i(l-\frac{N}{2})\varphi}. \end{aligned} \tag{2.3.22}$$

Using Properties 1 and 3 of the small d-matrix, we can write the inner product (2.3.19) as:

$$\sum_{l=0}^{N}(-1)^{N-l}\, c_l\, d^{N/2}_{N/2,l-N/2}(\theta)\, e^{i(l-\frac{N}{2})\varphi} = 0. \tag{2.3.23}$$

One can explicitly compute the small d-matrix elements where only one term remains in (2.3.5). Algebraic manipulations yield the simplified form:

$$d^{N/2}_{N/2,l-N/2}(\theta) = \binom{N}{l}^{1/2} \left(\cos\frac{\theta}{2}\right)^{l} \left(\sin\frac{\theta}{2}\right)^{N-l}. \tag{2.3.24}$$

Hence, (2.3.19) is essentially transformed into:

$$\mathcal{A}\sum_{l=0}^{N}(-1)^l c_l \binom{N}{l}^{1/2}\left(\cot\frac{\theta}{2}\right)^l e^{il\varphi}=0, \tag{2.3.25}$$

where $\mathcal{A}=\left(-e^{-i\frac{N}{2}\varphi}\cos\frac{\theta}{2}\right)^N$ is a complex multiplicative factor. The problem thus reduces to finding the roots of the *Majorana polynomial* of degree N:

$$P(z)=\sum_{l=0}^{N}(-1)^l c_l \binom{N}{l}^{1/2} z^l, \tag{2.3.26}$$

where we introduced the complex variable $z=\cot\left(\frac{\theta}{2}\right)e^{i\varphi}$ known as the *stereographic projection*. By virtue of the fundamental theorem of algebra, this polynomial has N complex roots z_i, which define the Majorana stars through the mapping:

$$z_i=\cot\left(\frac{\theta_i}{2}\right)e^{i\varphi_i}, \qquad \forall i=1,\dots,N. \tag{2.3.27}$$

The entire set of these complex roots unequivocally defines the symmetric state $|\psi_N^{\text{sym}}\rangle$, defining the Majorana representation. For reference, Figure 2.5 displays the Majorana constellation and the stereographic projections of the Majorana stars for the spin cat state (2.2.18) for a spin $j=3/2$.

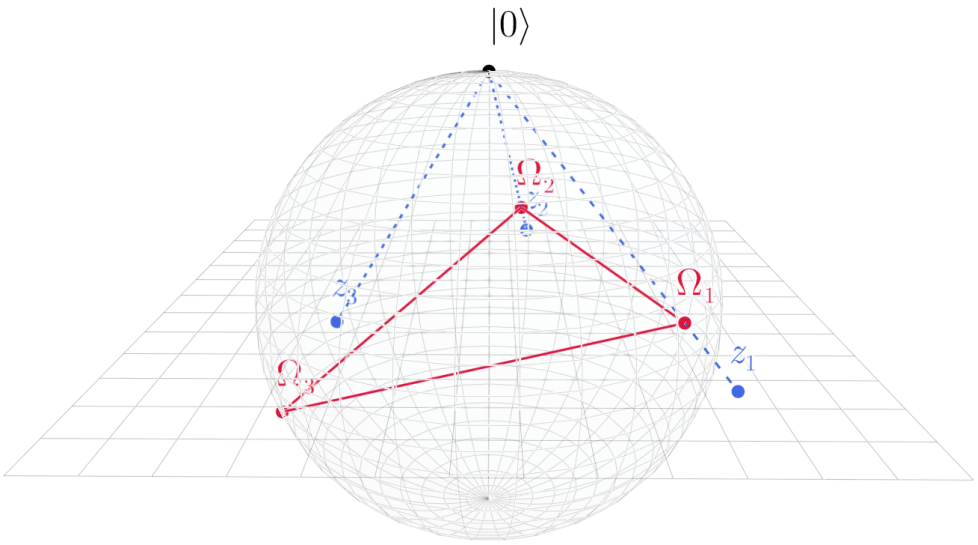

Figure 2.5: Majorana constellation of a spin-3/2 cat state (2.2.18) for the angular values $\theta=\pi/8, \varphi=\pi/4$, represented on the Bloch sphere. The three Majorana stars are labeled by Ω_i, and their stereographic projections are represented on the equatorial complex plane by the complex numbers z_i. The north pole is highlighted in black by the ket vector $|0\rangle$.

2.3.3 The spin tensor multipolar basis

In quantum angular momentum theory, *the spin tensor multipolar basis (STMB)* is an operator basis constructed by irreducible tensor operators acting on a spin-j Hilbert space. It constitutes the operator analogue of the standard angular momentum basis formed by the spin states $|j,m\rangle$,

providing a classification of spin operators according to their behavior under rotations. In fact, this basis is widely used to describe spin states, as it reveals their angular structure and highlights their symmetries within a natural mathematical framework.

Hence, for a spin-j system with Hilbert space $\mathcal{H} = \mathbb{C}^{2j+1}$, the spin tensor multipolar basis is defined by a collection of irreducible tensor operators $\hat{\mathbf{T}}_L$ of rank $L \in \{0, 1, \ldots, 2j\}$, each containing $2j + 1$ elements called polarization operators $\hat{T}_{LM}$, where $M \in \{-L, \ldots, L\}$. Essentially, they represent linearly independent $(2j+1)\times(2j+1)$ matrices that transform under a rotation, such that their respective rank is invariant. Such operators can be fully determined based on the requirements [46]:

1. Commutation relations with the spherical angular momentum operators:

$$[\hat{J}_z, \hat{T}_{LM}] = \hbar M \hat{T}_{LM}, \qquad [\hat{J}_\pm, \hat{T}_{LM}] = \hbar\sqrt{L(L+1) - M(M \pm 1)}\hat{T}_{LM\pm1}. \tag{2.3.28}$$

2. The orthonormalization condition:

$$\mathrm{Tr}\left(\hat{T}^\dagger_{LM}\hat{T}_{L'M'}\right) = \delta_{LL'}\delta_{MM'}. \tag{2.3.29}$$

3. The phase factor relation:

$$\hat{T}_{LM} = (-1)^M \hat{T}^\dagger_{L-M}. \tag{2.3.30}$$

Hence, any operator $\hat{\mathcal{O}}$ can be formally expanded in the STMB using the polarization operators. We will focus in particular on the case of quantum states $\hat{\rho}$, which can be written as [41]:

$$\hat{\rho} = \sum_{L=0}^{2j}\sum_{M=-L}^{L} \rho_{LM}\hat{T}_{LM}, \tag{2.3.31}$$

where the coefficients ρ_{LM} are called *multipoles* and are associated with moments of rank L. They can be computed according to:

$$\rho_{LM} = \mathrm{Tr}\left(\hat{T}^\dagger_{LM}\hat{\rho}\right). \tag{2.3.32}$$

Since $\hat{\rho}$ defines a physical observable, we have the additional relation:

$$\rho_{LM} = (-1)^M \rho^*_{L-M}. \tag{2.3.33}$$

The multipole expansion (2.3.31) separates operator content according to rotational symmetry into terms of monopole, dipole, quadrupole, and higher-order L-moments. This is in close analogy to classical electrodynamics for a charged distribution $\rho(\mathbf{r})$ [34]. In fact, the spin tensor multipolar basis allows us to explore the angular structure of a quantum state of a spin j system by fragmenting it into components of increasing angular complexity.

From Table 2.1, it can be seen that, similarly to its classical counterpart, the monopole captures the isotropic part of the state since the latter is proportional to the identity operator. Similarly, the dipole can be seen as the quantum analogue of the dipole moment, since the rank-1 polarization operators are linear in the cartesian components of the angular momentum operator and can therefore be associated with the expectation value of $\hat{\mathbf{J}}$. Thus, the net orientation of the spin is encapsulated in this term. Finally, rank-2 polarization operators contain the anisotropic part of spin fluctuations in terms of the variance of the total angular momentum operator. Higher-rank polarization operators (and tensors) represent progressively higher-order angular correlations and

Rank	Multipole	Polarization operators	
$L=0$	Monopole	$\hat{T}_{00}=\mathcal{N}_0\hat{\mathbb{1}}$	$(M=0)$
$L=1$	Dipole	$\hat{T}_{10}=\mathcal{N}_1\hat{J}_z$	$(M=0)$
		$\hat{T}_{1\pm1}=\pm\frac{1}{\sqrt{2}}\mathcal{N}_1\hat{J}_\pm$	$(M=\pm1)$
$L=2$	Quadrupole	$\hat{T}_{20}=\mathcal{N}_2\left(3\hat{J}_z^2-j(j+1)\hat{\mathbb{1}}\right)$	$(M=0)$
		$\hat{T}_{2\pm1}=\mp\sqrt{\frac{3}{2}}\mathcal{N}_2\{\hat{J}_z,\hat{J}_\pm\}$	$(M=\pm1)$
		$\hat{T}_{2\pm2}=\sqrt{\frac{3}{2}}\mathcal{N}_2\hat{J}_\pm^2$	$(M\pm2)$

Table 2.1: Irreducible tensor polarization operators up to rank $L=2$, with the normalization factors $\mathcal{N}_0=\frac{1}{\sqrt{2j+1}}$, $\mathcal{N}_1=\sqrt{\frac{3}{j(j+1)(2j+1)}}$, and $\mathcal{N}_2=\sqrt{\frac{5}{j(2j+3)(j+1)(2j-1)}}$.

finer structure in the quantum spin distribution, such as skewness-like asymmetry or kurtosis-like shape anisotropy [34]. These higher-rank components of the spin tensor multipolar basis are relatively small for the quasi-classical spin coherent states, but become significant for non-classical states such as spin cat states or anticoherent states. Furthermore, the polarization operators can be expanded in the standard angular momentum basis according to:

$$\hat{T}_{LM}=\sqrt{2L+1}\sum_{m,m'=-j}^{j}(-1)^{j-m}\begin{pmatrix}j & L & j\\ -m & M & m'\end{pmatrix}|j,m'\rangle\langle j,m|\,, \tag{2.3.34}$$

which involves the Wigner $3j$ symbol. Alternatively, this definition can be formulated using the compact Clebsch-Gordan form [41]:

$$\hat{T}_{LM}=\sqrt{\frac{2L+1}{2j+1}}\sum_{m,m'=-j}^{j}C^{jm'}_{jm,LM}\,|j,m'\rangle\langle j,m|\,, \tag{2.3.35}$$

where we used the identification for the Clebsch-Gordan coefficients:

$$C^{jm'}_{jm,LM}\equiv\langle jm',LM|jm\rangle=(-1)^{j-m}\sqrt{2j+1}\begin{pmatrix}j & L & j\\ -m & M & m'\end{pmatrix}. \tag{2.3.36}$$

Moreover, we can derive the irreducible polarization operators using solid spherical harmonics [46]:

$$\hat{T}_{LM}=\mathcal{N}_L^{(j)}(\hat{\mathbf{J}}\cdot\boldsymbol{\nabla})^L(r^LY_{LM}(\theta,\varphi)), \tag{2.3.37}$$

where we denoted by $\mathcal{N}_L^{(j)}$ the normalization prefactor:

$$\mathcal{N}_L=\frac{2^L}{L!}\sqrt{\frac{4\pi(2j-L)!}{(2j+L+1)!}}. \tag{2.3.38}$$

We should emphasize that although (2.3.37) depends on the radial spherical coordinate r on the right-hand side, the polarization operators are independent of this coordinate. Under a rotation

characterized by the usual Euler angles α, β, γ, the irreducible polarization operators transform according to the Wigner D-matrix [46]:

$$\hat{T}'_{LM'} = D(\alpha,\beta,\gamma)\hat{T}_{LM'}\left(D(\alpha,\beta,\gamma)\right)^{-1} = \sum_{M=-L}^{L} D^{(j)}_{M',M}(\alpha,\beta,\gamma)\hat{T}_{LM}. \tag{2.3.39}$$

Moreover, the product of two irreducible polarization operators can be decomposed in the spin tensor multipolar basis as [46]:

$$\hat{T}_{L_1M_1}\hat{T}_{L_2M_2} = \sum_{L=0}^{2j}\sum_{M=-L}^{L}(-1)^{2j+L}\sqrt{(2L_1+1)(2L_2+1)}\begin{Bmatrix} L_1 & L_2 & L \\ j & j & j \end{Bmatrix} C^{LM}_{L_1M_1,\,L_2M_2}\hat{T}_{LM}, \tag{2.3.40}$$

defined based on the Wigner $6j$ symbol.

2.3.4 The Husimi Q function

The *Husimi Q function* is a quasi-probability distribution belonging to the same family of phase-space representations as the Wigner function and the Glauber–Sudarshan P function [34]. It provides a powerful visualization tool for quantum states, especially in the context of anticoherent states, as it highlights their isotropy and high symmetry properties.

For a spin-j system, the Husimi Q function of a quantum state $\hat{\rho}$ represents the overlap of this state with spin coherent states $|\Omega\rangle \equiv |\theta,\varphi\rangle$ on the Bloch sphere [34]:

$$Q(\Omega,\hat{\rho}) = \langle\Omega|\hat{\rho}|\Omega\rangle\,. \tag{2.3.41}$$

It essentially defines a natural probability density for obtaining the outcome $|\Omega\rangle$ in a projective measurement of the quantum state $\hat{\rho}$ in the coherent state basis, indicating the extent to which $\hat{\rho}$ is aligned with the direction (θ,φ). It verifies the relation:

$$\frac{2j+1}{4\pi}\int_{\mathcal{S}^2} Q(\Omega,\hat{\rho})d\Omega = 1. \tag{2.3.42}$$

In the case of a pure quantum state $\hat{\rho}_\psi = |\psi\rangle\langle\psi|$, The Husimi function simply becomes [34]:

$$Q(\Omega,\hat{\rho}_\psi) = |\langle\Omega|\psi\rangle|^2. \tag{2.3.43}$$

One can show that the Husimi Q function of a spin coherent state $|\psi\rangle = |\theta_0,\varphi_0\rangle$ reads:

$$Q(\theta,\varphi) = \left(\frac{1+\cos\theta\cos\theta_0+\sin\theta\sin\theta_0\cos(\varphi-\varphi_0)}{2}\right)^{2j}, \tag{2.3.44}$$

which can be greatly simplified as:

$$Q(\theta,\varphi) = \cos^{4j}\left(\frac{\Theta}{2}\right), \tag{2.3.45}$$

by defining the angle Θ between the directions $|\theta,\varphi\rangle$ and $|\theta_0,\varphi_0\rangle$ through:

$$\cos\Theta = \cos\theta\cos\theta_0+\sin\theta\sin\theta_0\cos(\varphi-\varphi_0). \tag{2.3.46}$$

This Husimi function is displayed Figure 2.6, along with the Husimi function (and its wall projections) of the Dicke state $|D^{(2)}_6\rangle$ in order to highlight its rotation symmetry.

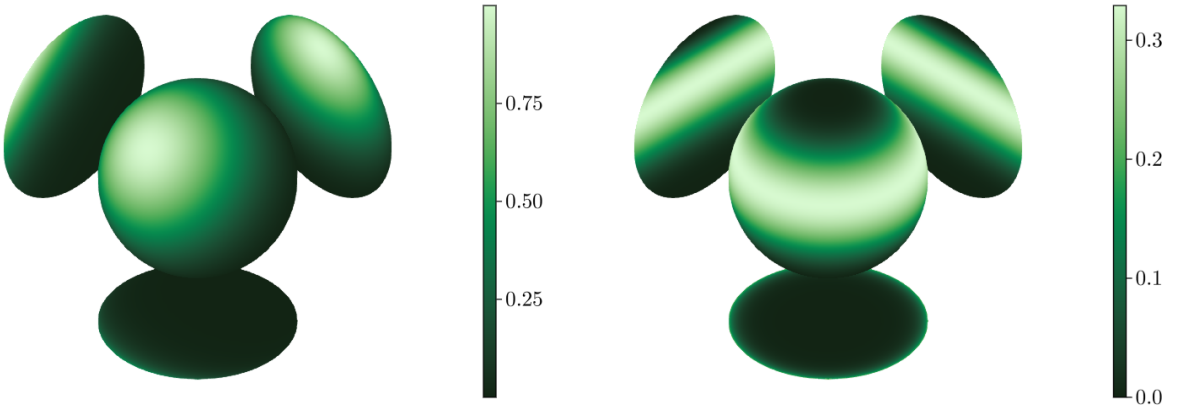

Figure 2.6: Left panel : Husimi Q function of a spin coherent state and its wall projections for the angular values $\theta = \pi/4$ and $\varphi = 0$ for a spin $j = 2$. Right panel : Husimi Q function of the Dicke state $|D_N^{(2)}\rangle$ and its wall projection for $N = 6$ qubits.

2.4 Anticoherence in spin systems

The notion of *anticoherence* was first introduced in 2006 by Jason Zimba [50] in the context of spin states and the Majorana representation while searching for quantum states that could be regarded as the natural opposite of coherent states. Indeed, coherent states are generally regarded as the most classical quantum states due to their behavior resembling classical spins, essentially pointing in a definite direction. In contrast, anticoherent states are characterized by a high degree of isotropy and entanglement. They possess no preferred direction and may therefore be viewed as highly non-classical states. Since the original publication, anticoherence has evolved from a mathematical curiosity into an active area of research, owing in part to the deep connection with entanglement, geometric representations of quantum states, and quantum-enhanced precision measurements. As a matter of fact, significant progress has been made toward understanding both the fundamental properties and practical applications of anticoherent states. A particularly notable development has been the growing interest in these states within the field of quantum metrology, where they constitute valuable resources owing to their high degree of isotropy, which leads to uniform sensitivity to rotations about arbitrary axes. Moreover, anticoherent states are especially attractive for quantum sensing, where they serve as optimal rotosensors to detect rotations about unknown axes with enhanced precision [16]. Finally, they are well suited for tasks that require probe states that are robust against environmental interactions, such as decoherence.

2.4.1 Anticoherent states

As previously emphasized, *anticoherent states* define the opposite of spin coherent states. While spin coherent states maximize the mean value of the angular momentum operator $\hat{\mathbf{J}}$ along their direction, anticoherent spin states exhibit a high degree of isotropy. In particular, the absence of a preferred direction implies that the expectation value of the angular momentum operator vanishes [50]:

$$\langle \hat{\mathbf{J}} \rangle_{\psi_{AC}} = \mathbf{0}, \tag{2.4.1}$$

where $|\psi_{AC}\rangle$ defines a pure anticoherent state of a spin-j system. Additionally, the contrast between coherent states and anticoherent states lies in the fact that anticoherent spin states maximize the

total variance of the angular momentum operators, whereas spin coherent states minimize it [34]:

$$(\Delta_{\psi_{AC}} J_x)^2 + (\Delta_{\psi_{AC}} J_y)^2 + (\Delta_{\psi_{AC}} J_z)^2 = \hbar^2 j(j+1), \qquad (\Delta_{\psi_{AC}} J_\alpha)^2 = \langle \hat{J}_\alpha^2 \rangle_{\psi_{AC}} - \underbrace{\langle \hat{J}_\alpha \rangle_{\psi_{AC}}^2}_{=0}. \tag{2.4.2}$$

Isotropy of the second moment, the variance, can be formulated using the relations [34]:

$$\langle \hat{J}_\alpha \hat{J}_\beta + \hat{J}_\beta \hat{J}_\alpha \rangle_{\psi_{AC}} = \frac{2\hbar^2 j(j+1)}{3} \delta_{\alpha,\beta}, \qquad \forall \alpha, \beta = x, y, z. \tag{2.4.3}$$

One can impose stronger constraints on the isotropic nature of such quantum states by requiring isotropy of higher-order moments. Hence, going beyond the second moment, we say that any pure anticoherent state is *t-anticoherent* (t-AC) if they satisfy the relation [51, 52]:

$$\frac{\partial}{\partial \mathbf{n}} \langle (\hat{\mathbf{J}} \cdot \mathbf{n})^k \rangle_{\psi_{AC}} = 0, \qquad \forall k \in \{1, \ldots, t\}. \tag{2.4.4}$$

In other words, the expectation value in (2.4.4) should be completely independent of the $\mathbf{n}$ axis. From this definition of t-anticoherence, it is clear that any pure quantum state that is t-anticoherent is also t'-anticoherent, with $t' < t$, by construction. This feature is only made possible for pure states through superpositions, which highlight the quantum nature of such spin states. To date, no general closed-form construction of anticoherent states is known for an arbitrary spin j value. Nonetheless, several families of anticoherent subspaces have been identified in the literature [53]. Furthermore, the experimental realization of such states remains an open challenge, although a recent study introduced the first protocol specifically aimed at generating spin-j anticoherent states of different orders [54].

A natural question concerns the extremal case of states exhibiting the maximum achievable order of anticoherence for a given spin j. Determining which orders t can be realized for a fixed finite spin number j remains an open problem, although numerical evidence has established the existence of states anticoherent up to order $t = 13$ [55]. Because of their exceptional isotropy and highly non-classical character, such states have earned the title of *"kings of quantumness"* [56]. Furthermore, it has been shown that arbitrarily high orders of anticoherence can be achieved for pure states, provided the spin number j is sufficiently large [34]. Anticoherent states that achieve the highest order of anticoherence are well known for small values of j. For example, in the case of a spin $j = 2$, the *tetrahedron state* achieves anticoherence of order 2. In the standard spin basis, it reads (up to a rotation) [34]:

$$|\psi_{\text{tetra}}\rangle = \frac{1}{2}\left(|2,-2\rangle + i\sqrt{2}\,|2,0\rangle + |2,2\rangle\right). \tag{2.4.5}$$

The origin of the "tetrahedron" appellation stems from the platonic solid obtained from its highly symmetric Majorana constellation, displayed in Figure 2.8. For a spin-3 system, the highest order anticoherent pure state is also unique (up to a phase factor) and is called the 3-AC *octahedron state*. In the standard spin basis, it reads [34]:

$$|\psi_{\text{octa}}\rangle = \frac{1}{\sqrt{2}}\left(|3,-2\rangle + |3,2\rangle\right). \tag{2.4.6}$$

However, the anticoherence order $t = 4$ and $t = 5$ can only be reached for a spin system with spin $j = 6$ at least. For example, the icosahedron state is 4-anticoherent [34]:

$$|\psi_{\text{ico}}\rangle = \frac{1}{5}\left(\sqrt{7}\,|6,-5\rangle + \sqrt{11}\,|6,0\rangle + \sqrt{7}\,|6,5\rangle\right). \tag{2.4.7}$$

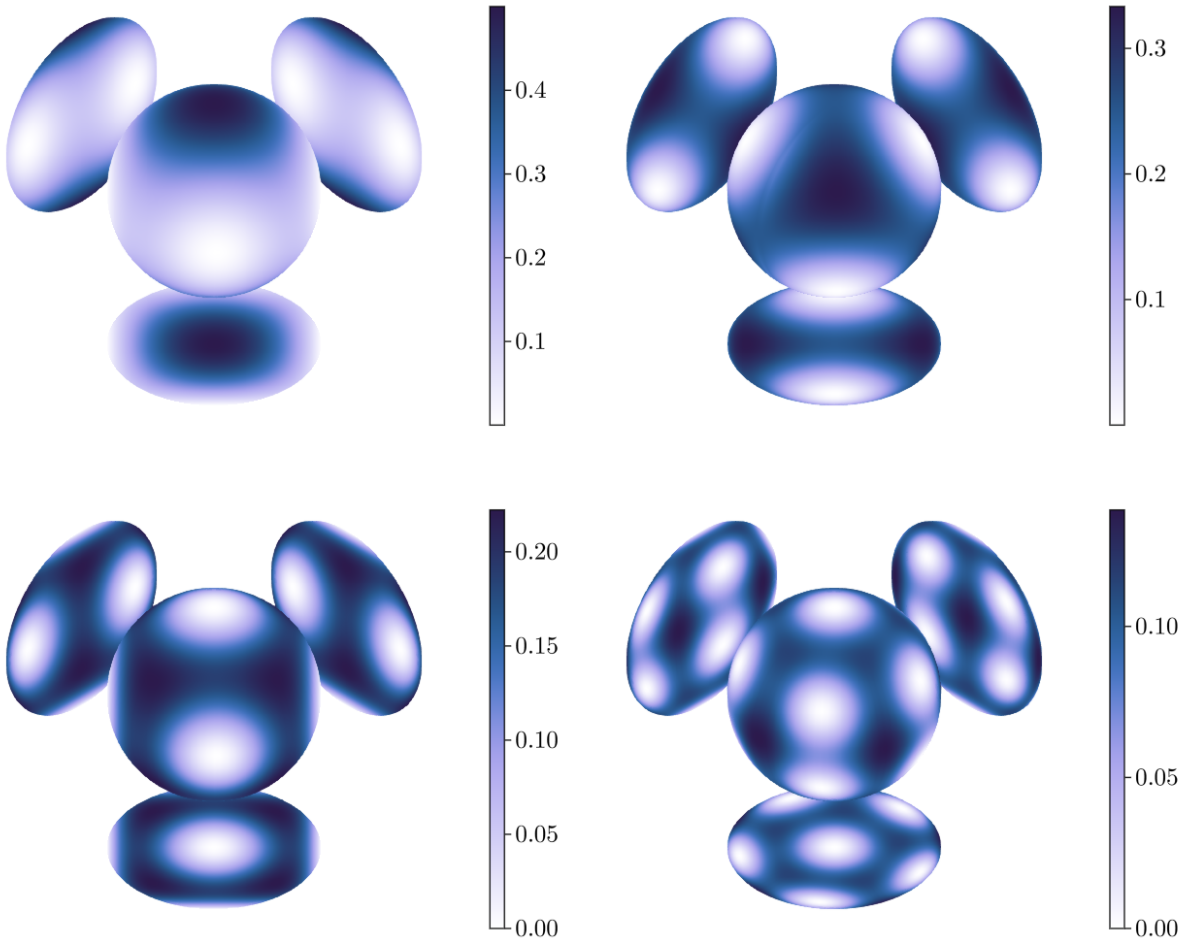

Figure 2.7: Husimi Q function and its wall projections for anticoherent states with increasing order of t-anticoherence. Top left: the GHZ state for $j = 2$. Top right: the tetrahedron state for $j = 2$. Bottom left: The octahedron state for $j = 3$. Bottom right: The icosahedral state for $j = 6$.

For higher j spin values, numerical studies have been performed in the literature and further indicate that the maximum attainable order of anticoherence is proportional to the square root of the spin number j [34]. Anticoherence can also be visualized directly on the Husimi Q function. For a given quantum spin j value, states with higher t-anticoherence will typically display complex patterns with higher isotropy, as shown in Figure 2.7. Moreover, the Majorana constellations of the octahedron state and the icosahedron state are displayed in Figure 2.8 to highlight their geometry through platonic solids.

The definitions that were introduced in the beginning of this section only concern quantum pure states. However, anticoherence is a concept that transcends the nature of the quantum state itself. Hence, we can define anticoherent mixed states using the formalism of the density operator. A mixed state $\hat{\rho}_{AC}$ is anticoherent (at first order) if it satisfies:

$$\mathrm{Tr}(\hat{\mathbf{J}}\hat{\rho}_{AC}) = 0, \tag{2.4.8}$$

As in the case of pure states, we can impose stronger conditions on the isotropy of the moments.

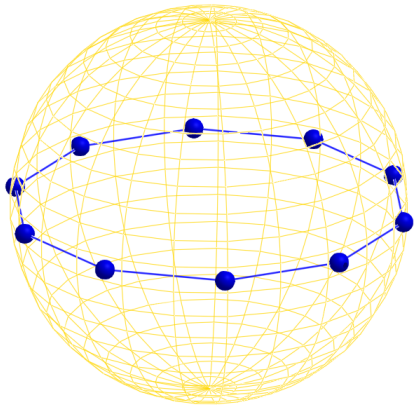

(a) The GHZ state for $j = 5$.

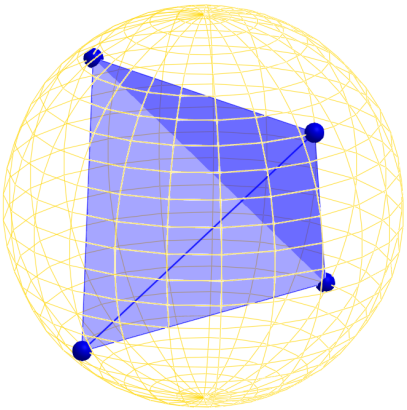

(b) The 2-AC tetrahedron state for $j = 2$.

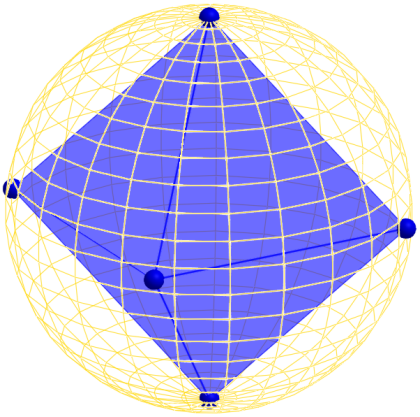

(c) The 3-AC octahedron state for $j = 3$.

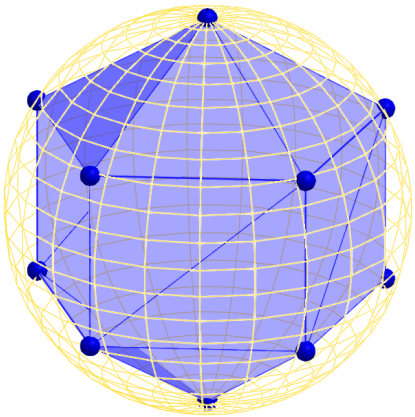

(d) The 4-AC icosahedron state for $j = 6$.

Figure 2.8: Majorana constellations of multiple anticoherent spin states with various order of t-anticoherence, ranging from 1 to 4. The Majorana stars are highlighted in blue and the Bloch sphere in gold.

Indeed, for the second moment, these conditions are translated as:

$$\mathrm{Tr}\left(\hat{\rho}_{AC}(\hat{J}_\alpha\hat{J}_\beta+\hat{J}_\beta\hat{J}_\alpha)\right)=\frac{2\hbar^2 j(j+1)}{3}\delta_{\alpha,\beta},\qquad \forall\alpha,\beta=x,y,z. \tag{2.4.9}$$

Moreover, a quantum mixed state $\hat{\rho}_{AC}$ is said to be t-anticoherent if the density operator satisfies the relation:

$$\frac{\partial}{\partial\mathbf{n}}\mathrm{Tr}(\hat{\rho}_{AC}(\hat{\mathbf{J}}\cdot\mathbf{n})^k)=0,\qquad \forall k\in\{1,\dots,t\}. \tag{2.4.10}$$

Finally, the spin tensor multipolar basis can be incorporated into the definition of t-anticoherence. Indeed, a spin-j quantum state $\hat{\rho}$ is t-anticoherent if and only if its multipoles vanish up to order t [41]:

$$\rho_{LM}=0,\qquad \forall L\leq t,\forall M=-L,\dots,L. \tag{2.4.11}$$

2.4.2 Measures of t-anticoherence

Naturally, it becomes necessary to introduce a mathematical object that quantifies the t-anticoherence of a pure or mixed state. In the case of mixed states, it has been shown that a (total) measure of t-anticoherence can be separated into a classical contribution and a quantum contribution [57]. Hence, we seek to find a mathematical form for a *measure of t-anticoherence* $\mathcal{A}_t$ of a pure state $|\psi\rangle$ that is a positive function whose value is contained within the range [0,1] and is invariant under arbitrary spin rotations and global phase changes. This quantity should satisfy [51]:

$$\mathcal{A}_t(|\psi\rangle)=\begin{cases}0 & \text{if and only if } |\psi\rangle \text{ is a coherent state}\\ 1 & \text{if and only if } |\psi\rangle \text{ is a } t\text{-anticoherent state}\end{cases} \tag{2.4.12}$$

The *purity based measure* $\mathcal{A}_t^R$ is defined based on the t-reduced qubit state of a spin j system. Let a spin j system be in a pure quantum state $|\psi\rangle$. Since this system is equivalent to a $N=2j$-qubit system in terms of their symmetric subspace, one can define the t-qubit reduced state of this subspace as [51]:

$$\hat{\rho}_t=\mathrm{Tr}_{N-t}(|\psi\rangle\langle\psi|),\qquad t\in\{1,\dots,N-1\}. \tag{2.4.13}$$

Thus, the purity-based measure of order t associated to this state is defined as:

$$\mathcal{A}_t^R(|\psi\rangle)=\frac{t+1}{t}(1-\mathrm{Tr}(\hat{\rho}_t^2)), \tag{2.4.14}$$

where the purity of the t-qubit reduced state is given by:

$$\mathrm{Tr}(\hat{\rho}_t^2)=\sum_{i=1}^{t+1}\lambda_i^2, \tag{2.4.15}$$

where $\{\lambda_i,\ \forall i=1,\dots,t+1\}$ is the set of $t+1$ eigenvalues of $\hat{\rho}_t$. The multiplicative prefactor $\frac{t+1}{t}$ ensures that the value of this measure stays in the correct range.

When moving to mixed states, isotropy can arise from either quantum correlations or classical statistical mixing. It has been shown that three metrics based on total, quantum, and classical anticoherence can be defined to solve this problem [57]. Moreover, it has been demonstrated that the purity-based measure admits a natural extension for the case of mixed states that coincides with the form (2.4.14) [57]. We should emphasize that the purity-based measure is only one possible realization of the measure; alternative constructions exist, with examples including the distance based measure and the fidelity based measure [57].

Chapter 3

Single-parameter estimation theory

Quantum Parameter Estimation Theory (QPET) is the branch of quantum science that investigates how precisely arbitrary unknown physical parameters can be measured using quantum systems. In numerous instances, such parameters cannot be observed directly. To overcome this limitation, the parameters of interest are encoded into a prepared quantum state describing the physical system of interest. The central objective is then to infer these unknown parameters from a series of N measurements performed on the system. Consequently, Quantum Parameter Estimation Theory provides the ideal mathematical framework for determining optimal measurement strategies, as well as the ultimate precision limits imposed by quantum mechanics.

In classical statistics, estimation accuracy is bounded by the so-called *Cramér–Rao inequality*, which relates the variance of an estimator to the quantity of information that the observed data carries about an unknown parameter, which is quantified by the *Fisher information* [58]. This key idea is generalized in quantum parameter estimation by recognizing that distinct quantum measurements extract different levels of informational content from the same quantum state. This leads to the concept of the *Quantum Fisher Information (QFI)*, which measures how sensitively a quantum state changes when the parameter varies [59]. Indeed, the magnitude of this quantity is directly linked to parameter estimation precision. Hence, the corresponding quantum analog of the Cramér–Rao bound sets the absolute minimum uncertainty achievable by any measurement protocol permitted by the laws of quantum mechanics [60]. The quantum nature of QPET is highly beneficial, as it introduces key concepts such as entanglement, squeezing, coherence, and superpositions that can be exploited in quantum protocols to surpass classical strategies. These ideas form the theoretical foundation of Quantum Metrology, with applications including atomic clocks [10], gravitational-wave detectors [15] and interferometry [12, 13]. Modern research, therefore, focuses not only on achieving ultimate precision limits but also on designing robust estimation protocols that remain advantageous under practical laboratory conditions. In essence, quantum parameter estimation theory aims to quantify the maximum amount of information that can be extracted from a quantum system and to design experimental protocols to approach the fundamental limits of precision according to the laws of quantum mechanics. Throughout this thesis, we will mainly focus on single parameter estimation, specifically on the estimation of a rotation angle θ resulting from the unitary transformation on a quantum state, and on the estimation of the squeezing strength χ induced by spin squeezing. Multi-parameter estimation and several other types of parameters and transformations are intensively discussed in modern research and literature [61, 62]. A brief introduction on multiparameter estimation is given in Chapter 6.

3.1 The fundamental scaling precision limits

Scaling laws in parameter estimation theory are essential to describe how the precision with which an unknown parameter θ can be estimated improves as we increase the number of experimental resources N. In practice, this number can represent the total number of times we repeat a probe–interaction–measurement process or the number of particles (spin-$\frac{1}{2}$ particles, photons,...) used as probes. Thus, the cornerstone of parameter estimation theory is the estimation uncertainty $\Delta\theta$ of the physical parameter under investigation, which is often quantified as the standard deviation or root-mean-square error of an estimator of θ. Consequently, different physical assumptions about correlations, noise, and measurement strategies lead to fundamentally different scaling behaviors.

In the most basic classical or uncorrelated quantum scenario, one encounters the so-called *shot-noise limit (SNL)*. This arises when N independent, statistically identical measurements are performed. Because each measurement contributes independent noise, the variance of the average decreases as $1/N$, leading to an uncertainty that scales as [58]:

$$\Delta\theta_{\mathrm{SNL}} \sim \frac{1}{\sqrt{N}}. \tag{3.1.1}$$

The SNL scaling is a direct consequence of the central limit theorem: random fluctuations average out slowly, only as the square root of the number of samples. In quantum optics, for example, this corresponds to measuring a phase using coherent light, where photons arrive independently and the phase uncertainty remains limited by Poissonian statistics.

Closely related to the shot-noise limit is the *standard quantum limit (SQL)*. In many contexts, particularly in quantum metrology within Quantum Physics, the SQL refers to the best precision achievable using separable quantum states and independent measurements. While the terminology can vary slightly across subfields, the SQL typically coincides with the same scaling as the shot-noise limit [58, 59]:

$$\Delta\theta_{\mathrm{SQL}} \sim \frac{1}{\sqrt{N}}. \tag{3.1.2}$$

Thus, the SQL represents a limitation imposed not by classicality itself, but rather by the absence of useful quantum correlations between the probes. A fundamentally stronger scaling becomes possible when quantum resources such as entanglement are exploited. This leads to the *Heisenberg limit (HL)*, which represents the ultimate precision bound allowed by quantum mechanics under ideal conditions. In this regime, the uncertainty scales as [58, 59]:

$$\Delta\theta_{\mathrm{HL}} \sim \frac{1}{N}. \tag{3.1.3}$$

This quadratic improvement over the SQL arises because entangled states allow the N probes to act collectively as a single highly sensitive quantum system rather than as independent noisy probes. Intuitively, while independent measurements reduce noise by averaging, entangled states enhance the signal sensitivity itself, making the parameter imprint on the quantum state effectively scale with N.

However, the Heisenberg limit is an idealized bound. In realistic systems, decoherence, loss, and imperfect control often degrade entanglement and reduce the achievable scaling back toward the SQL [63]. As a result, the observed performance in practical experiments frequently lies between the SQL and the Heisenberg limit, depending on how robustly quantum correlations can be maintained.

3.2 Parameter encoding in quantum states

As we will emphasize in future sections, the main objectives of (single) parameter quantum metrology are to estimate a physical quantity in the form of an unknown parameter θ with the highest precision that is physically reachable. The mathematical concept that is used in quantum metrology to encode the unknown parameter is the quantum state of a system under investigation. In the context of quantum parameter estimation theory, we define a *parameter family of mixed quantum states* as [64]:

$$\{\hat{\rho}(\theta)\}_{\theta\in\Theta}, \tag{3.2.1}$$

where θ is a continuous real parameter that is contained in a parameter space Θ. Note that in this work, we will often consider the condensed notation $\hat{\rho}_\theta \equiv \hat{\rho}(\theta)$. This object allows us to describe how the quantum system used in quantum strategies changes depending on variations of the encoded parameter, mainly by computing the quantum Fisher information. Throughout this master's thesis, we will focus on parameter families that are encoded by a unitary transformation:

$$\hat{\rho}(\theta) = \hat{U}(\theta)\hat{\rho}\hat{U}^\dagger(\theta), \qquad U^\dagger(\theta) = U^{-1}(\theta), \tag{3.2.2}$$

where $\hat{U}(\theta)$ is a unitary operator encoding the parameter that we wish to estimate, and $\hat{\rho}$ defines the mixed state describing the quantum system prior to the transformation. Specifically, we will focus on *phase encoding* transformations, which are specified by the form [59, 60]:

$$\hat{U}(\theta) = e^{-i\theta\hat{G}}, \qquad \theta \in \mathbb{R}, \tag{3.2.3}$$

where the self-adjoint operator $\hat{G}$ is known as the *generator* of the transformation. In practice, $\hat{G}$ can represent various physical observables, such as Hamiltonians or spin operator components. For pure states, the transformation (3.2.2) simply reads:

$$|\psi(\theta)\rangle = \hat{U}(\theta)\,|\psi\rangle\,, \qquad \hat{U}(\theta) = e^{-i\theta\hat{G}}, \tag{3.2.4}$$

where $|\psi\rangle \in \mathcal{H}$ refers to the pure quantum state describing the quantum system before phase encoding. Hence, $\{|\psi(\theta)\rangle\}_{\theta\in\Theta}$ refers to a uni-parametric family of pure states. In practice, for phase encoding transformations, the parameter may represent physical quantities that include elapsed time, magnetic or electric field amplitude, rotation angle or frequency. As emphasized in section 1.2.1, for general unitary transformations, the canonical form of $\hat{\rho}(\theta)$ is given by its spectral decomposition:

$$\hat{\rho}(\theta) = \sum_{i=1}^{d_\mathcal{H}} \lambda_\theta^{(i)}\,|\Psi_\theta^{(i)}\rangle\,\langle\Psi_\theta^{(i)}|\,, \tag{3.2.5}$$

where the eigenvectors $|\Psi_\theta^{(i)}\rangle$ and eigenvalues $\lambda_\theta^{(i)}$ generally both depend on the parameter θ that we wish to estimate.

3.3 Methodology for estimator construction

The main problem faced in single parameter estimation theory is estimating the value of the parameter θ encoded in the density operator with high precision, based on measurements carried out on the physical system. Mathematically speaking, a measurement is represented by a random variable x. Experimentally, one carries out a large number of independent trials N, each yielding a specific

measurement outcome x_i. As a result, one can construct the vector of outcomes (or data record) [60]:

$$\mathbf{x} = (x_1, \ldots, x_N)^T. \tag{3.3.1}$$

Therefore, the estimation of the desired parameter θ depends on a given set of measurements through a conditional probability density labeled $p(x|\theta)$, determined by the statistical model of the experimental process. One typically assumes that the N random variables are identically distributed such that each variable x_i is governed by the same parameter θ. Moreover, we infer that each measurement carried out is independent of the others, which mathematically implies that the joint distribution of the N random variables x_i can be factorized as a product [60]:

$$p(\mathbf{x}|\theta) = \prod_{i=1}^{N} p(x_i|\theta). \tag{3.3.2}$$

Based on the collected data represented by a set of the form (3.3.1), the main goal of parameter estimation is to construct an estimator, which is defined by a function $\tilde{\theta}(\mathbf{x})$ of the N random variables, as the notation emphasizes. We can define the expected (average) value of this estimator over a repeated number of trials as [60]:

$$\mathbb{E}_{\mathbf{x}}[\tilde{\theta}] = \int d\mathbf{x} p(\mathbf{x}|\theta)\tilde{\theta}(\mathbf{x}), \tag{3.3.3}$$

for continuous variables, and:

$$\mathbb{E}_{\mathbf{x}}[\tilde{\theta}] = \sum_{\mathbf{x}} p(\mathbf{x}|\theta)\tilde{\theta}(\mathbf{x}), \tag{3.3.4}$$

for discrete random variables. If the average value of the estimator equals the true parameter being estimated, the estimator is said to be unbiased. Hence, these estimators satisfy:

$$\mathbb{E}_{\mathbf{x}}[\tilde{\theta}] = \theta. \tag{3.3.5}$$

There are several ways of constructing the function that is used to define estimators in the literature. We will mainly focus on the forms that are best suited to the context of quantum metrology and are applicable in realistic experimental conditions.

3.3.1 Maximum likelihood estimator

The maximum likelihood estimator is arguably one of the most widely spread example of estimators. It is defined as [60]:

$$\tilde{\theta}_{\mathrm{ML}}(\mathbf{x}) = \arg\max_{\theta} p(\mathbf{x}|\theta). \tag{3.3.6}$$

In other words, this estimator corresponds to the value of the parameter θ that makes the observed data set $\mathbf{x}$ the most probable, hence its name. In practice, one often uses the Napierian logarithm of the likelihood to benefit from the valuable properties of the log. This defines the log-likelihood function [58]:

$$l(\theta) = \ln\left(p(\mathbf{x}|\theta)\right). \tag{3.3.7}$$

Inserting (3.3.2) yields the simple form:

$$l(\theta) = \sum_{i=1}^{N} \ln\left(p(x_i|\theta)\right). \tag{3.3.8}$$

The maximum likelihood estimator is then obtained by differentiating this expression and solving the equation:

$$\left.\frac{\partial l(\theta)}{\partial \theta}\right|_{\theta=\tilde{\theta}_{\mathrm{ML}}} = 0. \tag{3.3.9}$$

3.3.2 The method of moments

The method of moments aims to build an estimator $\tilde{\theta}$ of an unknown parameter encoded in a quantum state $\hat{\rho}(\theta)$ based on the measurement outcomes of a physical observable $\hat{M}$ whose expectation value depends on θ. Hence, suppose that we carry out N trials of measurements of $\hat{M}$ on the physical systems, yielding the outcomes $m_1, \ldots, m_N$. One can define the sample mean as [58]:

$$\bar{M}_N = \frac{1}{N}\sum_{i=1}^{N} m_i. \tag{3.3.10}$$

On the other hand, the expectation value of $\hat{M}$ in the quantum state $\hat{\rho}_\theta$ is defined as:

$$\langle \hat{M} \rangle_{\rho_\theta} = \mathrm{Tr}(\hat{\rho}_\theta \hat{M}), \tag{3.3.11}$$

and is referred to as the *calibration curve* [65]. The key idea of the method of moments is to build an estimator that satisfies:

$$\langle \hat{M} \rangle_{\tilde{\theta}} = \bar{M}_N. \tag{3.3.12}$$

In other words, the estimator selects the parameter value whose predicted signal matches the observed one based on a sample of the data. For a large number of trials N, the right-hand side converges to the exact expected mean value of $\hat{M}$, ensuring that the constructed estimator is asymptotically unbiased[1]:

$$\lim_{N\to+\infty} \bar{M}^{(N)} = \langle \hat{M} \rangle_\theta \,. \tag{3.3.13}$$

Since the expectation value of $\hat{M}$ depends on θ through:

$$\langle \hat{M} \rangle_{\rho_\theta} = f(\theta), \tag{3.3.14}$$

where f is an invertible function, one can build the estimator $\tilde{\theta}$ by inverting the calibration curve, such that [66]:

$$\tilde{\theta}_{\mathrm{MM}} = f^{-1}(\bar{M}_N), \tag{3.3.15}$$

where f is an invertible function. We should stress that, in general, the solution of (3.3.12) is not unique and requires either prior knowledge or a restriction to the parameter interval. Moreover, the variance of the estimator can be computed using:

$$(\Delta\tilde{\theta}_{\mathrm{MM}})^2 = \mathbb{E}_\theta[(\tilde{\theta}_{\mathrm{MM}} - \theta)^2], \tag{3.3.16}$$

which in this case, satisfies [66]:

$$(\Delta\tilde{\theta}_{\mathrm{MM}})^2 = \frac{1}{N}\frac{\mathrm{Var}_\theta(\hat{M})}{(\partial_\theta \langle \hat{M} \rangle_{\rho_\theta})^2}. \tag{3.3.17}$$

Hence, small fluctuations in measurement outcomes and rapid changes of the observable $\hat{M}$ with respect to the parameter contribute to a smaller uncertainty.

[1] Therefore, for any finite set of trials, the estimator is biased based on this argument.

3.3.3 The Bayesian approach

The central idea of Bayesian estimation is to have prior knowledge about the unknown parameter that we wish to estimate before carrying out any measurements on the system, which can be done by assuming a prior distribution $p(\theta)$. Suppose that we carry out N measurements on the system that lays in the quantum state $\hat{\rho}(\theta)$ containing the unknown parameter, such that we get the measurement outcomes set $\mathbf{x}$. Hence, the measurement statistics are governed by the likelihood function (3.3.2) for independent and identically distributed measurements. Based on Baye's theorem, we can compute the *posterior distribution* [67]:

$$p(\theta|\mathbf{x}) = \frac{p(\mathbf{x}|\theta)p(\theta)}{p(\mathbf{x})}, \tag{3.3.18}$$

which represents the probability distribution after seeing data and contains the full statistical information about the unknown parameter. Based on this quantity, we can build the estimator [67]:

$$\tilde{\theta}_{\mathrm{B}} = \int_{\Theta} \theta\, p(\theta|\mathbf{x}) d\theta, \tag{3.3.19}$$

with variance:

$$(\Delta\tilde{\theta}_{\mathrm{B}})^2 = \int_{\Theta} (\tilde{\theta}_{\mathrm{B}} - \theta)^2\, p(\theta|\mathbf{x}) d\theta. \tag{3.3.20}$$

3.4 The symmetric logarithmic derivative

The symmetric logarithmic derivative refers to an operator $\hat{L}_\theta$ that is widely used in parameter estimation theory and quantum metrology, mainly to compute the quantum Fisher information and to perform an optimal measurement in its eigenbasis in order to reach the Cramér-Rao bound, which constitutes the single parameter precision limit of the information accessible. The symmetric logarithmic derivative refers to an operator $\hat{L}_\theta$ that is defined based on a parameter family $\hat{\rho}(\theta)$ through the relation [59]:

$$\frac{\partial\hat{\rho}(\theta)}{\partial\theta} = \frac{1}{2}\left\{\hat{\rho}_\theta, \hat{L}_\theta\right\}, \tag{3.4.1}$$

which represents the equation governing the dynamics of the quantum system under investigation. On the other hand, unitary dynamics are characterized by an Hamiltonian operator $\hat{H}$ and are given by the Von-Neumann equation [59]:

$$\frac{\partial\hat{\rho}(\theta)}{\partial\theta} = -\frac{i}{\hbar}\left[\hat{H}, \hat{\rho}_\theta\right]. \tag{3.4.2}$$

We can obtain an explicit expression of $\hat{L}_\theta$ that depends on the eigenvectors and eigenvalues of the parameter family $\hat{\rho}(\theta)$, as well as the Hamiltonian $\hat{H}$ as follows. First, we diagonalize $\hat{\rho}(\theta)$ to obtain its spectral decomposition:

$$\hat{\rho}(\theta) = \sum_{i=1}^{d_{\mathcal{H}}} \lambda_\theta^{(i)} \left|\Psi_\theta^{(i)}\right\rangle \left\langle\Psi_\theta^{(i)}\right|, \tag{3.4.3}$$

Using this decomposition, we can compute the projection of equation (3.4.1) in the eigenbasis of $\hat{\rho}(\theta)$ in terms of the matrix elements:

$$\langle\Psi_\theta^{(k)}|\partial_\theta\hat{\rho}_\theta|\Psi_\theta^{(l)}\rangle = \frac{1}{2}\left(\langle\Psi_\theta^{(k)}|\hat{\rho}_\theta\hat{L}_\theta|\Psi_\theta^{(l)}\rangle + \langle\Psi_\theta^{(k)}|\hat{L}_\theta\hat{\rho}_\theta|\Psi_\theta^{(l)}\rangle\right), \tag{3.4.4}$$

which yields, after inserting the spectral decomposition and the orthogonality property of the eigenbasis:

$$\langle \Psi_\theta^{(k)} | \partial_\theta \hat{\rho}_\theta | \Psi_\theta^{(l)} \rangle = \frac{1}{2}(\lambda_\theta^{(k)} + \lambda_\theta^{(l)}) \langle \Psi_\theta^{(k)} | \hat{L}_\theta | \Psi_\theta^{(l)} \rangle . \tag{3.4.5}$$

Using the same approach on equation (3.4.2) yields:

$$\langle \Psi_\theta^{(k)} | \partial_\theta \hat{\rho}_\theta | \Psi_\theta^{(l)} \rangle = \frac{i}{\hbar}(\lambda_\theta^{(k)} - \lambda_\theta^{(l)}) \langle \Psi_\theta^{(k)} | \hat{L}_\theta | \Psi_\theta^{(l)} \rangle . \tag{3.4.6}$$

We can compare the right-hand side of (3.4.5) and (3.4.6) to obtain the matrix elements of the symmetric logarithmic derivative in the eigenbasis of $\hat{\rho}(\theta)$:

$$\langle \Psi_\theta^{(k)} | \hat{L}_\theta | \Psi_\theta^{(l)} \rangle = \frac{2i}{\hbar} \frac{\lambda_\theta^{(k)} - \lambda_\theta^{(l)}}{\lambda_\theta^{(k)} + \lambda_\theta^{(l)}} \langle \Psi_\theta^{(k)} | \hat{H} | \Psi_\theta^{(l)} \rangle , \tag{3.4.7}$$

for $\lambda_\theta^{(k)} + \lambda_\theta^{(l)} > 0$, for all $k, l = 1, \ldots, d_{\mathcal{H}}$. These matrix elements can be inserted into the expansion of $\hat{L}_\theta$ in the eigenbasis of $\hat{\rho}(\theta)$:

$$\hat{L}_\theta = \sum_{k,l=1}^{d_{\mathcal{H}}} \langle \Psi_\theta^{(k)} | \hat{L}_\theta | \Psi_\theta^{(l)} \rangle \, | \Psi_\theta^{(k)} \rangle \langle \Psi_\theta^{(l)} | , \tag{3.4.8}$$

to obtain the final desired expression of the symmetric logarithmic derivative [59]:

$$\hat{L}_\theta = \frac{2i}{\hbar} \sum_{k,l=1}^{d_{\mathcal{H}}} \frac{\lambda_\theta^{(k)} - \lambda_\theta^{(l)}}{\lambda_\theta^{(k)} + \lambda_\theta^{(l)}} \langle \Psi_\theta^{(k)} | \hat{H} | \Psi_\theta^{(l)} \rangle \, | \Psi_\theta^{(k)} \rangle \langle \Psi_\theta^{(l)} | , \qquad \lambda_\theta^{(k)} + \lambda_\theta^{(l)} > 0. \tag{3.4.9}$$

From this decomposition, it is clear that the symmetric logarithmic derivative is self-adjoint and therefore corresponds to a physical observable, provided $\hat{\rho}(\theta)$ defines a valid differentiable density operator with respect to the parameter θ. Moreover, in the particular case of pure states $\hat{\rho}_\theta = |\psi_\theta\rangle \langle \psi_\theta|$, this formula reduces to [59]:

$$\hat{L}_\theta = \frac{2i}{\hbar} \left[|\psi_\theta\rangle \langle \psi_\theta| , \hat{H} \right] . \tag{3.4.10}$$

3.5 The quantum Fisher information

The *Quantum Fisher Information (QFI)* is one of the central quantities in quantum estimation theory and quantum metrology. It quantifies how sensitively a quantum state depends on a parameter θ and therefore determines the ultimate precision with which that parameter can be estimated.

In classical statistics, the Fisher information $F(\theta)$ measures how much information a probability distribution $p(x|\theta)$ carries about an unknown parameter θ, where x denotes the measurement outcome or observed data obtained from an experiment. Depending on the physical measurement considered, this variable is either discrete or continuous. The Fisher information in the continuous case is written as an integral [60]:

$$F(\theta) = \int dx \frac{1}{p(x|\theta)} \left(\frac{\partial p(x|\theta)}{\partial \theta} \right)^2 , \tag{3.5.1}$$

whereas the discrete case involves a sum instead. The Quantum Fisher Information generalizes this idea to quantum states, where measurements themselves are part of the optimization problem.

The parameter is encoded in the quantum state $\hat{\rho}(\theta)$ of the physical system under investigation. Measurement outcomes depend on the positive operator-valued measure (POVM) $\hat{M}_x$, such that the probability distribution takes the form [60]:

$$p(x|\theta) = \mathrm{Tr}\left(\hat{\rho}(\theta)\hat{M}_x\right). \tag{3.5.2}$$

Different measurements produce different classical Fisher information. The Quantum Fisher Information $F_Q(\theta)$ is defined as the maximum over all possible measurements [60]:

$$F_Q(\hat{\rho}(\theta)) = \max_{\{\hat{M}_x\}} F(\theta). \tag{3.5.3}$$

Thus, the QFI characterizes the intrinsic distinguishability of nearby quantum states $\hat{\rho}(\theta)$ and $\hat{\rho}(\theta + d\theta)$. We shall now focus on computing the QFI, which can be done using specific forms that will be helpful both on a theoretical and numerical point of view throughout this master's thesis.

3.5.1 The eigenspace decomposition

It is useful to decompose the quantum Fisher information using the spectral decomposition (3.4.3) of the quantum state $\hat{\rho}(\theta) \equiv \hat{\rho}_\theta$ that contains the parameter we wish to estimate. An explicit derivation based on the symmetric logarithmic derivative of this so-called *eigenspace decomposition* of the quantum Fisher information is derived explicitly in [21, 68]. Thus, this decomposition reads:

$$F_Q(\theta) = \sum_{i=1}^{r} \frac{\left(\partial_\theta \lambda_\theta^{(i)}\right)^2}{\lambda_\theta^{(i)}} + 4\sum_{i=1}^{r} \lambda_\theta^{(i)} \langle \partial_\theta \Psi_\theta^{(i)} | \partial_\theta \Psi_\theta^{(i)} \rangle - 8 \sum_{i,j=1}^{r} \frac{\lambda_\theta^{(i)} \lambda_\theta^{(j)}}{\lambda_\theta^{(i)} + \lambda_\theta^{(j)}} |\langle \Psi_\theta^{(i)} | \partial_\theta \Psi_\theta^{(j)} \rangle|^2, \tag{3.5.4}$$

where we defined the rank $r = \mathrm{rank}(\rho_\theta)$. The first term on the right-hand side of this expression represents the classical part of the information encoded. Moreover, the second term represents a measure of the average quantum "speed" of each eigenstate along the parameter path, capturing the local motion of these states. Finally, the last term captures how eigenvectors mix into each other under parameter change. In particular, it removes redundant contributions arising from the components of $|\partial_\theta \Psi_\theta^{(j)}\rangle$, along with other eigenvectors, thereby suppressing inter-eigenstate mixing terms and ensuring basis-invariant distinguishability. Consequently, it can be seen that the spectral decomposition of $\hat{\rho}(\theta)$ truly encodes the total information contained in the quantum state. Equation (3.5.4) can be decomposed into a pure classical contribution and a pure quantum contribution, together forming the (total) quantum Fisher information. Indeed, we can write [68]:

$$F_Q(\theta) = F_{\text{classical}}(\theta) + F_{\text{quantum}}(\theta), \tag{3.5.5}$$

where both contributions are defined based on the right-hand side of (3.5.4). The classical contribution can be identified based on the theory of classical Fisher information. This contribution reads:

$$F_{\text{classical}}(\theta) = \sum_{i=1}^{r} \frac{\left(\partial_\theta \lambda_\theta^{(i)}\right)^2}{\lambda_\theta^{(i)}}, \tag{3.5.6}$$

and depends solely on the eigenvalues of the mixed state. Hence, it can be seen that the classical contribution vanishes if the eigenvalues do not contain any information on the parameter that we wish to estimate. Consequently, we can deduce the purely quantum contribution, which reads:

$$F_{\text{quantum}}(\theta) = 4\sum_{i=1}^{r} \lambda_\theta^{(i)} \langle \partial_\theta \Psi_\theta^{(i)} | \partial_\theta \Psi_\theta^{(i)} \rangle - 8 \sum_{i,j=1}^{r} \frac{\lambda_\theta^{(i)} \lambda_\theta^{(j)}}{\lambda_\theta^{(i)} + \lambda_\theta^{(j)}} |\langle \Psi_\theta^{(i)} | \partial_\theta \Psi_\theta^{(j)} \rangle|^2. \tag{3.5.7}$$

This term depends on both the eigenvalues and the eigenvectors of the mixed state. It can be instructive to compute (3.5.4) for a pure state $\hat{\rho}(\theta) = |\psi(\theta)\rangle\langle\psi(\theta)|$. Inserting this expression in (3.5.4) yields the quantum Fisher information for a pure state [68]:

$$F_Q(|\psi_\theta\rangle, \theta) = 4\langle\partial_\theta\psi_\theta|\partial_\theta\psi_\theta\rangle - 4|\langle\psi_\theta|\partial_\theta\psi_\theta\rangle|^2. \tag{3.5.8}$$

Hence, for pure states, the classical contribution to the quantum Fisher information vanishes. Moreover, for a unitary parametrization of the mixed state of the form (3.2.2) with a unitary operator $\hat{U}(\theta)$ encoding the parameter of interest and $\hat{\rho}$ being a fixed mixed state that does not contain any information on the parameter, the classical contribution vanishes since $\hat{\rho}(\theta)$ shares the exact same set of eigenvalues as $\hat{\rho}_0$, which do not depend on the estimated parameter. Finally, the classical contribution is invariant under unitary transformations of the type:

$$\hat{\rho}'(\theta) = \hat{U}\hat{\rho}(\theta)\hat{U}^\dagger, \qquad \hat{U}^\dagger = \hat{U}^{-1}, \tag{3.5.9}$$

where $\hat{U}$ is a unitary operator that does not depend on θ, since this amounts to a change of basis. Using the explicit form of the quantum Fisher information for a pure state, we can rewrite the quantum contribution of the quantum Fisher information in the convenient form [68]:

$$F_{\text{quantum}}(\theta) = 4\sum_{i=1}^{r}\lambda_\theta^{(i)}F_Q(|\Psi_\theta^{(i)}\rangle, \theta) - 8\sum_{\substack{i,j=1\\ i\neq j}}^{r}\frac{\lambda_\theta^{(i)}\lambda_\theta^{(j)}}{\lambda_\theta^{(i)}+\lambda_\theta^{(j)}}|\langle\Psi_\theta^{(i)}|\partial_\theta\Psi_\theta^{(j)}\rangle|^2, \tag{3.5.10}$$

where $F_Q(|\Psi_\theta^{(i)}\rangle, \theta)$ is the quantum Fisher information of the eigenstate $|\Psi_\theta^{(i)}\rangle$.

3.5.2 The Bures distance form

The quantum Fisher information is linked with the distinguishability of a parameter family $\hat{\rho}(\theta)$ for small variations of the unknown parameter θ. Mathematically, this can be shown by introducing the *Bures distance* $d^{\text{B}}(\hat{\rho}_1, \hat{\rho}_2)$, which represents an operator distance between two operators $\hat{\rho}_1, \hat{\rho}_2$ and can be defined through the relation [34]:

$$\left(d^{\text{B}}(\hat{\rho}_1, \hat{\rho}_2)\right)^2 = 2\left(1 - \sqrt{F(\hat{\rho}_1, \hat{\rho}_2)}\right), \tag{3.5.11}$$

where $F(\hat{\rho}_1, \hat{\rho}_2)$ is the Ulhman-Josza fidelity of two quantum states [34]:

$$F(\hat{\rho}_1, \hat{\rho}_2) = \text{Tr}\left(\sqrt{\sqrt{\hat{\rho}_1}\hat{\rho}_2\sqrt{\hat{\rho}_1}}\right)^2. \tag{3.5.12}$$

The key idea is to compute the Bures distance for a parameter dependent family $\hat{\rho}(\theta)$, specifically by considering the Bures distance between $\hat{\rho}(\theta)$ and $\hat{\rho}(\theta + d\theta)$, where $d\theta$ is a finite increment of the parameter θ. Inserting the expression of the fidelity yields:

$$\left(d^{\text{B}}(\hat{\rho}_\theta, \hat{\rho}_{\theta+d\theta})\right)^2 = 2 - 2\,\text{Tr}\left(\sqrt{\sqrt{\hat{\rho}_\theta}\hat{\rho}_{\theta+d\theta}\sqrt{\hat{\rho}_\theta}}\right). \tag{3.5.13}$$

One can now derive the following relation using the spectral decomposition [58, 69]:

$$\left(d^{\text{B}}(\hat{\rho}_\theta, \hat{\rho}_{\theta+d\theta})\right)^2 = \sum_{i,j=1}^{d_{\mathcal{H}}}\frac{d\theta^2\lambda_\theta^{(i)}}{(\lambda_\theta^{(i)}+\lambda_\theta^{(j)})^2}\left|\langle\Psi_\theta^{(i)}|\frac{d\hat{\rho}_\theta}{d\theta}|\Psi_\theta^{(j)}\rangle\right|^2. \tag{3.5.14}$$

The right-hand side is proportional to the quantum Fisher information, as shown in [58], which can be used to define this latter quantity in terms of the Bures distance. Indeed, the quantum Fisher information is formally defined by considering that the increment $d\theta$ represents an infinitesimal change such that:

$$F_Q(\theta) = 4 \lim_{d\theta \to 0} \frac{\left(d^{\mathrm{B}}(\hat{\rho}_\theta, \hat{\rho}_{\theta+d\theta})\right)^2}{d\theta^2}. \tag{3.5.15}$$

The limit appearing in this definition is crucial because it ensures that the quantum Fisher information is a local quantity, characterizing the sensitivity of the quantum state to infinitesimal variations of the parameter θ. From a computational perspective, the expression (3.5.15) is advantageous since the QFI can be obtained from finite-difference evaluations of the Bures distance between nearby states, which is often numerically more stable and easier to implement than analytic formulas involving derivatives of eigenvalues and eigenvectors. The intrinsic nature of (3.5.15) is purely geometrical. In fact, the QFI is the Riemannian metric tensor associated with the geometry of quantum state space induced by the Bures distance. Indeed, for two infinitesimally close states $\hat{\rho}(\theta)$ and $\hat{\rho}(\theta + d\theta)$, the squared Bures distance admits the form [70]:

$$\left(d^{\mathrm{B}}(\hat{\rho}_\theta, \hat{\rho}_{\theta+d\theta})\right)^2 = \frac{1}{4} F_Q(\theta) d\theta^2 + \mathcal{O}(d\theta^3). \tag{3.5.16}$$

Thus, this expression emphasizes that the quantum Fisher information governs the rate at which the Bures distance increases under small changes of the parameter θ. Consequently, a larger QFI implies that neighboring states become increasingly distinguishable for a given parameter variation $d\theta$, enhancing the sensitivity of the quantum state to the unknown parameter and improving the achievable precision in parameter estimation.

3.5.3 Properties of the QFI

In this section, we review the main properties of the Quantum Fisher information [58–60].

1. Convexity in the quantum states: Let $\hat{\rho}(\theta)$ be a parameter family defined by the mixture:

$$\hat{\rho}(\theta) = \sum_{k=1}^{n} p_k \hat{\rho}_\theta^{(k)}, \qquad \sum_{k=1}^{n} p_k = 1, \tag{3.5.17}$$

   where $p_k \geq 0 \ \forall k = 1, \ldots, n$ for $n \geq 2$. The QFI verifies:

$$F_Q(\hat{\rho}_\theta, \theta) \leq \sum_{k=1}^{n} p_k F_Q(\hat{\rho}_\theta^{(k)}, \theta). \tag{3.5.18}$$

2. Additivity over independent measures: Let $\hat{\rho}(\theta)$ be a parameter family defined by the mixture:

$$\hat{\rho}(\theta) = \bigotimes_{k=1}^{n} \hat{\rho}_\theta^{(k)}, \tag{3.5.19}$$

   where $n \geq 2$. The QFI verifies:

$$F_Q(\hat{\rho}_\theta, \theta) = \sum_{k=1}^{n} F_Q(\hat{\rho}_\theta^{(k)}, \theta). \tag{3.5.20}$$

3. Invariance under unitary parametric transformation: Let $\hat{\rho}(\theta)$ be a parameter family, $\hat{\rho}_0$ be a general (fixed) mixture independent of θ, and $\hat{U}(\theta)$ be a unitary operator of the form:

$$\hat{U}(\theta) = e^{-i\theta\hat{G}}, \tag{3.5.21}$$

where the self-adjoint operator $\hat{G}$ is the generator of the transformation. Because for a unitary transformation of $\hat{\rho}_\theta$ of the type (3.2.2), the eigenvalues of $\hat{\rho}_\theta$ do not depend on the parameter θ, the quantum Fisher information reduces to the parameter-independent form:

$$F_Q(\hat{\rho}_\theta, \theta) = 2\sum_{i,j=1}^{d_\mathcal{H}} \frac{(\lambda_i - \lambda_j)^2}{\lambda_i + \lambda_j} |\langle\Psi_i|\hat{G}|\Psi_j\rangle|^2, \qquad \lambda_i + \lambda_j > 0. \tag{3.5.22}$$

For the sole case of a pure state $|\psi_\theta\rangle$, the unitary transformation reads:

$$|\psi(\theta)\rangle = e^{-i\theta\hat{G}} |\psi_0\rangle\,, \tag{3.5.23}$$

where $|\psi_0\rangle$ is a fixed initial state. In this case, the QFI is also independent of θ and reduces to:

$$F_Q(|\psi_\theta\rangle\,, \theta) = 4(\Delta_{\psi_0} G)^2. \tag{3.5.24}$$

4. Relation with the symmetric logarithmic derivative: The quantum Fisher information is related to the symmetric logarithmic derivative. Using (3.4.9) and the spectral decomposition (3.4.3), as well as (3.5.22) (the Hamiltonian $\hat{H}$ is the corresponding generator of the dynamics), we can show that:

$$F_Q(\theta) = \mathrm{Tr}(\hat{\rho}_\theta \hat{L}_\theta^2). \tag{3.5.25}$$

5. Monotonicity under quantum channels: For any completely positive, trace-preserving (CPTP) map, i.e., a quantum channel $\mathcal{E}$ that acts on the parameter-dependent state $\hat{\rho}(\theta)$, the quantum Fisher information satisfies:

$$F_Q(\mathcal{E}(\hat{\rho}_\theta), \theta) \leq F_Q(\hat{\rho}_\theta, \theta). \tag{3.5.26}$$

As we will underscore in the future section, quantum channels represent noise, decoherence, or any physical process (e.g., measurement, loss, thermalization). This property can therefore be interpreted as follows. Since a channel cannot create new information about θ from nothing, the QFI can only stay the same (if the channel is reversible on the subspace containing the parameter) or decrease since it quantifies how much information about θ is imprinted in the state. This property is essential for establishing fundamental limits in quantum metrology: noise can only worsen the estimation precision, never improve it. If $\mathcal{E}$ is a projective measurement applied to a quantum state $\hat{\rho}_\theta$, it produces a classical probability distribution from which one can compute the classical Fisher information. This classical Fisher information is always less than or equal to the quantum Fisher information of the original state, with equality achieved only for optimal measurements that saturate the QFI.

3.6 The quantum Cramér-Rao bound

In classical statistics, the variance of any estimator $\tilde{\theta}$ constructed based on a set of measurement outcomes resulting from m trials of measurements carried out on a physical system satisfies the so-called Cramér-Rao bound for classical parameter estimation [60]:

$$(\Delta\tilde{\theta})^2 \geq \frac{1}{mF(\theta)}. \tag{3.6.1}$$

The quantum analogue of this criterion is called the *quantum Cramér-Rao bound* and is based on the quantum Fisher information which results from the optimization process of the classical Fisher information over all possible measurements. In other words, the QFI represents the maximum achievable quantity of information that is extractable from the quantum state containing the unknown parameter θ that we want to estimate. In this quantum context of parameter estimation, the quantum Cramér-Rao bound reads [60]:

$$(\Delta\tilde{\theta})^2 \geq \frac{1}{mF_Q(\theta)}. \tag{3.6.2}$$

Hence, the precision of any quantum measurement strategy is fundamentally limited by the sensitivity of the rate of change of the quantum state $\hat{\rho}(\theta)$ with respect to the encoded parameter. A high degree of precision is therefore achievable if a minor change in θ produces a notable change in its associated density operator. The fundamental nature of the quantum state that encodes the unknown parameter defines the maximum achievable precision that can be reached in such a setting. As emphasized in section 3.1, separable states composed of N independent probes (e.g. qubits) can achieve maximal precision with SQL scaling $1/\sqrt{N}$, whereas entangled states can improve this scaling quadratically to achieve Heisenberg scaling, surpassing the precision of any classical strategy, which provides a crucial advantage in the realm of metrology.

Chapter 4

Noisy quantum metrology

Quantum metrology refers to the branch of quantum science that studies how quantum systems can be employed to estimate physical parameters with the highest possible precision in realistic conditions where unavoidable environmental noise is present. Although an ideal noiseless case of isolated quantum systems can enhance error estimation scaling beyond classical shot-noise limits by exploiting entanglement [39] (allowing us to approach the Heisenberg limit), real systems suffer from decoherence processes such as depolarization, dephasing or particle loss that degrade quantum correlations and reduce the maximal achievable precision.

The quantum Fisher information provides a beneficial mathematical tool to analyze the performance of a given protocol of quantum metrology, by quantifying how much information about the parameter can be retained in the presence of surrounding noise. Key strategies to fight these parasitic effects and maintain the quantum advantage can be incorporated into an ideal strategy, with examples including ancilla-assisted quantum protocols using external resources and careful engineering of the probe state used as a resource, among which anticoherent states play a notable role owing to their isotropic nature, making them less sensitive to directional noise and certain collective decoherence effects. Consequently, anticoherent probe states help preserve quantum resources owing to their intrinsic isotropy, allowing for better stability of estimation precision compared to highly anisotropic entangled states [17]. As a result, noisy quantum metrology becomes the study of balancing entanglement-driven enhancement with noise-induced degradation, while using specially engineered states—such as anticoherent states—to retain as much quantum advantage as possible in practical sensing applications.

4.1 Anticoherent states in quantum metrology

In this section, we review specific applications of anticoherent states in quantum metrology, highlighting how their beneficial properties, such as intrinsic isotropy, can lead to enhanced precision in various realistic scenarios.

4.1.1 Rotation amplitude estimation

A key application of spin anticoherent states concerns arbitrary rotations in three dimensions [19]. For simplicity, we restrain ourselves to the single-parameter simplified situation where we want to estimate the rotation amplitude θ around a reference axis $\mathbf{n} \in \mathbb{R}^3$ that is known before measurement. We will follow a path that is inspired from [19, 34]. Hence, we consider a pure state parameter family that is defined by:

$$|\psi(\theta)\rangle = \hat{R}(\theta, \mathbf{n}) |\psi\rangle , \tag{4.1.1}$$

where we define the unitary rotation operator as:

$$\hat{R}(\theta, \mathbf{n}) = e^{-\frac{i}{\hbar}\theta(\hat{\mathbf{J}}\cdot\mathbf{n})}. \tag{4.1.2}$$

Using this rotation transformation, where the generator is proportional to the projection of the angular momentum operator along the reference axis $\hat{J}_{\mathbf{n}} = (\mathbf{n}\cdot\hat{\mathbf{J}})$, we deduce from (3.5.8) that the computation of the QFI leads to:

$$F_Q(|\psi(\theta)\rangle, \theta, \mathbf{n}) = \frac{4}{\hbar^2}(\Delta_\psi J_{\mathbf{n}})^2. \tag{4.1.3}$$

Consequently, the quantum Cramér-Rao bound can be formulated as:

$$(\Delta\tilde{\theta})^2 \geq \frac{\hbar^2}{4m(\Delta_\psi J_{\mathbf{n}})^2}. \tag{4.1.4}$$

In order to reach the Heisenberg limit, we need to carefully engineer the state to maximize the variance of the projection of the spin operator along the reference axis. For a spin-j system, this can be done by choosing the Greenberger–Horne–Zeilinger state (GHZ) state (which is 1-AC), as the probe:

$$|\mathrm{GHZ}\rangle = \frac{1}{\sqrt{2}}(|j, j\rangle + |j, -j\rangle). \tag{4.1.5}$$

Indeed, by choosing the reference axis $\mathbf{n} = \mathbf{e}_z$, we can compute the variance explicitly, which yields:

$$(\Delta_\psi J_{\mathbf{n}})^2 = \hbar^2 j^2. \tag{4.1.6}$$

This state maximizes the variance along the z-axis. We easily deduce from the identification $N = 2j$ that we reach the Heisenberg limit:

$$(\Delta\tilde{\theta})^2 \sim \frac{1}{N^2}. \tag{4.1.7}$$

The generalization of this problem to estimate a general 3-dimensional rotation, which implies a multiparameter setting (axis and angle of rotation or the Euler angles parametrization), has been explored [19] showed that 2-AC are optimal for this convoluted situation.

4.1.2 Optimal quantum rotosensors

One could also be interested in the complementary problem of the previous situation by considering a rotation of a known angle ϕ around an unknown axis. As for the case of rotation amplitude estimation, we will follow the same path used in a previous work [16]. Hence, the general form of the vector $\mathbf{n} \in \mathbb{R}^3$ can be decomposed in spherical coordinates as:

$$\mathbf{n} = (\cos\varphi\sin\theta, \sin\varphi\sin\theta, \cos\theta). \tag{4.1.8}$$

Thus, the projection of the total spin operator is written as:

$$(\hat{\mathbf{J}}\cdot\mathbf{n}) = (\cos\varphi\sin\theta)\hat{J}_x + (\sin\varphi\sin\theta)\hat{J}_y + \cos\theta\hat{J}_z. \tag{4.1.9}$$

We first consider the simple case where both the rotation angle and axis are known, and we examine the exact same transformation as in the case of rotation amplitude estimation (4.1.1) where the rotation operator is given by (4.1.2). The probability of finding the quantum system in the initial state can be directly mapped to the fidelity between the rotated state and the initial state:

$$F(|\psi\rangle, \hat{R}(\phi, \mathbf{n})|\psi\rangle) = |\langle\psi|\hat{R}(\phi, \mathbf{n})|\psi\rangle|^2. \tag{4.1.10}$$

Since we want to compute the probability of detecting the rotation of angle ϕ around the axis $\mathbf{n}$, we essentially want to maximize the expression:

$$p_{|\psi\rangle}(\phi, \mathbf{n}) = 1 - |\langle\psi|\hat{R}(\phi, \mathbf{n})|\psi\rangle|^2. \tag{4.1.11}$$

In realistic measurement situations, it is possible to encounter a case where the rotation angle is known a priori, while the axis remains unspecified. This scenario typically arises when spins that are initially prepared in a quantum state experience a magnetic field during a measurement process whose directional axis fluctuates randomly over a timescale $\tau > T$ where T is the Larmor period [16]. Consequently, we have to account for the average of the fidelity over all measurement axes in (4.1.10). In other words, we seek quantum pure states $|\psi\rangle$ that minimize the averaged fidelity:

$$\bar{F}(|\psi\rangle, \hat{R}(\phi, \mathbf{n})|\psi\rangle) = \int_{\mathcal{S}^2} F(|\psi\rangle, \hat{R}(\phi, \mathbf{n})|\psi\rangle) d\mathbf{n}. \tag{4.1.12}$$

For small angles, we can expand the rotation operator as:

$$\hat{R}(\phi, \mathbf{n}) \simeq 1 - \frac{i}{\hbar}\phi\hat{J}_{\mathbf{n}} - \frac{1}{2\hbar^2}\phi^2\hat{J}^2_{\mathbf{n}}. \tag{4.1.13}$$

Inserting this relation in the fidelity yields up to the second order:

$$\bar{F}(|\psi\rangle, \hat{R}(\phi, \mathbf{n})|\psi\rangle) \approx \int_{\mathcal{S}^2} \left(1 - \frac{\phi^2}{\hbar^2}(\Delta_\psi J_{\mathbf{n}})^2\right) d\mathbf{n}. \tag{4.1.14}$$

Hence, for the case of small ϕ, we seek to find suitable candidates that maximize the average variance of the projected spin operator. Hence, anticoherent spin states provide excellent candidates and are called optimal quantum rotosensors.

4.2 Noise modeling in quantum metrology

In realistic experimental situations of quantum metrology, the precision with which we want to estimate an unknown parameter θ is inevitably affected by environmental noise. A common problem is fighting the imperfections in the preparation of the initial state of the quantum system under investigation due to coupling with the environment. Hence, a practical, comprehensive description of a quantum protocol should carefully account for decoherence and dissipation effects that will irreparably affect the initially prepared quantum state. These effects often degrade quantum resources, such as entanglement, which are used to reach the Heisenberg limit in correlated quantum scenarios whose goal is the enhancement of parameter estimation.

To describe this loss of information in quantum systems, we will employ the CPTP maps known as quantum channels, introduced in section 1.2.5 to model distinct noise mechanisms. In quantum metrology, incorporating these noisy channels into the system dynamics is essential for accurately evaluating achievable precision limits. Noise can significantly alter the scaling of estimation precision with system size, often reducing the ideal Heisenberg scaling to the standard quantum limit in sufficiently noisy regimes [71]. Consequently, realistic metrological protocols focus not only on optimizing probe states and measurements but also on developing noise-resilient strategies such as error correction [72], adaptive estimation [73], decoherence-free subspaces [74], and robust control techniques [75].

4.2.1 The depolarizing channel

The *depolarizing channel* is a quantum channel that is used to model isotropic noise causing an uniform loss of information through the mixing of a prepared state $\hat{\rho}$ with the maximally mixed state, with probability p called the depolarizing strength. For an Hilbert space of general dimension d, the depolarizing channel reads [24]:

$$\mathcal{E}_{\text{depo}}(\hat{\rho}, p) = (1-p)\hat{\rho} + \frac{p}{d}\hat{\mathbb{1}}_d. \tag{4.2.1}$$

Hence, for full depolarization, we obtain the maximally mixed state associated to the d-dimensional system. This is highlighted by a uniform Husimi Q function in Figure 4.1. In a multipartite system composed of N subsystems, the local depolarization channel acting on subsystem k is defined as:

$$\mathcal{E}^{(k)}_{\text{depo}}(\hat{\rho}, p) = (1-p)\hat{\rho} + p\left(\frac{1}{d_k}\hat{\mathbb{1}}_k \otimes \text{Tr}_k(\hat{\rho})\right). \tag{4.2.2}$$

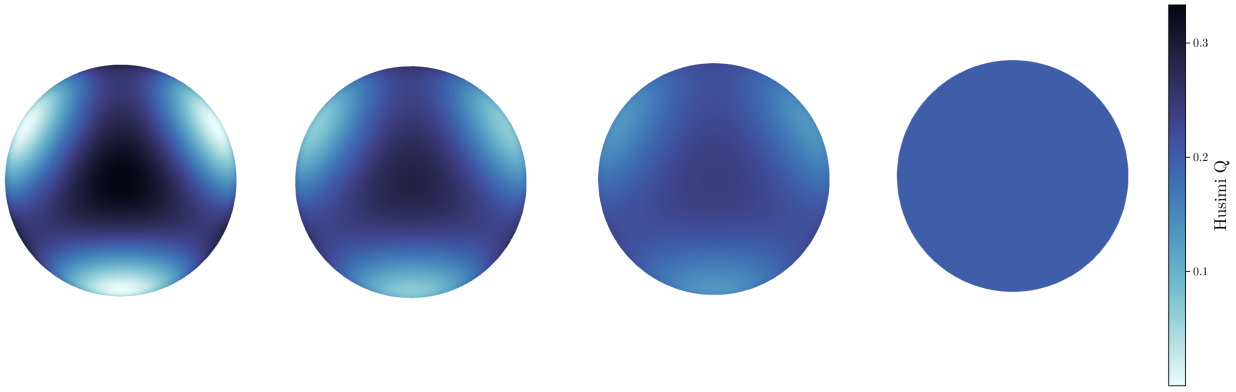

Figure 4.1: Husimi Q function of the depolarized tetrahedron anticoherent state $|\psi_{\text{tetra}}\rangle$ for four different values of the depolarizing strength p. From left to right : $p = 0$, $p = 1/3$, $p = 2/3$, $p = 1$. The tetrahedron state progressively deteriorates to the maximally mixed state, characterized by an uniform Husimi Q function.

We should stress that for depolarized anticoherent states such as the GHZ state or the tetrahedron state, the order of t-anticoherence characterizing these states does not degrade with the depolarization probability p. This result stems from the isotropic nature of the quantum channel. General information on the initial state is lost due to the white noise. However, this loss is uniform in the state and has no directional effect. As a consequence, the intrinsic isotropy contained in the initial state is conserved throughout the depolarization process, which can be seen in Figure 4.2, where the t-order of anticoherence is constant for the tetrahedron state for all possible values of the depolarizing strength.

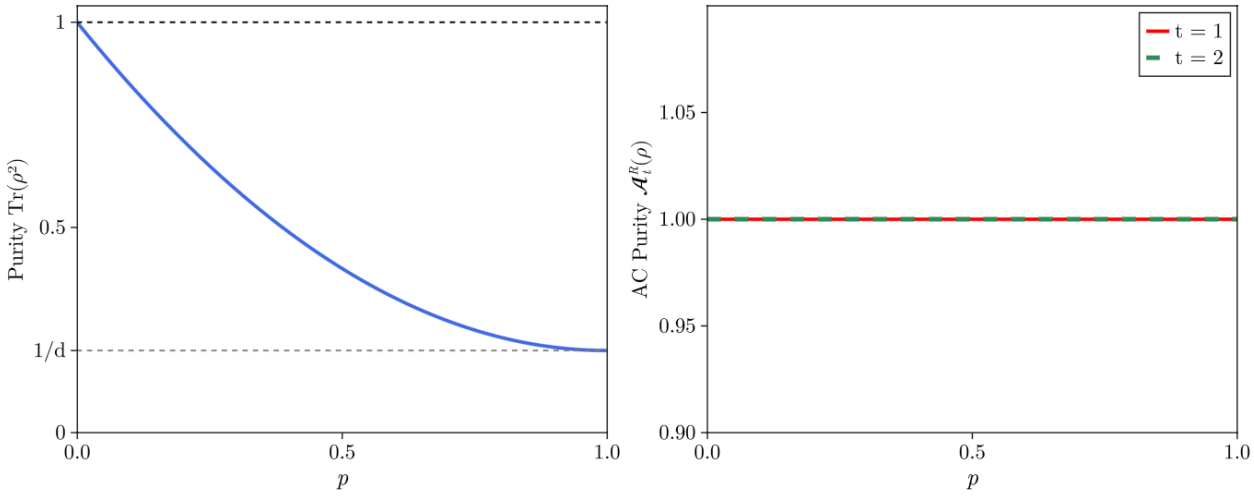

Figure 4.2: Left panel: purity of the depolarized tetrahedron state as a function of the depolarizing strength p. For $p = 1$ we reach the maximally mixed state. Right panel: AC-purity of the depolarized tetrahedron state as a function of the depolarizing strength p. The t-anticoherence is maintained due to the isotropic nature of the depolarizing channel.

4.2.2 The dephasing channel

Another type of quantum channel that describes a different noise mechanism is the *dephasing channel* (or phase damping channel), which is defined by its application on a quantum state in a d-dimensional Hilbert space as [23]:

$$\mathcal{E}_{\text{deph}}(\hat{\rho}, p) = (1-p)\hat{\rho} + p\sum_{i=1}^{d} \langle\chi_i|\hat{\rho}|\chi_i\rangle \, |\chi_i\rangle \langle\chi_i| \,, \tag{4.2.3}$$

where $\{|\chi_i\rangle \,, \;\; i = 1 \ldots, d\}$ defines an orthonormal basis of $\mathcal{H}$, where the quantum state is represented. Physically, this quantum channel destroys the coherences of the quantum state in this basis, while leaving its populations unchanged. Indeed, this can be seen by expanding the quantum state in this basis as:

$$\hat{\rho} = \sum_{i,j=1}^{d} \rho_{ij} \, |\chi_i\rangle \langle\chi_j| \,. \tag{4.2.4}$$

Inserting this expression in the definition of the quantum channel yields:

$$\mathcal{E}_{\text{deph}}(\hat{\rho}, p) = \sum_{i=1}^{d} \rho_i \, |\chi_i\rangle \langle\chi_i| + (1-p) \sum_{\substack{i,j=1 \\ i\neq j}}^{d} \rho_{ij} \, |\chi_i\rangle \langle\chi_j| \,. \tag{4.2.5}$$

For full dephasing ($p = 1$), quantum superpositions are fully destroyed, and only the classical probabilities associated with the basis states $|\chi_i\rangle$ remain. Hence, its matrix is diagonal and corresponds to a classical mixture in the chosen basis, with all interference effects lost. In contrast to the depolarizing channel, the dephasing channel models basis-dependent noise and is therefore directional in the Hilbert space of the system. The preferred basis $\{|\chi_i\rangle \,, \;\; i = 1 \ldots, d\}$ defines the direction in which coherence is destroyed. In the standard angular momentum basis for a spin-j system, the

fully dephased state reads:

$$\mathcal{E}_{\text{deph}}(\hat{\rho}, p = 1) = \sum_{m=-j}^{j} \rho_{mm} \left| j, m \right\rangle \left\langle j, m \right| . \tag{4.2.6}$$

As in the case of depolarization, we can visualize the effects of dephasing by plotting the Husimi Q function of the dephased states for several values of the dephasing probability p. Figure 4.3 displays this effect for the 2-AC tetrahedron state.

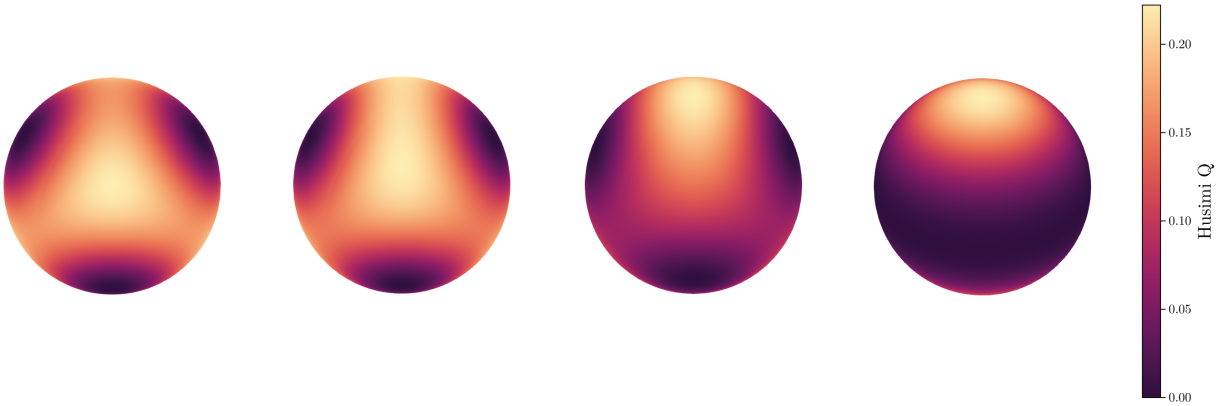

Figure 4.3: Husimi Q function of the dephased tetrahedron anticoherent state $|\psi_{\text{tetra}}\rangle$ for four different values of the dephasing strength p. From left to right : $p = 0$, $p = 1/3$, $p = 2/3$, $p = 1$. The tetrahedron state progressively deteriorates to a classical mixture in the corresponding basis.

In the context of multipartite systems, the local dephasing channel acting on the subsystem k of dimension d_k is defined as:

$$\mathcal{E}^{(k)}_{\text{deph}}(\hat{\rho}, p) = (1 - p)\hat{\rho} + p \sum_{i=1}^{d_k} \hat{P}^{(k)}_i \hat{\rho} \hat{P}^{(k)}_i, \tag{4.2.7}$$

where we defined the projectors:

$$\hat{P}^{(k)}_i = \hat{\mathbb{1}}_1 \otimes \ldots \otimes \hat{\mathbb{1}}_{k-1} \otimes \left| \chi^{(i)}_k \right\rangle \left\langle \chi^{(i)}_k \right| \otimes \hat{\mathbb{1}}_{k+1} \otimes \ldots \otimes \hat{\mathbb{1}}_N, \tag{4.2.8}$$

for all $i = 1, \ldots, d_k$. We should emphasize that in the case of spin anticoherent states, the choice of the basis used to represent the dephasing channel has tremendous consequences on the nature of the dephased state obtained. Indeed, it is possible to conserve the anticoherent nature of the state by choosing the standard angular momentum basis. Figure 4.4 displays this invariance for the 2-AC tetrahedron state. Choosing a generic basis will generally destroy anticoherence as dephasing increases. Throughout numerical simulations and analytical derivations in Chapter 5, we will systematically choose the standard angular momentum basis in order to study the link between the quantum Fisher information and anticoherence.

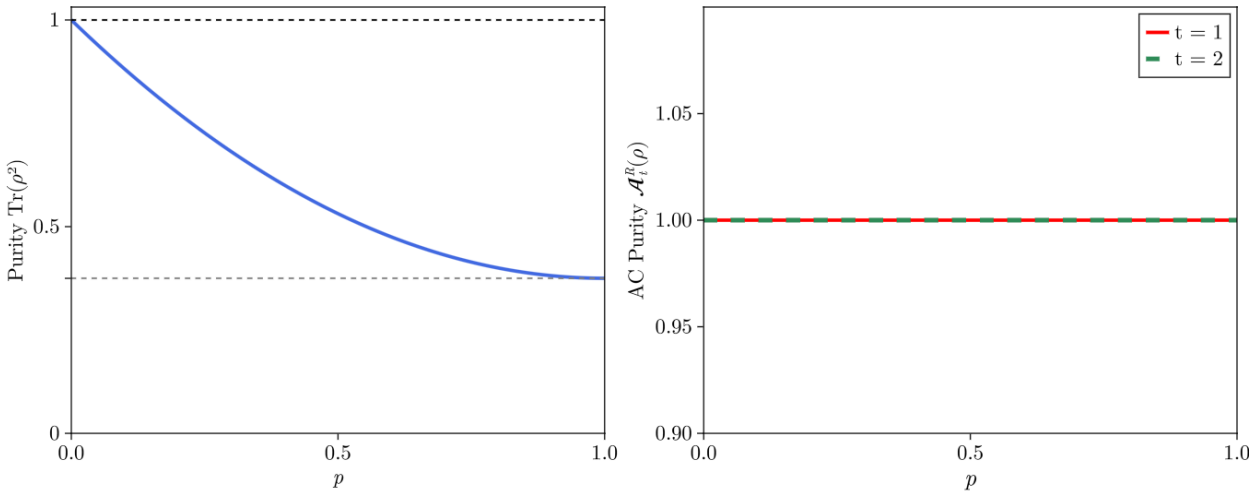

Figure 4.4: Left panel: purity of the dephased tetrahedron state as a function of the dephasing strength p. Right panel: AC-purity of the dephased tetrahedron state as a function of the dephasing strength p. The t-anticoherence is maintained in the standard angular momentum basis due to this convenient choice.

4.3 Optimal measurement and noisy rotation sensing

This section aims to introduce a measurement strategy based on a POVM in order to saturate the quantum Cramér-Rao bound, helping us extract all the information available on the unknown rotation angle θ. The concept of optimal measurement is based on the symmetric logarithmic derivative that we introduced in section 3.4. In fact, an optimal measurement corresponds to a projective measurement in the eigenbasis of the SLD [59]. Starting from a parameter family $\hat{\rho}(\theta)$, one can compute the eigenvalues and eigenvectors of these quantum states in order to insert them into the eigenspace decomposition of the symmetric logarithmic derivative operator. The next step is to diagonalize the SLD. Since $\hat{L}$ is Hermitian, it admits the spectral decomposition (for a qudit):

$$\hat{L}_\theta = \sum_{k=1}^{d} \lambda_k(\theta)\hat{\Pi}_k(\theta), \qquad \hat{\Pi}_k(\theta) = |k(\theta)\rangle \langle k(\theta)|\,, \tag{4.3.1}$$

where $\hat{\Pi}_k(\theta)$ are the projectors onto the eigenstates of $\hat{L}$. Hence, an optimal measurement is given by the projective POVM $\{\hat{\Pi}_k\}$, namely a projective measurement in the eigenbasis of $\hat{L}$ [59]. We can explicitly derive the projectors needed to carry out a projective measurement in this optimal setting for a noisy rotosensing protocol, where a chosen probe state is affected by depolarization and then rotated along a given axis with generator $\hat{J}_z$ and an unknown angle θ. The parameter family is then produced from the protocol shown in Figure 4.5.

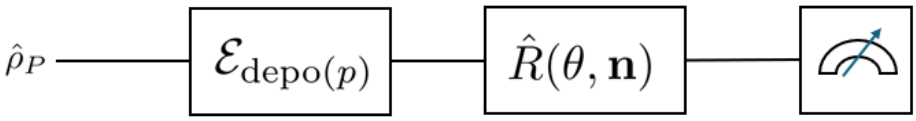

Figure 4.5: Quantum protocol used in rotosensing in the presence of noise modeled by depolarization using a probe state $\hat{\rho}_P$.

We now focus on two examples of anticoherent states used as probe states and we derive explicitly the eigenstates of the SLD.

4.3.1 GHZ probe state

Let us consider the GHZ state (4.1.5) in the general case of N qubits as the probe state. Applying the depolarizing channel with probability p on the density operator $\hat{\rho}_P = |\text{GHZ}\rangle\langle\text{GHZ}|$ yields, by definition:

$$\hat{\rho}_{\text{depo}} = (1-p)\,|\text{GHZ}\rangle\langle\text{GHZ}| + \frac{p}{d}\hat{\mathbb{1}}_d, \tag{4.3.2}$$

where $d = N+1$ is the dimension of the corresponding Hilbert space of the probe state. Using the operator $\hat{R}(\theta) = \exp(-i\theta\hat{J}_z)$ we perform a rotation of angle θ on the depolarized probe state, which transforms as:

$$\hat{\rho}_\theta = \hat{R}(\theta)\hat{\rho}_{\text{depo}}\hat{R}(\theta)^\dagger. \tag{4.3.3}$$

Since the generator is diagonal in the Dicke basis, we have, together with the completeness relation of the standard angular momentum basis, the final density operator:

$$\hat{\rho}_\theta = (1-p)\,|\psi_\theta^+\rangle\langle\psi_\theta^+| + \frac{p}{d}\sum_{m=-j}^{j}|j,m\rangle\langle j,m|\,, \tag{4.3.4}$$

where we used the shorthand notation:

$$|\psi_\theta^+\rangle \equiv \exp(-i\theta\hat{J}_z)\,|\text{GHZ}\rangle = \frac{e^{ij\theta}\,|j,-j\rangle + e^{-ij\theta}\,|j,j\rangle}{\sqrt{2}}. \tag{4.3.5}$$

Diagonalizing the final density operator yields:

$$\begin{cases} |j,m\rangle \quad \forall m \in \{-j+1,\dots,j-1\} \text{ with eigenvalue } \frac{p}{d} \\ |\psi_\theta^+\rangle = \frac{1}{\sqrt{2}}\left(e^{ij\theta}\,|j,-j\rangle + e^{-ij\theta}\,|j,j\rangle\right) \text{ with eigenvalue } (1-p)+\frac{p}{d} \\ |\psi_\theta^-\rangle = \frac{1}{\sqrt{2}}\left(e^{ij\theta}\,|j,-j\rangle - e^{-ij\theta}\,|j,j\rangle\right) \text{ with eigenvalue } \frac{p}{d} \end{cases} \tag{4.3.6}$$

From the eigenspace decomposition of the SLD, it is clear that all diagonal elements vanish in (3.4.9). Furthermore, all terms including $|j,m\rangle$ eigenvectors vanish, either due to equal eigenvalues or because the scalar product involves $\delta_{m,\pm j}$, which is never realized for the range of values of m. Hence, the number of terms to compute is considerably reduced, and we only need to compute two scalar products. The latter being:

$$\langle\psi_\theta^+|\hat{J}_z|\psi_\theta^-\rangle = -\frac{N}{2}, \tag{4.3.7}$$

and its adjoint, which is identical. Inserting these quantities, together with the eigenstates and eigenvalues of the final density operator, yields the following eigenspace expansion of the SLD:

$$\hat{L}_\theta = \underbrace{-N\frac{1-p}{(1-p)+\frac{2p}{d}}}_{=A(p)}\, i\left(|\psi_\theta^+\rangle\langle\psi_\theta^-| - |\psi_\theta^-\rangle\langle\psi_\theta^+|\right). \tag{4.3.8}$$

We can see that $\|\hat{L}_\theta\| \sim N$ which is a direct consequence of the fact that the generator itself scales identically. The last step is to diagonalize the SLD obtained in order to get an explicit form for its eigenvectors. The matrix representation of $\hat{L}_\theta$ is a $d \times d$ matrix that can be brought into the form of a 2×2 matrix containing only the non-vanishing elements since it has a block-diagonal

structure (up to a permutation of rows/columns) in the standard spin basis, which amounts to working in the subspace spanned by the set $\{|-\frac{N}{2}\rangle, |\frac{N}{2}\rangle\}$ of ket vectors, since the $(N-1)\times(N-1)$ remaining block yields the eigenvalue $\lambda = 0$ with multiplicity $N-1$. Hence, one finds the eigenvalues $\lambda_\pm = \pm A(p)$. Thus, we essentially need to find $a, b \in \mathbb{C}$ which satisfy both the normalization condition $|a|^2 + |b|^2 = 1$ and the system:

$$\begin{pmatrix} 0 & e^{iN\theta} \\ -e^{-iN\theta} & 0 \end{pmatrix} \begin{pmatrix} a \\ b \end{pmatrix} = \pm i \begin{pmatrix} a \\ b \end{pmatrix}. \tag{4.3.9}$$

One should therefore compute the two eigenvectors:

$$|\chi_\theta^\pm\rangle = \frac{1}{\sqrt{2}} \left(|j, -j\rangle \pm i e^{-iN\theta} |j, j\rangle \right), \tag{4.3.10}$$

used to carry out projective measurements. Both eigenvectors resemble the GHZ state used and are therefore highly entangled by construction. Consequently, implementing such a projective measurement in an experimental setup is rather difficult owing to the nature of the derived states.

4.3.2 Tetrahedron probe state

We now consider the specific case of $N = 4$ qubits, such that the probe state used in the quantum scheme is the so-called tetrahedron state, which, in the Dicke basis, reads:

$$|\psi_{\text{tetra}}\rangle = \frac{1}{2} \left(|2, -2\rangle + i\sqrt{2} |2, 0\rangle + |2, 2\rangle \right). \tag{4.3.11}$$

Applying depolarization to the density operator constructed based on this probe state yields:

$$\hat{\rho}_{\text{depo}} = (1-p) |\psi_{\text{tetra}}\rangle \langle\psi_{\text{tetra}}| + \frac{p}{d} \hat{\mathbb{1}}_d. \tag{4.3.12}$$

We now perform a rotation of angle θ using a generator $\hat{G} = \hat{J}_z$ through the operator $\hat{R}(\theta) = \exp(-i\theta \hat{J}_z)$. The depolarized probe state hence undergoes the same transformation (4.3.3) as in the case of the GHZ probe state. Using again the fact that the spin operator $\hat{J}_z$ is diagonal in the Dicke basis (where $j = 2$ for the tetrahedron state), we are left with the density operator of the last step before measurement:

$$\hat{\rho}_\theta = (1-p) |\phi_\theta^+\rangle \langle\phi_\theta^+| + \frac{p}{d} \sum_{m=-2}^{2} |2, m\rangle \langle 2, m|, \tag{4.3.13}$$

where we again used a shorthand notation, this time for the state:

$$|\phi_\theta^+\rangle \equiv \exp(-i\theta \hat{J}_z) |\psi_{\text{tetra}}\rangle = \frac{1}{2} \left(e^{2i\theta} |2, -2\rangle + i\sqrt{2} |2, 0\rangle + e^{-2i\theta} |2, 2\rangle \right). \tag{4.3.14}$$

The next step is to compute the $d = 5$ eigenvectors of the last density operator in order to insert them into the logarithmic derivative operator $\hat{L}$ (3.4.9). One therefore computes the set:

$$\begin{cases} |2, \pm 1\rangle \text{ with eigenvalue } \frac{p}{d} \\ |\phi_\theta^+\rangle = \frac{1}{2} \left(e^{2i\theta} |2, -2\rangle + i\sqrt{2} |2, 0\rangle + e^{-2i\theta} |2, 2\rangle \right) \text{ with eigenvalue } (1-p) + \frac{p}{d} \\ |\phi_\theta^-\rangle = \frac{1}{2} \left(e^{2i\theta} |2, -2\rangle - i\sqrt{2} |2, 0\rangle + e^{-2i\theta} |2, 2\rangle \right) \text{ with eigenvalue } \frac{p}{d} \\ |\Omega_\theta\rangle = \frac{1}{\sqrt{2}} \left(|2, -2\rangle - e^{-4i\theta} |2, 2\rangle \right) \text{ with eigenvalue } \frac{p}{d} \end{cases} \tag{4.3.15}$$

From this set, it can be deduced that all combinations involving identical eigenvalues will vanish in (3.4.9). Hence, only combinations in the scalar product involving $|\psi_\theta^+\rangle$ are potentially non zero. Furthermore, using the fact that the Dicke basis is orthogonal, it becomes apparent that any combination involving the states $|2,\pm1\rangle$ vanishes. Finally, one can compute the two useful relations:

$$\begin{cases} \langle\phi_\theta^-|\hat{J}_z|\phi_\theta^+\rangle = 0 \\ \langle\Omega_\theta|\hat{J}_z|\phi_\theta^+\rangle = -\sqrt{2}e^{2i\theta} \end{cases} \tag{4.3.16}$$

One can therefore derive the simplified version of the logarithmic derivative operator:

$$\hat{L}_\theta = \underbrace{2\sqrt{2}\frac{1-p}{(1-p)+\frac{2p}{d}}}_{=B(p)} i\left(e^{2i\theta}\,|\Omega_\theta\rangle\langle\phi_\theta^+| - e^{-2i\theta}\,|\Omega_\theta\rangle\langle\phi_\theta^+|\right). \tag{4.3.17}$$

The last step consists of diagonalizing the term in brackets in order to obtain the eigenvectors of the logarithmic derivative operator. One could compute the matrix form of the eigenvalue equation, where in this case we shall restrict ourselves to the subspace spanned by the set $\{|2,-2\rangle, |2,0\rangle, |2,2\rangle\}$ of spin states. However, since the matrix size is larger compared to the case of the GHZ probe state, we opt for a different approach based on the symmetry of the term in brackets. Indeed, one can define the two entangled ket vectors that are superpositions of the eigenvectors of $\hat{\rho}_\theta$:

$$|\eta_\theta^\pm\rangle = \frac{1}{\sqrt{2}}\left(|\phi_\theta^+\rangle \pm ie^{2i\theta}\,|\Omega_\theta\rangle\right) = \frac{1}{2}\left(e^{2i\theta}(\frac{1}{\sqrt{2}}\pm i)\,|2,-2\rangle + i\,|2,0\rangle + e^{-2i\theta}(\frac{1}{\sqrt{2}}\mp i)\,|2,2\rangle\right). \tag{4.3.18}$$

One can check that these states are indeed eigenvectors of the logarithmic derivative operator with $\lambda_\pm = \pm B(p)$ eigenvalues. Hence, the diagonalized form of (4.3.17) is:

$$\hat{L}_\theta = -2\sqrt{2}\frac{1-p}{(1-p)+\frac{2p}{d}}\left(|\eta_\theta^-\rangle\langle\eta_\theta^-| - |\eta_\theta^+\rangle\langle\eta_\theta^+|\right). \tag{4.3.19}$$

Once again, the eigenstates derived are highly entangled. Nonetheless, a recent paper [76] demonstrates an implementable algorithm for optimal measurement in the noise-free case, which allows us to saturate the quantum Cramér-Rao bound.

4.4 Sub-optimal measurements based on Husimi sampling

Although a full projective measurement of a quantum state $\hat{\rho}(\theta)$ that has been rotated by an unknown parameter θ onto eigenstates is optimal and theoretically possible, implementing this positive-valued measure in a practical experimental setting is challenging. Consequently, it becomes necessary to adopt an alternative approach that is more readily applicable.

An intuitive alternative is provided by [60] and consists of projecting this quantum state onto several coherent states. We present the natural generalization to mixed states. Let us consider the set composed of l coherent states:

$$\{|\mathbf{n}_1\rangle, |\mathbf{n}_2\rangle, \ldots, |\mathbf{n}_l\rangle\}. \tag{4.4.1}$$

The key idea is to determine the rotation of the probe quantum state by computing:

$$q_{\mathbf{n}_m} = \langle\mathbf{n}_m|\hat{\rho}(\theta)|\mathbf{n}_m\rangle, \qquad m = 1,\ldots,l, \tag{4.4.2}$$

which corresponds to a sample of the Husimi Q function evaluated in the $\mathbf{n}_m$ direction. This method amounts to a positive operator-valued measure POVM rather than a PVM, since coherent

states form an overcomplete basis and are therefore not fully distinguishable. Intuitively, computing this projection for every possible direction on the Bloch sphere is equivalent to full tomography. However, this process is redundant. In practice, only a few projections are needed to estimate the unknown parameter with sufficient precision.

For a fixed direction $\mathbf{n}_1 \in \mathbb{R}^3$, the measured value of the projection $q_{\mathbf{n}_1}$ defines an iso-contour on the Bloch sphere called a *level curve* of the Husimi Q function. The probe quantum state must be oriented to ensure that the direction $\mathbf{n}_1$ lies on this curve. Any rotation along this contour leaves the value of the projection invariant. Hence, there is an infinite number of possibilities to align this quantum state along the level curve. To solve this problem, we proceed with a second measurement of the projection $q_{\mathbf{n}_2}$ for a given direction $\mathbf{n}_2$ that will define its own level curve. Possible intersections between the two contours will correspond to valid candidates for potential orientations. A third measurement along another direction generally narrows the number of possibilities to a single intersection corresponding to a specific orientation, unless there are pathological cases. The latter can be avoided by performing a fourth measurement, while a fifth measurement is useful for normalization. Pathological cases can arise in situations where the Husimi Q displays symmetries such that two different directions can yield the same value for their corresponding projection. In order to avoid these problems, we must carefully choose the directions $\mathbf{n}_m$ to break the symmetries. Prior knowledge of the non-rotated Husimi function could also be beneficial to solve these possible issues. Often, the projection values $q_{\mathbf{n}_m}$ are measured with a characteristic uncertainty associated, which widens the level curves into "level-bands". To fight this limitation, one can proceed to perform additional measurements to narrow the number of possible orientations even further. For an infinite number of measurements across every possible direction on the Bloch sphere, we recover full state tomography. In practice, given a set of measured projection values and directions:

$$\{(q_{\mathbf{n}_m}, \mathbf{n}_m), \quad m = 1, \ldots, l\}, \tag{4.4.3}$$

where we suppose $l \geq 4$ as discussed above, one can use an estimation method of their choice to find the rotation angle θ that best aligns the Husimi function of $\hat{\rho}(\theta)$ with the measurements carried out on the quantum system by rigidly rotating the Husimi Q function until all directions $\boldsymbol{n}_m$ lie on their respective level curves and projections.

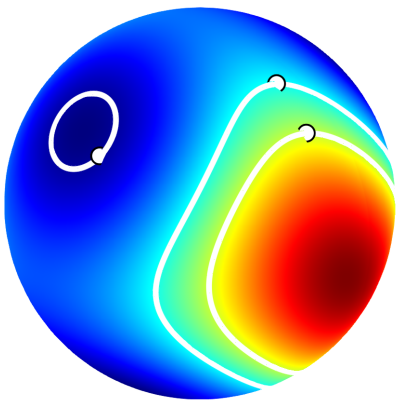

Figure 4.6: Husimi Q function and three level curves represented by the white curves, associated with their respective direction shown by white dots, based on data provided in [60].

Chapter 5

Numerical and analytical investigation of noisy quantum metrology

In this chapter, we investigate both numerically and analytically the behavior of the quantum Fisher information in ancilla-assisted noisy quantum metrological protocols, where anticoherent states are used as probes. We will compute the analytical expression of the QFI in multiple cases in order to interpret physically each situation encountered. For this reason, we will work in natural units where $\hbar = 1$ to simplify the calculations as much as possible. For every numerical simulation carried out, we consider the general qubit state (2.1.2) with equal weight $\alpha = \beta = 1/\sqrt{2}$ for the basis states, such that in the computational basis of the qubit, the density operator representing the ancilla state reads:

$$\hat{\rho}_{\text{anc}} = |+\rangle\langle+|, \qquad |+\rangle = \frac{|0\rangle + |1\rangle}{\sqrt{2}}. \tag{5.0.1}$$

This ancilla state will be entangled with an initially prepared probe state $\hat{\rho}_P$. We will specifically focus on the GHZ state for a spin-j system and the 2-AC tetrahedron state for $j = 2$. Entanglement between the probe state and the ancilla is achieved through the unitary transformation mediated by the unitary operator $\hat{U}(t)$:

$$\hat{\rho}(t) = \hat{U}(t)\hat{\rho}_0\hat{U}^\dagger(t), \tag{5.0.2}$$

where $\hat{\rho}_0$ is the state of the global system (probe-ancilla) before unitary evolution. The unitary operator appearing in this transformation takes the explicit form:

$$\hat{U}(t) = e^{-it\hat{H}}, \tag{5.0.3}$$

where $\hat{H}$ represents a Hamiltonian model of choice. We will specifically focus on two types of models. The first one is the generalized ZZ Hamiltonian (or Ising-type Hamiltonian) model for this qudit-qubit system:

$$\hat{H} = \underbrace{\omega_P(\hat{J}_z \otimes \hat{\mathbb{1}}_{\text{anc}})}_{=\hat{H}_P} + \underbrace{\omega_{\text{anc}}(\hat{\mathbb{1}}_d \otimes \hat{\sigma}_z)}_{=\hat{H}_{\text{anc}}} + \underbrace{g(\hat{J}_z \otimes \hat{\sigma}_z)}_{=\hat{H}_{\text{ZZ}}}, \tag{5.0.4}$$

where $\hat{H}_{\text{anc}}$ and $\hat{H}_P$ are the free Hamiltonians of the qubit and the qudit, which describe the intrinsic energy of the ancilla and the probe state, while $\hat{H}_{\text{ZZ}}$ is a ZZ-type term describing their interaction with a coupling strength g. This Hamiltonian is diagonal in the joint eigenbasis of the operators $\hat{J}_z$ and $\hat{\sigma}_z$ since both operators commute. Entanglement between the probe and the ancilla is contained in relative phases (this is analogous to a controlled-phase type gate). The second type of model

represents an isotropic ZZ interaction along all directions:

$$\hat{H}_{\text{iso}} = h \sum_{\alpha=x,y,z} \hat{J}_\alpha \otimes \hat{\sigma}_\alpha, \tag{5.0.5}$$

with the coupling strength h. Environmental coupling will be described by noisy quantum channels, such as the depolarizing channel and the dephasing channel, both introduced in section 4.2. In a given protocol of quantum metrology, realistic environmental couplings can occur at practically any step of the protocol. Hence, it becomes necessary to investigate the various scenarios. Indeed, we consider three simplistic scenarios to design an ancilla-assisted quantum protocol in quantum metrology:

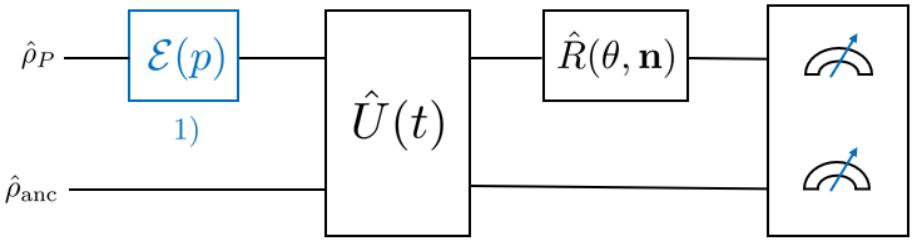

(a) Scenario 1 for an ancilla-assisted protocol, where the degradation of information occurs right after probe state preparation.

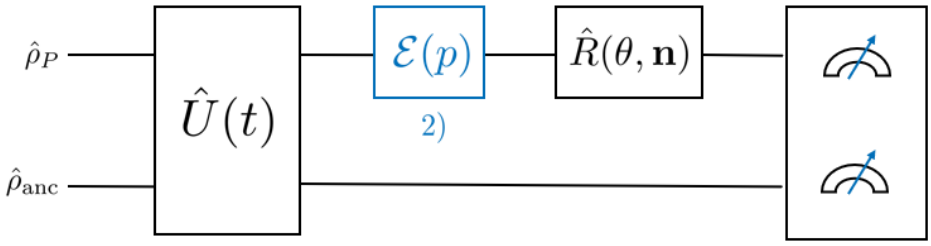

(b) Scenario 2 for ancilla-assisted protocol, where the degradation of information occurs right after unitary evolution of the probe with the ancilla.

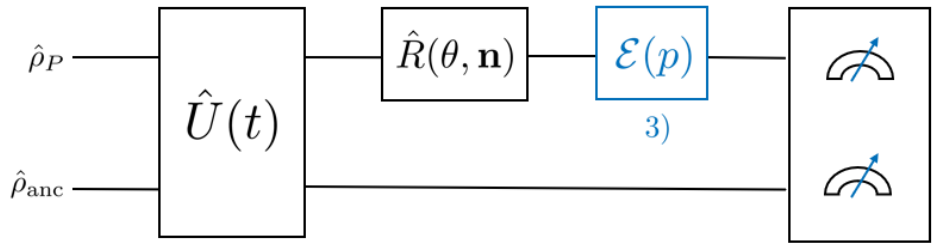

(c) Scenario 3 for ancilla-assisted protocol, where the degradation of information occurs after parameter encoding (here through the rotation operator $\hat{R}(\theta, \mathbf{n})$).

Figure 5.1: Three types of configurations for ancilla-assisted protocols in noisy quantum metrology based on which step is affected by environmental coupling through a quantum channel $\mathcal{E}$. Here, we have chosen the rotation operator $\hat{R}(\theta, \mathbf{n})$ as the encoding gate.

Parameter encoding can be realized in two ways. The first one is done through the rotation

(unitary) operator:

$$\hat{R}(\theta, \mathbf{n}) = e^{-i\theta(\hat{\mathbf{J}}\cdot\mathbf{n})}, \tag{5.0.6}$$

that we apply on the qudit. We will consider projections of the angular momentum operator along the cartesian three dimensional axes. Hence, the components $\hat{J}_x, \hat{J}_y, \hat{J}_z$ will play the role of the generators of the rotation of angle θ. Alternatively, parameter encoding on the qudit can be realized using the spin squeezing operator:

$$\hat{S}(\chi, \mathbf{n}) = e^{-i\frac{\chi}{N}(\hat{\mathbf{J}}\cdot\mathbf{n})^2}, \tag{5.0.7}$$

where χ denotes the dimensionless squeezing strength. Note that the factor $1/N$ is present to ensure that the generator scales linearly with N.

Hence, we investigate the three different possible scenarios for the ancilla-assisted quantum protocols displayed in Figure 5.1. However, we can drastically simplify the number of combinations by taking advantage of the fact that some of the operations/gates that we apply to the system commute with each other. Indeed, the depolarizing channel commutes with the rotation operator (the same reasoning holds for the spin squeezing operator):

$$\begin{aligned}\hat{R}(\theta, \mathbf{n})\mathcal{E}_{\text{depo}}(p, \hat{\rho})\hat{R}^\dagger(\theta, \mathbf{n}) &= (1-p)\hat{R}(\theta, \mathbf{n})\hat{\rho}\hat{R}^\dagger(\theta, \mathbf{n}) + \frac{p}{d}\hat{\mathbb{1}} \\ &= \mathcal{E}_{\text{depo}}\left(p, \hat{R}(\theta, \mathbf{n})\hat{\rho}\hat{R}^\dagger(\theta, \mathbf{n})\right),\end{aligned} \tag{5.0.8}$$

and the dephasing channel, in the sole case of $\mathbf{n} = \mathbf{e}_z$ since the rotation operator is diagonal in this basis in the eigenbasis of $\hat{J}_z$:

$$\begin{aligned}\hat{R}(\theta)\mathcal{E}_{\text{deph}}(p, \hat{\rho})\hat{R}^\dagger(\theta) &= (1-p)\hat{R}(\theta)\hat{\rho}\hat{R}^\dagger(\theta) + p\sum_{m=-j}^{j}\langle j, m|\hat{\rho}|j, m\rangle\, \hat{R}(\theta)\,|j, m\rangle\,\langle j, m|\,\hat{R}^\dagger(\theta) \\ &= (1-p)\hat{R}(\theta)\hat{\rho}\hat{R}^\dagger(\theta) + p\sum_{m=-j}^{j}\langle j, m|\hat{R}(\theta)\hat{\rho}\hat{R}^\dagger(\theta)|jnm\rangle\,|j, m\rangle\,\langle j, m| \\ &= \mathcal{E}_{\text{deph}}\left(p, \hat{R}(\theta)\hat{\rho}\hat{R}^\dagger(\theta)\right).\end{aligned} \tag{5.0.9}$$

The same reasoning can be applied to the spin squeezing operator. Moreover, the dephasing channel also commutes with the unitary operator (5.0.3) for the same reason:

$$\begin{aligned}\hat{U}(t)\mathcal{E}_{\text{deph}}(p, \hat{\rho})\hat{U}^\dagger(t) &= (1-p)\hat{U}(t)\hat{\rho}\hat{U}^\dagger(t) + p\sum_{m=-j}^{d}\langle j, m|\hat{\rho}|j, m\rangle\, \hat{U}(t)\,|j, m\rangle\,\langle j, m|\,\hat{U}^\dagger(t) \\ &= (1-p)\hat{U}(t)\hat{\rho}\hat{U}^\dagger(t) + p\sum_{m=-j}^{d}\langle j, m|\hat{U}(t)\hat{\rho}\hat{U}^\dagger(t)|j, m\rangle\,|j, m\rangle\,\langle j, m| \\ &= \mathcal{E}_{\text{deph}}\left(p, \hat{U}(t)\hat{\rho}\hat{U}^\dagger(t)\right).\end{aligned} \tag{5.0.10}$$

Note that the same results apply to the partial quantum channels. These relations are extremely beneficial and help us reduce the number of possible configurations. The latter have been implemented numerically. In the following sections, we primarily focus on rotation sensing using the rotation operator (5.0.6) in scenarios that reveal the exotic behavior of the QFI in terms of the parameter p characterizing the quantum channels, as well as configurations that lead to Heisenberg scaling, which signals a metrological quantum advantage. Nonetheless, we provide a summary table in section 5.5, containing relevant results of the relevant numerical observations, such as the measurements axes that display Heisenberg scaling for the QFI. This also includes the case where parameter encoding is done through the spin squeezing operator (5.0.7).

5.1 Depolarization prior to unitary evolution

In this section, we cover extensively Scenario 1 in Figure 5.1, specifically for the depolarizing channel (4.2.1) and the Ising-type Hamiltonian (5.0.4). We consider both the GHZ state and the tetrahedron state as probe states for this configuration of the quantum protocol, and we compute the QFI analytically to compare the result to numerical observations.

5.1.1 GHZ probe state

When depolarization occurs on the initially prepared GHZ probe state before entanglement with the ancilla qubit, the QFI associated with a rotation of angle θ around the x/y axis displays a linear increase as a function of the depolarization strength p, for the specific values $gt = \pi/2 + k\pi$ ($k \in \mathbb{Z}$), which is shown in Figure 5.2.

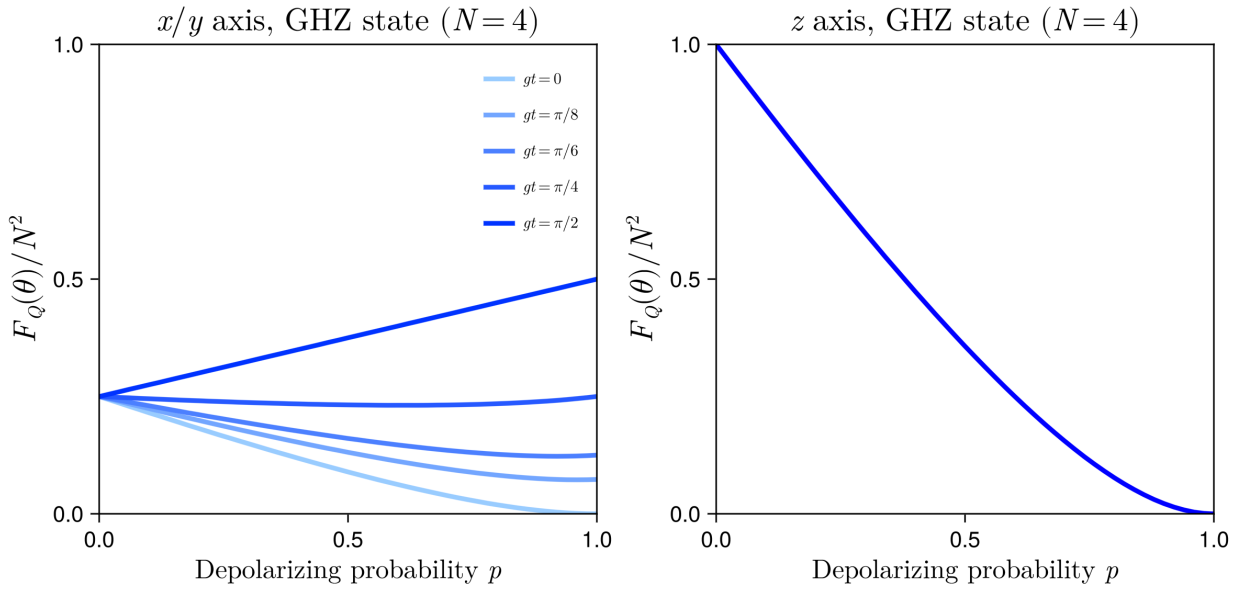

Figure 5.2: Normalized QFI using the GHZ state for $N = 4$ as a probe, entangled with the qubit ancilla state, on which we apply a rotation of angle θ. Left panel: Multiple curves for $gt = 0, \pi/8, \pi/6, \pi/4, \pi/2$ are shown in shades of blue for the x/y-axis. Right panel: Single curve for the z-axis.

This is by far the most exotic behavior of the QFI encountered during the numerical investigation of the protocols. At first glance, the QFI seems to violate its monotonicity property for the x/y axis. However, this is not the case, as the QFI displayed in the figure results from interactions with the ancilla qubit, compared to depolarization occurring solely on the probe state. In contrast, the z-axis does not display any dependence on the dimensionless parameter gt.

Let us compute the quantum Fisher information analytically. We start with the initial pure GHZ state of a spin-j system composed of N qubits by defining the density operator $\hat{\rho}_P = |\text{GHZ}\rangle\langle\text{GHZ}|$, which is subject to depolarization with a probability p:

$$\mathcal{E}_{\text{depo}}(p, \hat{\rho}_P) = (1-p)\hat{\rho}_P + \frac{p}{d}\hat{\mathbb{1}}_d, \tag{5.1.1}$$

with dimension $d = N + 1$. Using the completeness relation (2.2.5) concerning the standard spin basis, we can write the global state of the system after depolarizing the probe state:

$$\hat{\rho}_0 = (1-p)\,|\mathrm{GHZ}\rangle\langle\mathrm{GHZ}| \otimes |+\rangle\langle+| + \frac{p}{N+1}\sum_{m=-j}^{j} |j,m\rangle\langle j,m| \otimes |+\rangle\langle+|\,. \tag{5.1.2}$$

We now apply the unitary transformation (5.0.2) mediated by $\hat{U}(t)$. Hence, we need to compute the unitary evolution of the tensor product of the GHZ state with the ancilla state:

$$\hat{U}(t)\,|\mathrm{GHZ}\rangle\,|+\rangle = e^{-it\hat{H}}\left(\frac{|j,-j\rangle + |j,j\rangle}{\sqrt{2}} \otimes \frac{|0\rangle + |1\rangle}{\sqrt{2}}\right). \tag{5.1.3}$$

By defining the quantum state:

$$|\phi_m(t)\rangle = \frac{e^{-i\omega_P mt}}{\sqrt{2}}\left(e^{-it(\omega_{\mathrm{anc}}+mg)}\,|0\rangle + e^{it(\omega_{\mathrm{anc}}+mg)}\,|1\rangle\right), \tag{5.1.4}$$

for all $m = -j, \ldots, j$, we can write (5.1.3) as:

$$\hat{U}(t)\,|\mathrm{GHZ}\rangle\,|+\rangle = \frac{1}{\sqrt{2}}\left(\left(|j,-j\rangle\,|\phi_{-j}(t)\rangle + |j,j\rangle\,|\phi_j(t)\rangle\right)\right), \tag{5.1.5}$$

which we will refer to as $|\psi(t)\rangle$ to condense the notations. In the same spirit, we have:

$$\hat{U}(t)\,|j,m\rangle\,|+\rangle = |j,m\rangle\,|\phi_m(t)\rangle\,, \tag{5.1.6}$$

where we omit the overall factor appearing induced by $\hat{U}(t)$ since it will irrelevant in the expression of the total state of the system after unitary evolution. Inserting (5.1.5) and (5.1.6) into (5.0.2) yields the total state of the probe-ancilla system after unitary evolution at time t:

$$\hat{\rho}(t) = (1-p)\,|\psi(t)\rangle\langle\psi(t)| + \frac{p}{N+1}\sum_{m=-j}^{j} |j,m\rangle\langle j,m| \otimes |\phi_m(t)\rangle\langle\phi_m(t)|\,. \tag{5.1.7}$$

We now consider a rotation along $\mathbf{n} = \mathbf{e}_y$ (or $\mathbf{e}_x$) such that the final state reads:

$$\hat{\rho}(\theta,t) = (\hat{R}(\theta) \otimes \hat{\mathbb{1}}_2)\hat{\rho}(t)(\hat{R}^\dagger(\theta) \otimes \hat{\mathbb{1}}_2), \tag{5.1.8}$$

which we can write explicitly using the small Wigner d-matrix:

$$\hat{\rho}_\theta(t) = (1-p)\,|\psi_\theta(t)\rangle\langle\psi_\theta(t)| + \frac{p}{2j+1}\sum_{m=-j}^{j} |\delta_m^{(j)}(\theta)\rangle\langle\delta_m^{(j)}(\theta)| \otimes |\phi_m(t)\rangle\langle\phi_m(t)|\,, \tag{5.1.9}$$

using the notations:

$$|\delta_m^{(j)}(\theta)\rangle = \sum_{m'=-j}^{j} d_{m',m}^{(j)}(\theta)\,|j,m\rangle\,, \tag{5.1.10}$$

$$|\psi_\theta(t)\rangle = \frac{1}{\sqrt{2}}(|\delta_{-j}^{(j)}(\theta)\rangle\,|\phi_{-j}(t)\rangle\,|\delta_j^{(j)}(\theta)\rangle\,|\phi_j(t)\rangle). \tag{5.1.11}$$

We now compute the quantum Fisher information using its eigenspace expansion form. To this end, one needs to compute the eigenvectors and the eigenvalues of (5.1.9). This yields:

$$\begin{cases} |\Psi_m(\theta,t)\rangle = |\delta_m^{(j)}(\theta)\rangle \otimes |\phi_m(t)\rangle \qquad \text{with eigenvalue } \frac{p}{2j+1} \\ |\Psi_+(\theta,t)\rangle = \frac{1}{\sqrt{2}}\left(|\delta_j^{(j)}(\theta)\rangle \otimes |\phi_j(t)\rangle + |\delta_{-j}^{(j)}(\theta)\rangle \otimes |\phi_{-j}(t)\rangle\right) \text{ with eigenvalue } (1-p)+\frac{p}{2j+1} \\ |\Psi_-(\theta,t)\rangle = \frac{1}{\sqrt{2}}\left(|\delta_j^{(j)}(\theta)\rangle \otimes |\phi_j(t)\rangle - |\delta_{-j}^{(j)}(\theta)\rangle \otimes |\phi_{-j}(t)\rangle\right) \text{ with eigenvalue } \frac{p}{2j+1} \end{cases} \tag{5.1.12}$$

for all $m \in \{-j+1, \ldots, j-1\}$. These eigenvectors are orthonormal to each other, owing to the relations:

$$\begin{cases} \langle \phi_{m'}(t)|\phi_m(t)\rangle = e^{-i\omega_P(m'-m)t}\cos((m'-m)gt) \\ \langle \delta_{m'}^{(j)}(\theta)|\delta_m^{(j)}(\theta)\rangle = \delta_{m',m} \end{cases} \tag{5.1.13}$$

From (5.1.12), we deduce that the classical contribution (3.5.6) of the total quantum Fisher information vanishes since none of the eigenvalues depend on the unknown parameter θ. This feature appears in every single combination considered in this work. Next, we separate the quantum contribution (3.5.7) of the QFI into two separate terms:

$$F_{\text{quantum}}(\theta) = F_+(\theta) + F_-(\theta), \tag{5.1.14}$$

where r is the rank of the final density operator obtained at the end of the protocol (5.1.9). The positive term appearing in (5.1.14) is given by:

$$F_+(\theta) = 4\sum_{i=1}^{r} \lambda_\theta^{(i)} \langle \partial_\theta \Psi_\theta^{(i)} | \partial_\theta \Psi_\theta^{(i)} \rangle , \tag{5.1.15}$$

and the negative term by:

$$F_-(\theta) = -8\sum_{i,j=1}^{r} \frac{\lambda_\theta^{(i)}\lambda_\theta^{(j)}}{\lambda_\theta^{(i)}+\lambda_\theta^{(j)}} |\langle \Psi_\theta^{(i)} | \partial_\theta \Psi_\theta^{(j)} \rangle|^2. \tag{5.1.16}$$

Naturally, we want to maximize the positive contribution and minimize the negative contribution. During the computation of both contributions, we consider the limit $\theta \to 0$ to analyze the local sensitivity of the state $\hat{\rho}_\theta(t)$ under infinitesimal rotations, where the quantum Fisher information determines the leading-order distinguishability and sets the achievable precision bound.

To calculate the positive contribution, we need to compute derivatives of the eigenvectors of (5.1.9) with respect to θ. One can verify that the following identity holds:

$$\frac{d}{d\theta} d_{m',m}^{(j)}(\theta)\Big|_{\theta=0} = a_{m,j}^{+}\delta_{m',m-1} + a_{m,j}^{-}\delta_{m',m+1}, \tag{5.1.17}$$

where we denote:

$$a_{m,j}^{\pm} = \pm\frac{1}{2}\sqrt{(j\pm m)(j\mp m+1)}. \tag{5.1.18}$$

Hence, the derivatives of the eigenvectors (5.1.12) read:

$$\partial_\theta |\Psi_m(\theta,t)\rangle|_{\theta=0} = \left(a_{m,j}^{+}|j,m-1\rangle + a_{m,j}^{-}|j,m+1\rangle\right) \otimes |\phi_m(t)\rangle , \tag{5.1.19}$$

$$\partial_\theta |\Psi_\pm(\theta,t)\rangle|_{\theta=0} = \sqrt{\frac{j}{4}}\left(|j,j-1\rangle|\phi_j(t)\rangle \mp |j,j+1\rangle|\phi_{-j}(t)\rangle\right), \tag{5.1.20}$$

for all $m = -j, \dots, j$. One therefore computes the following inner products:

$$\begin{cases} \langle \partial_\theta \Psi_m(\theta,t) | \partial_\theta \Psi_m(\theta,t) \rangle|_{\theta=0} = \frac{1}{2}(j(j+1) - m^2) \\ \langle \partial_\theta \Psi_\pm(\theta,t) | \partial_\theta \Psi_\pm(\theta,t) \rangle|_{\theta=0} = \frac{j}{2} \end{cases} \tag{5.1.21}$$

We can use the following series:

$$\sum_{m=-j+1}^{j-1} m^2 = \frac{j(j-1)(2j-1)}{3}. \tag{5.1.22}$$

Hence, the positive contribution (5.1.15) reads:

$$F_+(p) = N + \frac{1}{3} pN(N-1). \tag{5.1.23}$$

We now focus on the computation of the negative contribution (5.1.16) of the QFI. Using the derivatives of the eigenvectors (5.1.19)(5.1.20), one derives the cross inner products:

$$\begin{cases} \langle \Psi_m | \partial_\theta \Psi_{m'} \rangle|_{\theta=0} = e^{-i\omega_P (m'-m)t} \cos((m'-m)gt) \\ \qquad\qquad \times \left(a^+_{m',j} \delta_{m,m'-1} + a^-_{m',j} \delta_{m,m'+1} \right) \\ \langle \Psi_\pm | \partial_\theta \Psi_m \rangle|_{\theta=0} = \frac{1}{\sqrt{2}} \Big[e^{-i\omega_P (j-m)t} \cos((j-m)gt) a^-_{m',j} \delta_{j,m+1} \\ \qquad\qquad - e^{i\omega_P (j+m)t} \cos((j+m)gt) a^+_{m',j} \delta_{-j,m-1} \Big] \\ \langle \Psi_m | \partial_\theta \Psi_\pm \rangle|_{\theta=0} = \sqrt{\frac{j}{4}} \Big[e^{-i\omega_P (j-m)t} \cos((j-m)gt) \delta_{m,j-1} \\ \qquad\qquad \mp e^{i\omega_P (j+m)t} \cos((j+m)gt) \delta_{m,-j+1} \Big] \\ \langle \Psi_\pm | \partial_\theta \Psi_\pm \rangle|_{\theta=0} = 0 \end{cases} \tag{5.1.24}$$

Inserting these inner products in (5.1.16) yields, after algebraic simplifications, the final expression for the negative contribution:

$$F_-(p, gt) = -\frac{1}{3} \cos^2(gt) Np \frac{4(p-2) + N(N(p-1) + p - 3)}{p(N-1) - (N+1)}, \tag{5.1.25}$$

which displays a dependence on time t and the coupling strength g. This dependence is shown in Figure 5.3, as well as the positive and negative contributions of the QFI. Note that the QFI is completely independent of the free energy of the probe and the ancilla (which is also observed numerically), and that for $gt = \pi/2 + k\pi$ ($k \in \mathbb{Z}$) we minimize this term since it vanishes for these specific values, and the total quantum Fisher corresponds to $F_+(\theta)$, which explains the linear increase in terms of p that is observed. Moreover, we can reach the Heisenberg limit for the x and y axes in the presence of noise owing to the interaction with the ancilla, which is a notable improvement over the standard case where the GHZ state undergoes depolarization and then parameter encoding.

The QFI is maximal at full polarization $p = 1$, which is equivalent to replacing the depolarized GHZ state by the maximally mixed state, such that:

$$\hat{\rho}_0 = \frac{1}{d} \hat{\mathbb{1}}_d \otimes \hat{\rho}_{\text{anc}}. \tag{5.1.26}$$

The behavior of the QFI for the z-axis can be derived much more simply. Indeed, for the generator $\hat{J}_z$, the rotation operator $\hat{R}(\theta)$ is diagonal in the standard spin basis. From (5.1.7), we obtain:

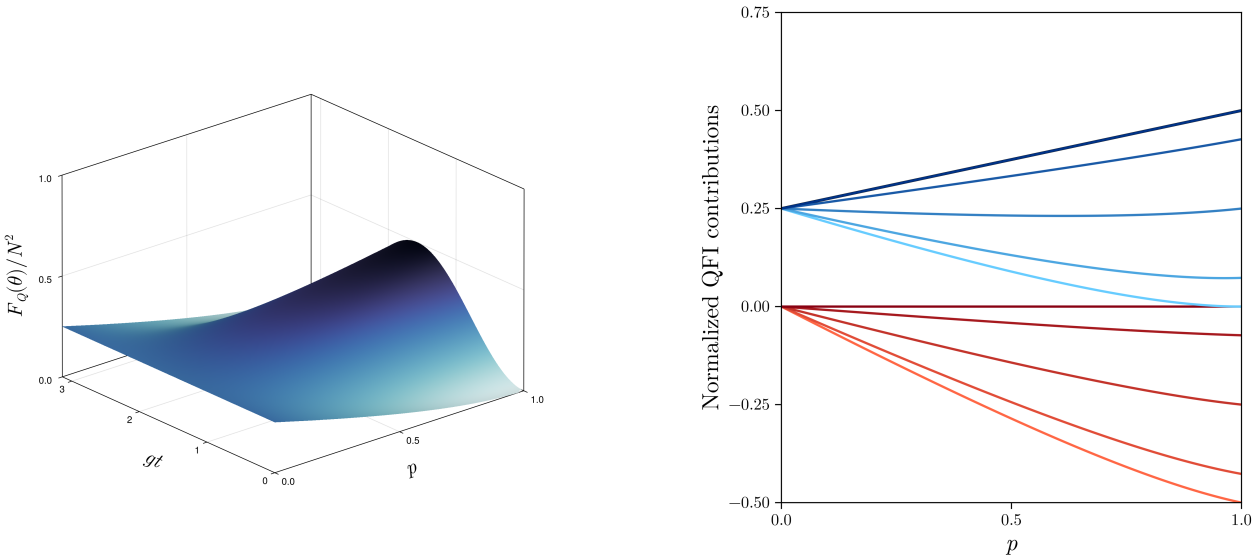

Figure 5.3: Left panel: Normalized QFI for the GHZ state ($N = 4$) for the x/y axis as a function of the dimensionless parameter gt and the parameter p. Right panel: Curves of the contributions of the QFI for successive values of gt. The black curve represents the positive contribution, whereas the blue curves represent the total QFI. Red curves represent the negative contribution, for the GHZ state ($N = 4$) for the x/y axis as a function of the dimensionless parameter gt.

$$\hat{\rho}_\theta(t) = (1-p)\,|\psi_\theta(t)\rangle\langle\psi_\theta(t)| + \frac{p}{2j+1}\sum_{m=-j}^{j} |j,m\rangle\langle j,m| \otimes |\phi_m(t)\rangle\langle\phi_m(t)|\,, \tag{5.1.27}$$

where this time the ket vector $|\psi_\theta(t)\rangle$ takes the simple form:

$$|\psi_\theta(t)\rangle = \frac{1}{\sqrt{2}}(e^{-ij\theta}\,|j,j\rangle\,|\phi_j(t)\rangle + e^{ij\theta}\,|j,-j\rangle\,|\phi_{-j}(t)\rangle). \tag{5.1.28}$$

Diagonalizing this density operator yields the set of eigenvectors and eigenvalues:

$$\begin{cases} |\Psi_m(\theta,t)\rangle = |j,m\rangle \otimes |\phi_m(t)\rangle \text{ with eigenvalue } \frac{p}{2j+1} \\ |\Psi_+(\theta,t)\rangle = \frac{1}{\sqrt{2}}(e^{-ij\theta}\,|j,j\rangle\,|\phi_j(t)\rangle + e^{ij\theta}\,|j,-j\rangle\,|\phi_{-j}(t)\rangle) \text{ with eigenvalue } (1-p)+\frac{p}{2j+1} \\ |\Psi_-(\theta,t)\rangle = \frac{1}{\sqrt{2}}(e^{-ij\theta}\,|j,j\rangle\,|\phi_j(t)\rangle - e^{ij\theta}\,|j,-j\rangle\,|\phi_{-j}(t)\rangle) \text{ with eigenvalue } \frac{p}{2j+1} \end{cases} \tag{5.1.29}$$

for all $m \in \{-j+1,\ldots,j-1\}$. Using the following derivatives:

$$\begin{cases} \partial_\theta\,|\Psi_m(\theta,t)\rangle = -im\,|\Psi_m(\theta,t)\rangle \\ \partial_\theta\,|\Psi_\pm(\theta,t)\rangle = -ij\,|\Psi_\pm(\theta,t)\rangle \end{cases} \tag{5.1.30}$$

One computes the total quantum Fisher information:

$$F_Q(p) = N^2\frac{(N+1)(1-p)^2}{N+1-p(N-1)}. \tag{5.1.31}$$

which clearly displays Heisenberg scaling as well (this is unchanged from the situation without an ancilla), although for the z-axis, the QFI worsens as depolarization increases, and displays no dependence in terms of the dimensionless parameter gt, which is also supported by numerical observations.

5.1.2 Tetrahedron probe state study

We can reiterate the same quantum protocol, this time swapping the GHZ state for the tetrahedron state (2.4.5) for $j = 2$. In order to quantify how the total quantum Fisher information scales, we can instead focus on the family of pure quantum states:

$$|\psi\rangle = \frac{1}{2}(|j,j\rangle + i\sqrt{2}\,|j,0\rangle + |j,-j\rangle), \tag{5.1.32}$$

for a general spin-j system. Hence, we simply recover the tetrahedron state for the case $j = 2$. Unlike the case of the GHZ state, the total quantum Fisher information displays no dependence on the depolarization strength p for the x/y-axis for the same set of values $gt = \pi/2 + k\pi$ $(k \in \mathbb{Z})$, as shown in Figure 5.4.

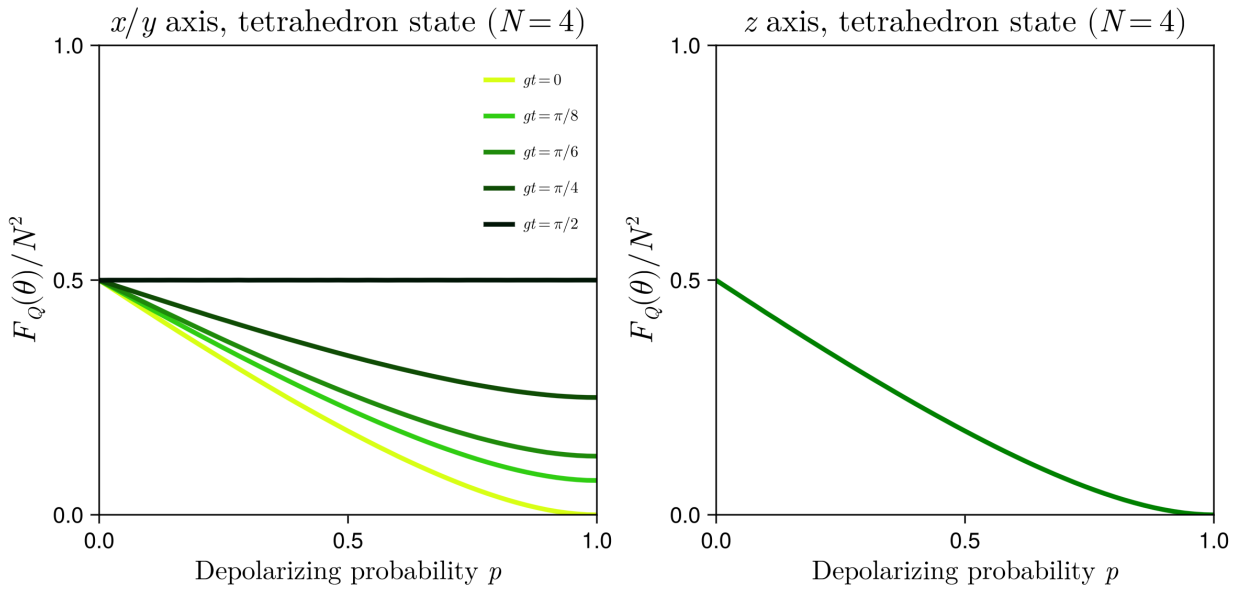

Figure 5.4: Normalized QFI using the tetrahedron state for $N = 4$ as a probe, entangled with the qubit ancilla state, on which we apply a rotation of angle θ. Multiple curves for $gt = 0, \pi/8, \pi/6, \pi/4, \pi/2$ are shown in shades of green for the x/y-axis.

To see this characteristic, let us compute the quantum Fisher information explicitly. The depolarized probe state reads:

$$\mathcal{E}_{\text{depo}}(p, \hat{\rho}_P) = (1-p)\,|\psi\rangle\langle\psi| + \frac{p}{d}\hat{\mathbb{1}}_d. \tag{5.1.33}$$

Again, using the completeness relation (2.2.5) concerning the standard angular momentum basis, we can write the global state of the system after depolarization:

$$\hat{\rho}_0 = (1-p)\,|\psi\rangle\langle\psi| \otimes |+\rangle\langle+| + \frac{p}{N+1}\sum_{m=-j}^{j} |j,m\rangle\langle j,m| \otimes |+\rangle\langle+|\,. \tag{5.1.34}$$

Similarly to the GHZ probe state, we need to compute the following quantity to express the total state of the system after unitary evolution:

$$\hat{U}(t)\,|\psi\rangle\,|+\rangle = e^{-it\hat{H}}\left(\frac{|j,-j\rangle + i\sqrt{2}\,|j,0\rangle + |j,j\rangle}{2} \otimes \frac{|0\rangle + |1\rangle}{\sqrt{2}}\right). \tag{5.1.35}$$

Using the same definition (5.1.4) for the $|\phi_m(t)\rangle$ states, we can write this expression as:

$$\hat{U}(t)\,|\psi\rangle\,|+\rangle \equiv |\psi'(t)\rangle = \frac{1}{2}\left((|j,-j\rangle\,|\phi_{-j}(t)\rangle + i\sqrt{2}\,|j,0\rangle\,|\phi_0(t)\rangle\,|j,j\rangle\,|\phi_j(t)\rangle\right), \tag{5.1.36}$$

which we will refer to as $|\psi'(t)\rangle$ to condense notations. Additionally, we can use the relation (5.1.6) that was derived in section 5.1.1. Hence, the total state of the system after unitary evolution with time t reads:

$$\hat{\rho}(t) = (1-p)\,|\psi'(t)\rangle\,\langle\psi'(t)| + \frac{p}{N+1}\sum_{m=-j}^{j} |j,m\rangle\,\langle j,m| \otimes |\phi_m(t)\rangle\,\langle\phi_m(t)|\,. \tag{5.1.37}$$

We now consider a rotation along $\mathbf{n} = \mathbf{e}_y$ (or $\mathbf{e}_x$ equivalently). The rotation transformation of (5.1.37) reads:

$$\begin{aligned}\hat{\rho}_\theta(t) = (1-p)\hat{R}(\theta)\,|\psi'(t)\rangle\,\langle\psi'(t)|\,\hat{R}^\dagger(\theta) \\ + \frac{p}{2j+1}\sum_{m=-j}^{j} \hat{R}(\theta)\,|j,m\rangle\,\langle j,m|\,\hat{R}^\dagger(\theta) \otimes |\phi_m(t)\rangle\,\langle\phi_m(t)|\,.\end{aligned} \tag{5.1.38}$$

We could use the small Wigner d-matrix as in the case of the GHZ, but we instead consider a different yet equivalent approach. The eigenvectors of (5.1.38) can be written in the following form:

$$|\Psi_i(\theta,t)\rangle = \hat{R}(\theta)\,|\Phi_i(t)\rangle\,, \tag{5.1.39}$$

where we define the set of eigenvectors and eigenvalues of (5.1.37):

$$\begin{cases} |\Phi(t)\rangle = |\psi'(t)\rangle \text{ with eigenvalue } (1-p) + \frac{p}{2j+1} \\ |\Phi_m(t)\rangle = |j,m\rangle\,|\phi_m\rangle \text{ with eigenvalue } \frac{p}{2j+1} \end{cases} \tag{5.1.40}$$

for m taking any value between $-j+1$ and $j-1$ besides 0. Note that we have the identity:

$$\partial_\theta\,|\Psi_i(\theta,t)\rangle = -i(\hat{J}_y \otimes \hat{\mathbb{1}})\,|\Psi_i(\theta,t)\rangle\,, \tag{5.1.41}$$

which tremendously simplifies the computation of the inner products that have to be inserted to compute the positive contribution (5.1.15) and negative contributions (5.1.16) of the QFI. Indeed, because the rotation operator trivially commutes with its generator, we have:

$$\langle\partial_\theta\Psi_i(\theta,t)|\partial_\theta\Psi_i(\theta,t)\rangle = \langle\Phi_i|\hat{J}_y^2|\Phi_i\rangle\,. \tag{5.1.42}$$

Hence, for the positive contribution we have:

$$\langle\partial_\theta\Psi(\theta,t)|\partial_\theta\Psi(\theta,t)\rangle = \begin{cases} \frac{3}{4} - \frac{1}{4}\cos(2\omega_P t)\cos(2gt) & j=1 \\ \frac{j(j+2)}{4} & j\geq 2 \end{cases} \tag{5.1.43}$$

Note that for the sole case $j=1$, the QFI will depend on the free energy of the probe state. Furthermore, we can compute:

$$\langle\partial_\theta\Psi_m(\theta,t)|\partial_\theta\Psi_m(\theta,t)\rangle = j(j+1) - m^2. \tag{5.1.44}$$

Hence, the positive contribution of the QFI reads:

$$F_+(\theta) = \begin{cases} 3 - \left(1 - \frac{2p}{3}\right)\cos(2\omega_P t)\cos(2gt) & j=1 \\ j(j+2) + p\frac{j(j-2)}{3} & j\geq 2 \end{cases} \tag{5.1.45}$$

Surprisingly, we see that this term is constant with respect to p for the sole case $j = 2$, which coincides with the tetrahedron state. For the negative contribution, we first note that:

$$\langle \Psi_i(\theta,t)|\partial_\theta \Psi_k(\theta,t)\rangle = -i\,\langle \Phi_i|\hat{J}_y|\Phi_k\rangle\,, \tag{5.1.46}$$

which can be easily computed owing to orthogonality of the standard angular momentum basis and the decomposition of $\hat{J}_y$ using ladder operators (2.2.6). Therefore, the negative contribution reads for $j \geq 2$:

$$F_-(\theta) = -2p\cos^2(gt)\left(\frac{2j(j+1)}{3} + \frac{(1-p)j(j+2)}{2j+1-p(2j-1)}\right). \tag{5.1.47}$$

Finally, the total quantum Fisher information for the x/y axis reads for $j \geq 2$:

$$F_Q(\theta) = \frac{N(N+4)}{4} + p\frac{N(N-4)}{12} - 2p\cos^2(gt)\left(\frac{N(N+2)}{6} + \frac{1}{4}\frac{(1-p)N(N+4)}{N(1-p)+1+p}\right). \tag{5.1.48}$$

Hence, we maintain the quantum advantage using the ancilla setup. The total QFI is represented in Figure 5.5, as well as the positive and negative contributions.

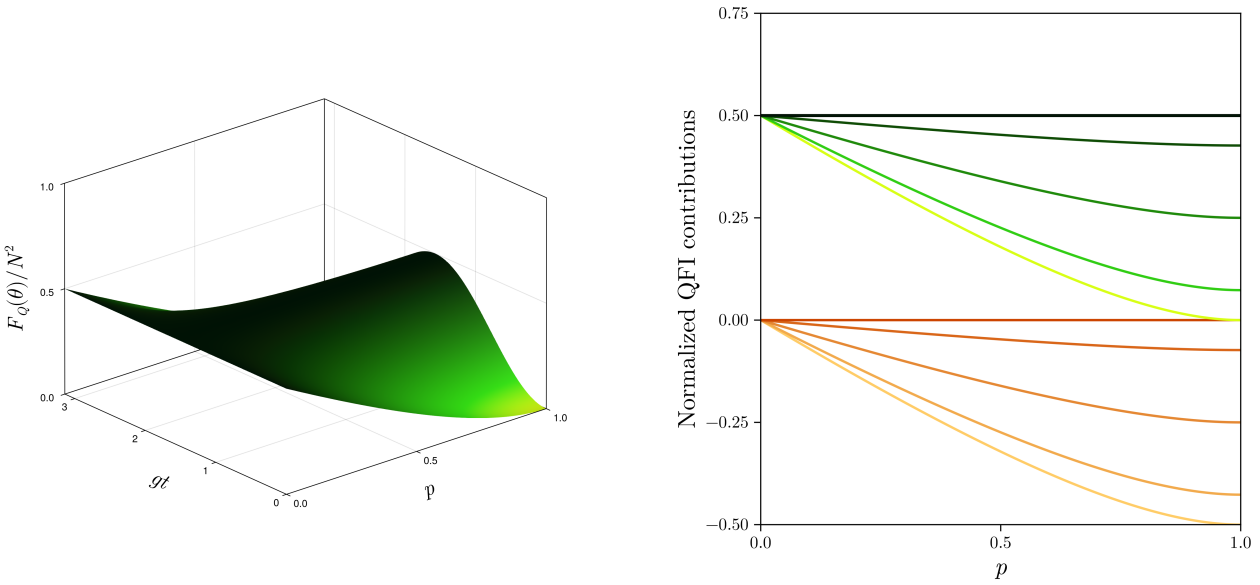

Figure 5.5: Left panel: Normalized QFI for the tetrahedron state ($N = 4$) for the x/y-axis as a function of the dimensionless parameter gt and the parameter p. Right panel: Curves of the contributions of the QFI for successive values of gt. The black curve represents the positive contribution of the QFI, whereas the green curves represent the total QFI. Orange curves represent the negative contribution, for the tetrahedron state ($N = 4$) for the x/y axis as a function of the dimensionless parameter gt.

As in the case of the GHZ probe state, the quantum Fisher information for the z-axis can be computed in a straightforward manner. Indeed, choosing the generator $\hat{J}_z$ in the final density

operator and diagonalizing the latter yields:

$$\begin{cases} |\Psi_\theta\rangle = \frac{1}{2}\left(e^{i\theta j}\,|j,-j\rangle\,|\phi_{-j}(t)\rangle + i\sqrt{2}\,|j,0\rangle\,|\phi_0(t)\rangle + e^{-i\theta j}\,|j,j\rangle\,|\phi_j(t)\rangle\right) \text{ with eigenvalue } (1-p)+\frac{p}{d} \\ |\Psi_m\rangle = |j,m\rangle\,|\phi_m\rangle \text{ with eigenvalue } \frac{p}{d} \\ |\chi_\theta\rangle = \frac{1}{\sqrt{2}}\left(|j,-j\rangle\,|\phi_{-j}(t)\rangle + e^{-2i\theta j}\,|j,j\rangle\,|\phi_j(t)\rangle\right) \text{ with eigenvalue } \frac{p}{d} \\ |\Omega_\theta\rangle = \sqrt{2}\,|j,0\rangle\,|\phi_0\rangle + i\,|\Psi_\theta\rangle \text{ with eigenvalue } \frac{p}{d} \end{cases} \tag{5.1.49}$$

for all m values between $j-1$ and $-j+1$ besides 0. The partial derivatives of these eigenvectors read:

$$\begin{cases} \partial_\theta\,|\Psi_\theta\rangle = \frac{ij}{2}\left(e^{i\theta j}\,|j,-j\rangle\,|\phi_{-j}(t)\rangle + e^{-i\theta j}\,|j,j\rangle\,|\phi_j(t)\rangle\right) \\ \partial_\theta\,|\Psi_m\rangle = 0 \\ \partial_\theta\,|\chi_\theta\rangle = -ij\sqrt{2}e^{-2i\theta j}\,|j,j\rangle\,|\phi_j(t)\rangle \\ \partial_\theta\,|\Omega_\theta\rangle = i\partial_\theta\,|\Psi_\theta\rangle \end{cases} \tag{5.1.50}$$

For the positive contribution of the QFI, we insert the inner products:

$$\begin{cases} \langle\partial_\theta\Psi_\theta|\partial_\theta\Psi_\theta\rangle = \frac{j^2}{2} \\ \langle\partial_\theta\chi_\theta|\partial_\theta\chi_\theta\rangle = 2j^2 \\ \langle\partial_\theta\Omega_\theta|\partial_\theta\Omega_\theta\rangle = \frac{j^2}{2} \end{cases} \tag{5.1.51}$$

which yields:

$$F_+(\theta) = \frac{N}{2}(1-p) + \frac{3N^2p}{N+1}. \tag{5.1.52}$$

For the negative contributions, we use:

$$\begin{cases} \langle\Psi_\theta|\partial_\theta\chi_\theta\rangle = \frac{-ij}{\sqrt{2}}e^{ij\theta} \\ \langle\chi_\theta|\partial_\theta\Psi_\theta\rangle = \frac{-ij}{\sqrt{2}}e^{-ij\theta} \\ \langle\chi_\theta|\partial_\theta\chi_\theta\rangle = ij \\ \langle\chi_\theta|\partial_\theta\Omega_\theta\rangle = \frac{j}{\sqrt{2}}e^{-ij\theta} \\ \langle\Omega_\theta|\partial_\theta\chi_\theta\rangle = -\frac{j}{\sqrt{2}}e^{ij\theta} \end{cases} \tag{5.1.53}$$

which yields the negative contribution:

$$F_-(\theta) = \frac{2N^2p(2(N+1)-p(2N-1))}{(N+1)((N+1)-p(N-1))}. \tag{5.1.54}$$

Hence, the total QFI reads :

$$F_Q(\theta) = N^2\frac{(N+1)(1-p)^2}{2(N+1-p(N-1))}, \tag{5.1.55}$$

which reveals Heisenberg scaling as in the case with no ancilla qubit. The total QFI, as well as the positive and negative contributions are displayed in Figure 5.5.

5.1.3 Link between anticoherence and metrological advantage

In Scenario 1 (displayed in Figure 5.1), where depolarization occurs on the probe state before unitary evolution, two types of probe states were considered. The GHZ state, which is 1-AC, and

the tetrahedron state, which is 2-AC. There is a notable difference in the behavior of the QFI for the x/y-axis when we compare both probe states. In both cases, after unitary evolution, we obtained a density operator of the form:

$$\hat{\rho}_\theta(t) = (1-p)\hat{R}(\theta)\left|\psi_P(t)\right\rangle\left\langle\psi_P(t)\right|\hat{R}^\dagger(\theta) + \frac{p}{2j+1}\sum_{m=-j}^{j}\hat{R}(\theta)\left|j,m\right\rangle\left\langle j,m\right|\hat{R}^\dagger(\theta)\otimes\left|\phi_m(t)\right\rangle\left\langle\phi_m(t)\right|, \tag{5.1.56}$$

where in this relation, $|\psi_P(t)\rangle$ actually depends on the probe state used. Using the convexity of the QFI, we can write:

$$F_Q(\theta,\hat{\rho}_\theta(t)) \leq (1-p)F_Q(\theta,|\psi_P(\theta)\rangle) + \frac{p}{2j+1}\sum_{m=-j}^{j}F_Q(\theta,|\psi_m(\theta)\rangle), \tag{5.1.57}$$

with:

$$|\psi_m(\theta)\rangle = \hat{R}(\theta)\left|j,m\right\rangle\left|\phi_m(t)\right\rangle, \tag{5.1.58}$$

stemming from the maximally mixed state contribution induced by the depolarizing channel. Note that for $gt = \pi/2 + k\pi$ ($k \in \mathbb{Z}$), neighbor states $|\phi_m(t)\rangle$ are orthogonal:

$$\langle\phi_m|\phi_{m+1}\rangle = 0. \tag{5.1.59}$$

However, the generator $\hat{G} = \hat{J}_\alpha$ for $\alpha = x, y$ only connects neighbors states with $m' - m = \pm 1$, but because of the orthogonality condition obtained for the $|\phi_m\rangle$ ket vectors, the generator maps every eigenstate of $\hat{\rho}(t)$ to a ket vector orthogonal to its entire support. Consequently, the strict equality holds for the convexity of the QFI, and we can simply decompose the latter as a sum. Using invariance under unitary transformation for pure states, we get:

$$F(\theta,\hat{\rho}_\theta(t)) = 4(1-p)(\Delta_{\psi_P}G)^2 + \frac{4p}{2j+1}\sum_{m=-j}^{j}(\Delta_{j,m}G)^2, \tag{5.1.60}$$

where we have:

$$\sum_{m=-j}^{j}(\Delta_{j,m}G)^2 = \frac{1}{2}\sum_{m=-j}^{j}(j(j+1)-m^2) = (2j+1)\frac{j(j+1)}{3}. \tag{5.1.61}$$

Hence, we can simplify the total quantum Fisher information as:

$$F_Q(\theta,\hat{\rho}_\theta(t)) = 4(\Delta_{\psi_P}\hat{G})^2 + 4p\left(\frac{j(j+1)}{3} - (\Delta_{\psi_P}G)^2\right). \tag{5.1.62}$$

Consequently, we deduce that for $\alpha = x, y$:

1. The quantum Fisher information strictly increases with depolarization probability p if:

$$(\Delta_{\psi_P}J_\alpha)^2 < \frac{j(j+1)}{3}. \tag{5.1.63}$$

2. The quantum Fisher information is completely independent of the depolarization probability p if:

$$(\Delta_{\psi_P}J_\alpha)^2 = \frac{j(j+1)}{3}. \tag{5.1.64}$$

The GHZ state, which is 1-AC, satisfies the first property, whereas the tetrahedron state, which is 2-AC, satisfies the second property. Moreover, the family of states containing the tetrahedron state satisfies the first condition of $j > 2$. Both conditions can actually be reformulated to impose constraints on the t-anticoherence of the probe state used:

1. The quantum Fisher information strictly increases with depolarizing probability p if $|\psi_P\rangle$ is 1-AC and satisfies:
$$(\Delta_{\psi_P} J_\alpha)^2 < \frac{j(j+1)}{3}. \tag{5.1.65}$$

2. The quantum Fisher information is completely independent of the depolarizing probability p for states with anticoherence order $t \geq 2$, since such states verify:
$$(\Delta_{\psi_P} J_\alpha)^2 = \frac{j(j+1)}{3}. \tag{5.1.66}$$

Hence, we offer a direct link between the anticoherence order of the probe state used and the metrological advantage of the ancilla-assisted protocol in the presence of depolarization for the values $gt = \pi/2 + k\pi$. Moreover, both conditions imply Heisenberg scaling, which is a hallmark of quantum advantage.

5.1.4 Optimal measurement

In this section, we seek to find the optimal measurement for the first scenario of the ancilla-assisted scheme displayed in Figure 5.1 for the depolarizing channel (4.2.1) and the rotation operator $\hat{R}(\theta)$, which will encode an unknown rotation angle θ in the quantum state of the system and the Ising Hamiltonian model.

GHZ probe state

We start from the state of the total probe-ancilla system obtained at the last step of the protocol in section 5.1.1 after a rotation of angle θ for the generator $\hat{J}_z$:

$$\hat{\rho}_\theta(t) = (1-p)\,|\psi_\theta(t)\rangle\langle\psi_\theta(t)| + \frac{p}{2j+1}\sum_{m=-j}^{j} |j,m\rangle\langle j,m| \otimes |\phi_m(t)\rangle\langle\phi_m(t)|\,, \tag{5.1.67}$$

that is defined based on (5.1.4) and (5.1.28). Recall that we calculated the set of eigenvectors and eigenvalues of this state:

$$\begin{cases} |\Psi_m(\theta,t)\rangle = |j,m\rangle \otimes |\phi_m(t)\rangle \text{ with eigenvalue } \frac{p}{2j+1} \\ |\Psi_+(\theta,t)\rangle = \frac{1}{\sqrt{2}}(e^{-ij\theta}\,|j,j\rangle\,|\phi_j(t)\rangle + e^{ij\theta}\,|j,-j\rangle\,|\phi_{-j}(t)\rangle) \text{ with eigenvalue } (1-p) + \frac{p}{2j+1} \\ |\Psi_-(\theta,t)\rangle = \frac{1}{\sqrt{2}}(e^{-ij\theta}\,|j,j\rangle\,|\phi_j(t)\rangle - e^{ij\theta}\,|j,-j\rangle\,|\phi_{-j}(t)\rangle) \text{ with eigenvalue } \frac{p}{2j+1} \end{cases} \tag{5.1.68}$$

for all $m \in \{-j+1, \ldots, j-1\}$. We now need to compute the symmetric logarithmic derivative operator through the decomposition (3.4.9):

$$\hat{L}_\theta = 2i\sum_{k,l=1}^{d} \frac{\lambda_k - \lambda_l}{\lambda_k + \lambda_l}\,|\Psi_\theta^{(k)}\rangle\langle\Psi_\theta^{(l)}|\,\langle\Psi_\theta^{(k)}|\hat{J}_z|\Psi_\theta^{(l)}\rangle\,. \tag{5.1.69}$$

We deduce that eigenvectors with equal eigenvalues do not contribute to this decomposition. Moreover, owing to the orthogonality property of the standard spin basis, the only relevant inner product that has to be computed in (5.1.69) is:

$$\langle \Psi_-(\theta)|\hat{J}_z|\Psi_+(\theta)\rangle = \frac{N}{2}. \tag{5.1.70}$$

Hence, the SLD operator greatly simplifies as:

$$\hat{L}_\theta = i\,\underbrace{N\frac{(1-p)}{(1-p)+\frac{2p}{d}}}_{=A_N(p)}(|\Psi_+(\theta)\rangle\langle\Psi_-(\theta)| - |\Psi_-(\theta)\rangle\langle\Psi_+(\theta|). \tag{5.1.71}$$

The last step consists in diagonalizing this operator. Hence, one easily finds the two eigenvectors $|v_\pm\rangle$ with eigenvalues $\lambda_\pm = \pm A_N(p)$:

$$|v_\pm\rangle = \frac{1}{\sqrt{2}}\left(|j,j\rangle\,|\phi_j(t)\rangle \pm ie^{2ij\theta}\,|j,-j\rangle\,|\phi_{-j}(t)\rangle\right), \tag{5.1.72}$$

which represents GHZ type states that are maximally entangled with the ancilla qubit. Therefore, the spectral decomposition of $\hat{L}_\theta$ is:

$$\hat{L}_\theta = A_N(p)(|v_+\rangle\langle v_+| - |v_-\rangle\langle v_-|). \tag{5.1.73}$$

An optimal measurement can be performed using the projectors $\hat{\Pi}_\pm = |v_\pm\rangle\langle v_\pm|$. However, owing to the entangled nature of the eigenstates of the SLD operator, the experimental implementation of the optimal measurement is highly challenging. Consequently, it is worthwhile to consider alternative approaches, such as the Husimi sampling method discussed in Section 4.4.

Tetrahedron probe state

Let us start from the density operator of the total probe-ancilla system obtained at the last step of the protocol in section 5.1.2 after a rotation of angle θ for the generator $\hat{J}_z$:

$$\hat{\rho}_\theta(t) = (1-p)\,|\psi_\theta(t)\rangle\langle\psi_\theta(t)| + \frac{p}{2j+1}\sum_{m=-j}^{j}|j,m\rangle\langle j,m|\otimes|\phi_m(t)\rangle\langle\phi_m(t)|\,. \tag{5.1.74}$$

We can set $j=2$ to obtain the density operator for the tetrahedron probe state, where we used the shorthand notation:

$$|\psi_\theta(t)\rangle = \frac{1}{2}\left(e^{-2i\theta}\,|2,2\rangle\,|\phi_2(t)\rangle + i\sqrt{2}\,|2,0\rangle\,|\phi_0(t)\rangle + e^{2i\theta}\,|2,-2\rangle\,|\phi_{-2}(t)\rangle\right). \tag{5.1.75}$$

One computes the eigenvectors and eigenvalues of the density operator $\hat{\rho}_\theta(t)$, which yield the set:

$$\begin{cases} |2,\pm1\rangle\,|\phi_{\pm1}(t)\rangle \text{ with eigenvalue } \frac{p}{d} \\ |\psi_\theta(t)\rangle \text{ with eigenvalue } (1-p)+\frac{p}{d} \\ |\chi_\theta(t)\rangle = \frac{1}{2}\left(ie^{-2i\theta}\,|2,2\rangle\,|\phi_2(t)\rangle + \sqrt{2}\,|2,0\rangle\,|\phi_0(t)\rangle + ie^{2i\theta}\,|2,-2\rangle\,|\phi_{-2}(t)\rangle\right) \text{ with eigenvalue } \frac{p}{d} \\ |\Omega_\theta(t)\rangle = \frac{1}{\sqrt{2}}\left(e^{-2i\theta}\,|2,2\rangle\,|\phi_2(t)\rangle - e^{2i\theta}\,|2,-2\rangle\,|\phi_{-2}(t)\rangle\right) \text{ with eigenvalue } \frac{p}{d} \end{cases} \tag{5.1.76}$$

We can insert these quantities in (3.4.9) to compute the SLD operator. One can show that:

$$\begin{cases} \langle \Omega_\theta(t)|\hat{J}_z|\psi_\theta(t)\rangle = \sqrt{2} \\ \langle \chi_\theta(t)|\hat{J}_z|\psi_\theta(t)\rangle = 0 \end{cases} \tag{5.1.77}$$

Hence, the symmetric logarithmic operator can be written in the simplified form:

$$\hat{L}_\theta = iB_N(p)(|\psi_\theta\rangle\langle\Omega_\theta| - |\Omega_\theta\rangle\langle\psi_\theta|). \tag{5.1.78}$$

where we defined the multiplicative factor:

$$B_N(p) = 2\sqrt{2}\frac{(1-p)}{(1-p)+\frac{2p}{d}}. \tag{5.1.79}$$

The last step consists of diagonalizing the SLD operator. Hence, one easily finds the two eigenvectors $|u_\pm\rangle$ with eigenvalues $\lambda_\pm = \pm B_N(p)$:

$$|u_\pm\rangle = \frac{1}{\sqrt{2}}(|\psi_\theta\rangle \mp i\,|\Omega_\theta\rangle), \tag{5.1.80}$$

which can be written using the $|j,m\rangle$ states:

$$\begin{aligned} |u_\pm\rangle = \frac{1}{2}\Big(e^{-2i\theta}\left(\frac{1}{\sqrt{2}} \mp i\right)|2,2\rangle\,|\phi_2(t)\rangle \\ + i\,|2,0\rangle\,|\phi_0(t)\rangle + e^{2i\theta}\left(\frac{1}{\sqrt{2}} \pm i\right)|2,-2\rangle\,|\phi_{-2}(t)\rangle\Big). \end{aligned} \tag{5.1.81}$$

Optimal measurement can be performed using the projectors $\hat{\Pi}_\pm = |u_\pm\rangle\langle u_\pm|$. However, as in the case of the GHZ state, the experimental implementation of the optimal measurement is highly challenging due to the nature of the eigenstates of the SLD operator. Consequently, it is worthwhile to consider the Husimi sampling method discussed in Section 4.4 instead.

5.2 Unitary evolution prior to depolarization

We now consider the second scenario in Figure 5.1, i.e., the protocol in which noise mediated by the depolarizing channel occurs after unitary evolution between the probe state and the ancilla state.

5.2.1 GHZ probe state

Choosing the GHZ state as the probe state in this case yields a QFI that strictly decreases as a function of the depolarization probability p across all axes; however, the scaling law varies between the x/y-axis and the z-axis. The case of the x/y-axis is not relevant since it displays SQL scaling, which does not provide any metrological advantage compared to the case without an ancilla qubit, as shown in Figure 5.6.

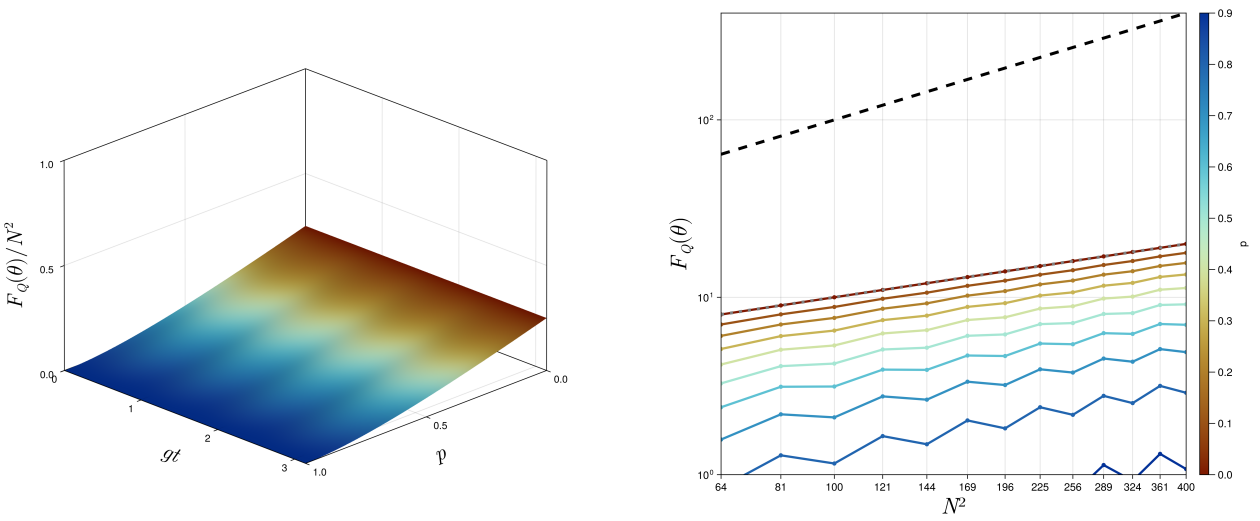

Figure 5.6: Left panel: Normalized QFI for the GHZ state ($N = 4$) as a function of the dimensionless parameter gt and the depolarizing strength p for the x/y-axis. Right panel: Log-Log plot of QFI curves for different values of the depolarizing probability p for the x/y-axis, as a function of the squared system size N^2. The Heisenberg limit is highlighted in a dashed black line, and the SQL limit in a gray dotted line.

Hence, we will focus on the z-axis case, which is displayed in Figure 5.7, as it exhibits Heisenberg scaling. We start with the GHZ probe state of a spin-j system. The total initial state of the system reads:

$$|\Psi\rangle = \left(\frac{|j,j\rangle + |j,-j\rangle}{\sqrt{2}}\right) \otimes \left(\frac{|0\rangle + |1\rangle}{\sqrt{2}}\right). \tag{5.2.1}$$

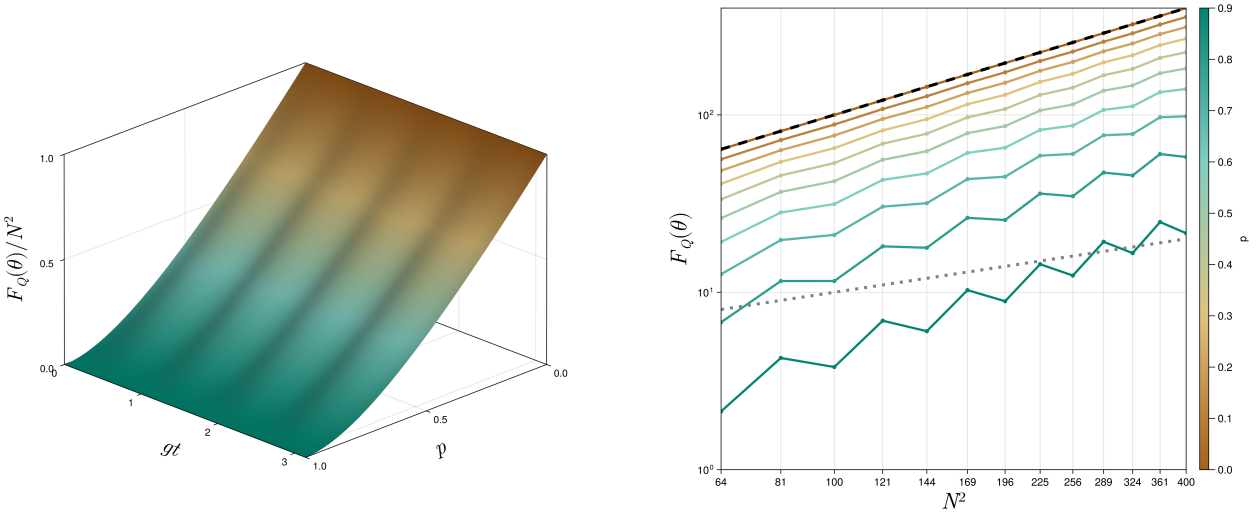

Figure 5.7: Left panel: Normalized QFI for the GHZ state ($N = 4$) as a function of the dimensionless parameter gt and the depolarizing strength p for the z-axis. Right panel: Log-Log plot of QFI curves for different values of the depolarizing probability p for the z-axis, as a function of the squared system size N^2. The Heisenberg limit is highlighted in a dashed black line, and the SQL limit in a gray dotted line.

Applying unitary evolution to this state yields:

$$|\Psi(t)\rangle = \hat{U}(t)\,|\Psi\rangle = \left(\frac{|j,-j\rangle\,|\phi_{-j}(t)\rangle + |j,j\rangle\,|\phi_j(t)\rangle}{\sqrt{2}}\right), \tag{5.2.2}$$

where we used the usual definition (5.1.4) for the $|\phi_m(t)\rangle$ states. We now apply the local depolarizing channel on the density operator of the total system $\hat{\rho}(t) = |\Psi(t)\rangle\langle\Psi(t)|$:

$$\hat{\rho}_{\text{depo}}(t) = (\mathcal{E}_{\text{depo}}(p) \otimes \hat{\mathbb{1}}_2)(\hat{\rho}(t)) = (1-p)\hat{\rho}(t) + p\left(\frac{1}{d}\hat{\mathbb{1}}_d \otimes \hat{\rho}_{\text{qubit}}\right), \tag{5.2.3}$$

where we can compute the reduced state of the qubit using the trace over the spin-j system:

$$\hat{\rho}_{\text{qubit}} = \sum_{m=-j}^{j} (\langle j,m| \otimes \hat{\mathbb{1}}_2)\hat{\rho}(t)(|j,m\rangle \otimes \hat{\mathbb{1}}_2), \tag{5.2.4}$$

which yields after simplifications:

$$\hat{\rho}_{\text{qubit}} = \frac{1}{2}(|\phi_j(t)\rangle\langle\phi_j(t)| + |\phi_{-j}(t)\rangle\langle\phi_{-j}(t)|). \tag{5.2.5}$$

Finally, we apply a rotation on the spin-j system only using the rotation operator $\hat{R}(\theta) = e^{-i\theta\hat{J}_z}$. Using the completeness relation (2.2.5) for the maximally mixed state of the spin-j system, we obtain:

$$\hat{\rho}_\theta(t) = (1-p)\,|\Psi_\theta(t)\rangle\langle\Psi_\theta(t)| + \frac{p}{2j+1}\sum_{m=-j}^{j} |j,m\rangle\langle j,m| \otimes \hat{\rho}_{\text{qubit}}, \tag{5.2.6}$$

where:

$$|\Psi_\theta(t)\rangle = \hat{R}(\theta)\,|\Psi(t)\rangle = \left(\frac{e^{i\theta j}\,|j,-j\rangle\,|\phi_{-j}(t)\rangle + e^{-i\theta j}\,|j,j\rangle\,|\phi_j(t)\rangle}{\sqrt{2}}\right). \tag{5.2.7}$$

One could attempt to diagonalize the mixed state (5.2.6) to insert its eigenvectors and eigenvalues into the eigenspace expansion form of the QFI. However, given the expression of the final density operator at the end of the protocol, this seems very time-consuming and convoluted. To keep the analysis concise, we avoid developing this aspect in detail, and we restrain ourselves to numerical simulations. It can be seen that for no depolarization, the Heisenberg limit is reached regardless of the size of the system. Depolarization effectively decreases the quantum Fisher information as p increases, which worsens the performance of the estimation of the rotation angle θ. At full depolarization, the QFI vanishes completely. Moreover, the QFI does not depend on the free energy of the probe and the ancilla. However, it depends on the dimensionless parameter gt, and the frequency is observed to be proportional to the size of the system N, although it appears extremely damped compared to the magnitude of the values observed. Finally, for sufficiently large values of the depolarization probability at a fixed size of the system, it is possible to reach the SQL limit, which signals a loss of quantum advantage. However, increasing the size of the system at a fixed depolarizing probability helps maintain this tremendous advantage for parameter estimation. Overall, we do not observe any key advantage compared to the case without an ancilla qubit.

5.2.2 Tetrahedron probe state

The tetrahedron probe state in this case yields a completely isotropic behavior of the QFI across all axes, although the ZZ interaction term in the Hamiltonian only concerns the z-axis, as shown

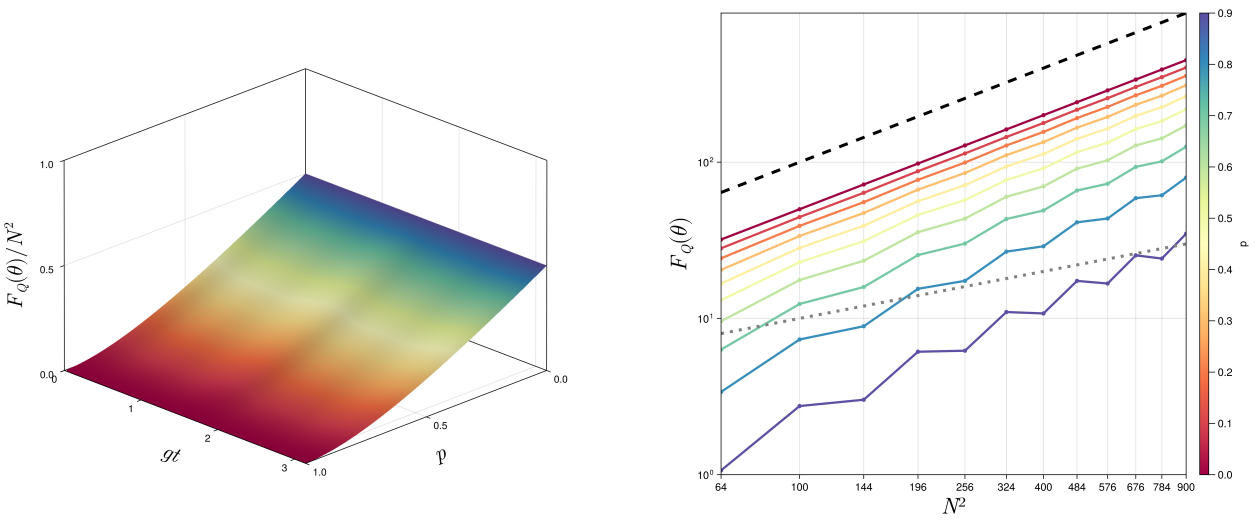

Figure 5.8: Left panel: Normalized QFI for the tetrahedron state ($N = 4$) as a function of the dimensionless parameter gt and the depolarizing strength p for the $x/y/z$-axis. Right panel: Log-Log plot of QFI curves of the family of states containing the tetrahedron state for different values of the depolarizing probability p for the $x/y/z$-axis, as a function of the squared system size N^2. The Heisenberg limit is highlighted in a dashed black line, and the SQL limit in a gray dotted line.

in Figure 5.8. Moreover, the QFI lays in the quantum advantage region, reaching an intermediate scaling with improved precision over the SQL limit, but not reaching the Heisenberg limit even for $p = 0$. The isotropic behavior is observed for anticoherent states with $t \geq 2$. Hence, it is highly probable that this feature of the system is tied to the presence of anticoherence in the probe state.

Let us compute the state at the final step of the protocol. The total initial state of the system yields:

$$|\Psi\rangle = \left(\frac{|j,j\rangle + i\sqrt{2}\,|j,0\rangle + |j,-j\rangle}{2}\right) \otimes \left(\frac{|0\rangle + |1\rangle}{\sqrt{2}}\right). \tag{5.2.8}$$

Applying unitary evolution to this state yields:

$$|\Psi(t)\rangle = \hat{U}(t)\,|\Psi\rangle = \left(\frac{|j,-j\rangle\,|\phi_{-j}(t)\rangle + i\sqrt{2}\,|j,0\rangle\,|\phi_0\rangle + |j,j\rangle\,|\phi_j(t)\rangle}{2}\right), \tag{5.2.9}$$

which depends on the $|\phi_m(t)\rangle$ states (5.1.4). We now apply the local depolarizing channel on the density operator of the total system $\hat{\rho}(t) = |\Psi(t)\rangle\langle\Psi(t)|$:

$$\hat{\rho}_{\text{depo}}(t) = (\mathcal{E}_{\text{depo}}(p) \otimes \hat{\mathbb{1}}_2)(\hat{\rho}(t)) = (1-p)\hat{\rho}(t) + p\left(\frac{1}{d}\hat{\mathbb{1}}_d \otimes \hat{\rho}_{\text{qubit}}\right). \tag{5.2.10}$$

The reduced state of the qubit can be calculated and written (after simplifications) as:

$$\hat{\rho}_{\text{qubit}} = \frac{1}{4}(|\phi_j\rangle\langle\phi_j| + 2\,|\phi_0\rangle\langle\phi_0| + |\phi_{-j}\rangle\langle\phi_{-j}|). \tag{5.2.11}$$

The last step consists of applying a rotation on the spin-j system only using the rotation operator $\hat{R}(\theta) = e^{-i\theta\hat{J}_\alpha}$. Thus, one derives:

$$\hat{\rho}_\theta(t) = (1-p)\,|\Psi_\theta(t)\rangle\langle\Psi_\theta(t)| + \frac{p}{2j+1}\sum_{m=-j}^{j} |j,m\rangle\langle j,m| \otimes \hat{\rho}_{\text{qubit}}, \tag{5.2.12}$$

where we used the shorthand notation:

$$|\Psi_\theta(t)\rangle = \hat{R}(\theta)\,|\Psi(t)\rangle = \left(\frac{e^{i\theta j}\,|j,-j\rangle\,|\phi_{-j}(t)\rangle + i\sqrt{2}\,|j,0\rangle\,|\phi_0(t)\rangle + e^{-i\theta j}\,|j,j\rangle\,|\phi_j(t)\rangle}{2}\right). \quad (5.2.13)$$

To avoid unnecessarily lengthy calculations, we stop our analysis here, as in the case of the GHZ probe state for this protocol.

5.3 Dephasing before rotation

We now move on to the second type of channel to model noise. Applying the dephasing channel before or after the unitary evolution yields the same results since both quantum operations commute.

5.3.1 GHZ probe state

The QFI for the x/y-axis is completely independent of the dephasing strength p and displays a lower asymptotic bound for the limit $N \to +\infty$. However, the QFI in this displays SQL scaling, which is not relevant as it does not reveal any quantum advantage for estimation precision compared to the case without an ancilla qubit. However, choosing the z-direction constitutes a convenient choice since for this configuration, we observe Heisenberg scaling for the quantum Fisher information, as shown in Figure 5.9.

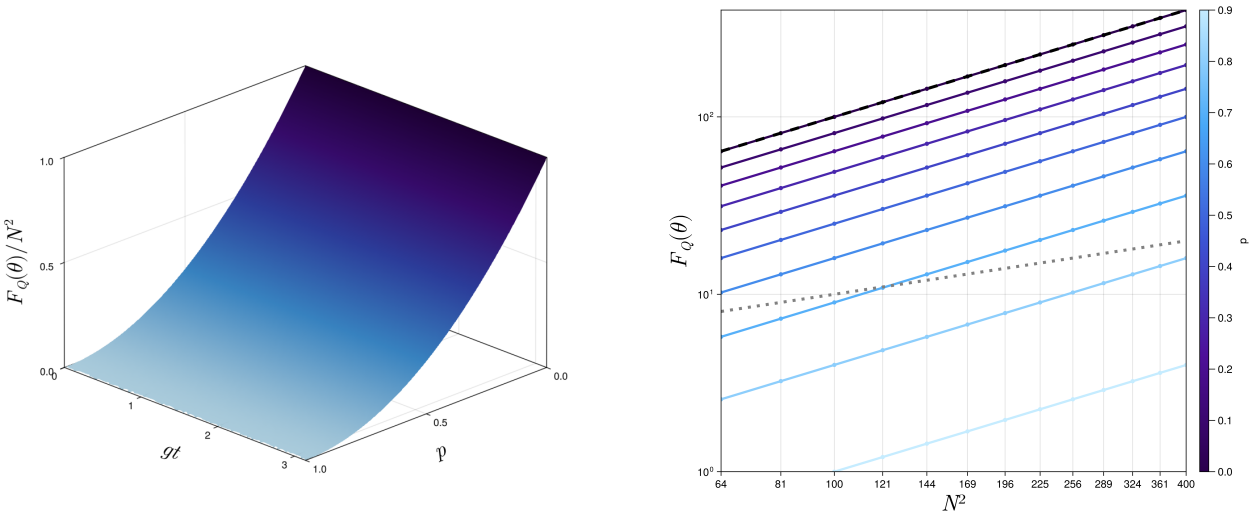

Figure 5.9: Left panel: Normalized QFI for the GHZ state ($N = 4$) as a function of the dimensionless parameter gt and the dephasing strength p for the z-axis. Right panel: Log-Log plot of QFI curves for different values of the dephasing probability p for the z-axis, as a function of the squared system size N^2. The Heisenberg limit is highlighted in a dashed black line, and the SQL limit in a gray dotted line.

Note that in this case, the QFI displays no dependence in terms of the parameter gt. Let us derive the simple expression of the QFI. We start from the initial GHZ probe state:

$$\hat{\rho}_P = |\mathrm{GHZ}\rangle\,\langle\mathrm{GHZ}|\,. \quad (5.3.1)$$

Applying the dephasing channel in the standard spin basis on this state yields:

$$\hat{\rho}_{\text{deph}}(p) = (1-p)\hat{\rho}_P + \sum_{m=-j}^{j} |\langle j,m|\text{GHZ}\rangle|^2 |j,m\rangle\langle j,m|, \tag{5.3.2}$$

which can be simplified as:

$$\hat{\rho}_{\text{deph}}(p) = \frac{1-p}{2}(|j,j\rangle\langle j,-j| + |j,-j\rangle\langle j,j|) + \frac{1}{2}(|j,j\rangle\langle j,j| + |j,-j\rangle\langle j,-j|). \tag{5.3.3}$$

Thus, the total state of the probe-ancilla system after dephasing reads:

$$\hat{\rho}_0 = \hat{\rho}_{\text{deph}}(p) \otimes |+\rangle\langle +|. \tag{5.3.4}$$

Using the usual definition for the $|\phi_m(t)\rangle$ states, we can write the density operator obtained after the unitary evolution $\hat{U}(t)\hat{\rho}_0\hat{U}^\dagger(t)$ as:

$$\begin{aligned}\hat{\rho}(t) = \frac{1-p}{2}&(|j,j\rangle\langle j,-j| \otimes |\phi_j\rangle\langle\phi_{-j}| + |j,-j\rangle\langle j,j| \otimes |\phi_{-j}\rangle\langle\phi_j|) \\ &+ \frac{1}{2}(|j,j\rangle\langle j,j| \otimes |\phi_j\rangle\langle\phi_j| + |j,-j\rangle\langle j,-j| \otimes |\phi_{-j}\rangle\langle\phi_{-j}|).\end{aligned} \tag{5.3.5}$$

Finally, applying the rotation operator $\hat{R}(\theta) = e^{-i\theta\hat{J}_z}$ yields:

$$\begin{aligned}\hat{\rho}_\theta(t) = \frac{1-p}{2}&(e^{-2i\theta j}|j,j\rangle\langle j,-j| \otimes |\phi_j\rangle\langle\phi_{-j}| + e^{2i\theta j}|j,-j\rangle\langle j,j| \otimes |\phi_{-j}\rangle\langle\phi_j|) \\ &+ \frac{1}{2}(|j,j\rangle\langle j,j| \otimes |\phi_j\rangle\langle\phi_j| + |j,-j\rangle\langle j,-j| \otimes |\phi_{-j}\rangle\langle\phi_{-j}|).\end{aligned} \tag{5.3.6}$$

This density operator admits the set of eigenvectors and eigenvalues:

$$\begin{cases} |\Psi_\theta^+\rangle = \frac{1}{\sqrt{2}}(|j,j\rangle|\phi_j\rangle + e^{2i\theta j}|j,-j\rangle|\phi_{-j}\rangle) & \text{with eigenvalue } \lambda_+ = \frac{2-p}{2} \\ |\Psi_\theta^-\rangle = \frac{1}{\sqrt{2}}(|j,j\rangle|\phi_j\rangle - e^{2i\theta j}|j,-j\rangle|\phi_{-j}\rangle) & \text{with eigenvalue } \lambda_- = \frac{p}{2} \end{cases} \tag{5.3.7}$$

Thus, the final quantum state obtained has rank 2 for $p > 0$ (and rank 1 for $p = 0$) since its support is spanned by the orthogonal ket vectors $|j,j\rangle|\phi_j\rangle, |j,-j\rangle|\phi_{-j}\rangle$ and therefore lives in a 2-dimensional subspace. All the other remaining eigenvalues are zero and are therefore irrelevant. From $\lambda_\pm$, we deduce, as in the case of the depolarizing channel, that the classical part of the total quantum Fisher information (3.5.6) vanishes. We can compute the positive contribution of the QFI (5.1.15) by calculating the following partial derivatives of the eigenvectors:

$$\partial_\theta|\Psi_\theta^\pm\rangle = \pm i\sqrt{2}je^{2i\theta}|j,-j\rangle|\phi_{-j}\rangle, \tag{5.3.8}$$

which yields the following inner products:

$$\langle\partial_\theta\Psi_\theta^\pm|\partial_\theta\Psi_\theta^\pm\rangle = 2j^2. \tag{5.3.9}$$

Hence, we deduce that the positive contribution of the total QFI part is simply:

$$F_+(\theta) = 2N^2, \tag{5.3.10}$$

which is a constant. To compute the negative contribution (5.1.16), we calculate the following cross inner products:

$$\begin{cases} \langle\Psi_\theta^\pm|\partial_\theta\Psi_\theta^\pm\rangle = ij \\ \langle\Psi_\theta^\pm|\partial_\theta\Psi_\theta^\mp\rangle = -ij \end{cases} \tag{5.3.11}$$

which yields the same j^2 value after taking the modulus squared. Hence, the negative contribution of the QFI can be written as:

$$F_-(\theta) = -N^2(1 + 2p - p^2), \tag{5.3.12}$$

and is responsible for the decay seen in Figure 5.9 as p increases. Hence, the total QFI reads:

$$F_Q(\theta) = N^2(1 - p)^2 \tag{5.3.13}$$

which does not depend on the parameter gt and displays Heisenberg scaling as expected, as in the case of no ancilla qubit.

5.3.2 Tetrahedron probe state

For the family of states (5.1.32), the QFI reaches the quantum advantage region across all axes, similarly to the case without an ancilla qubit. As for the case of the GHZ probe state, the QFI does not depend on the dimensionless parameter gt. Moreover, the quantum Fisher information is completely independent of the dephasing probability p for the x and y axes, and displays an asymptotic lower bound in the limit $N \to +\infty$, as shown in Figure 5.10.

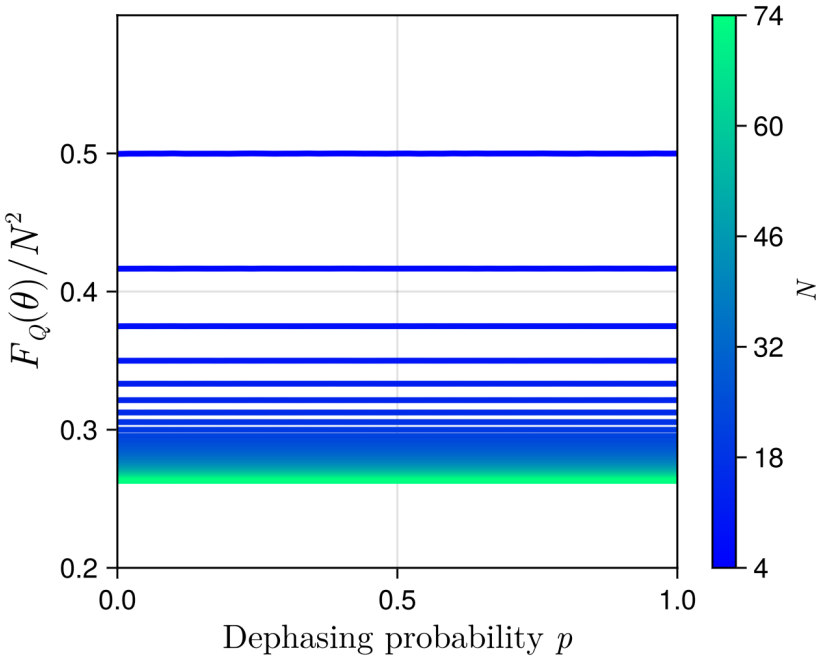

Figure 5.10: Normalized quantum Fisher information as a function of the dephasing probability p for the family of states (5.1.32) (x/y-axis) for successive values of even N between 4 and 74.

In order to derive the full expression of the QFI, we can proceed using the same method as in the case of the GHZ state in section 5.1.1, where depolarization occurs before unitary evolution. Hence, one needs to compute and manipulate elements of the Wigner small-d matrix. In order to keep this manuscript compact, we will just give the final expression:

$$F_Q(\theta) = \frac{N(N+4)}{4}. \tag{5.3.14}$$

Hence, normalizing this expression by N^2 yields, in the thermodynamic limit:

$$\lim_{N\to+\infty} \frac{F_Q(\theta)}{N^2} = \frac{1}{4}, \tag{5.3.15}$$

which is the lower bound observed in Figure 5.10. Let us derive the QFI explicitly for the z-axis, displayed in Figure 5.11, which offers a simpler analytical derivation.

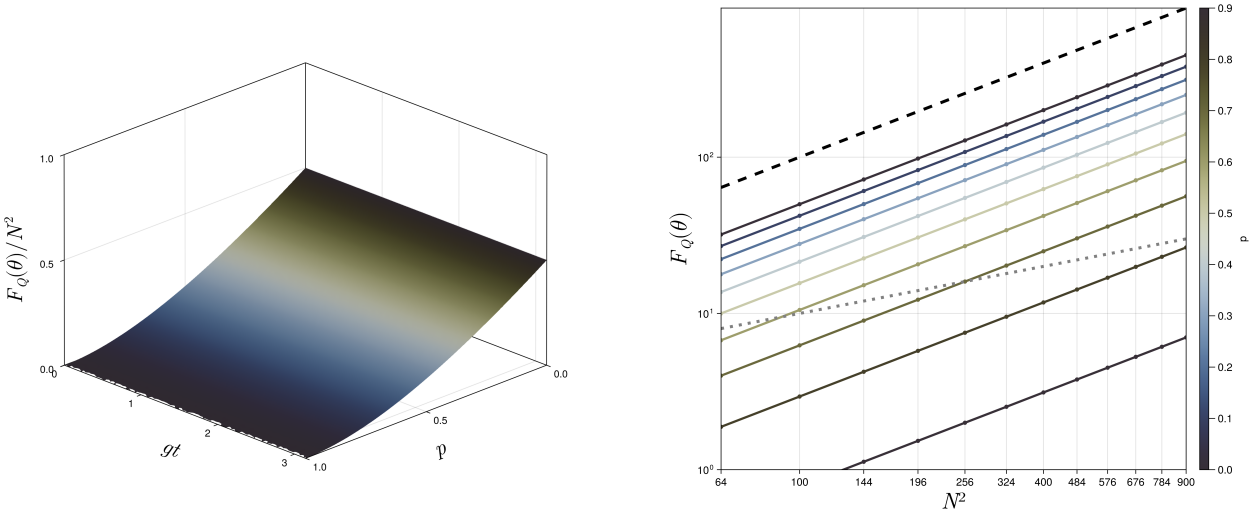

Figure 5.11: Left panel: Normalized QFI for the tetrahedron state ($N = 4$) as a function of the dimensionless parameter gt and the dephasing strength p for the z-axis. Right panel: Log-Log plot of QFI curves for different values of the depolarization probability p for the z-axis, as a function of the squared system size N^2 for the family of states (5.1.32). The Heisenberg limit is highlighted in a dashed black line, and the SQL limit in a gray dotted line.

Let us begin with the family of states (5.1.32):

$$|\psi\rangle = \frac{1}{2}(|j,j\rangle + i\sqrt{2}\,|j,0\rangle + |j,-j\rangle). \tag{5.3.16}$$

Applying the dephasing channel to the density operator of this state yields:

$$\hat{\rho}_{\text{deph}}(p) = (1-p)\,|\psi\rangle\langle\psi| + p\sum_{m=-j}^{j} |\langle j,m|\psi\rangle|^2\,|j,m\rangle\langle j,m|\,, \tag{5.3.17}$$

which we can write as:

$$\hat{\rho}_{\text{deph}}(p) = (1-p)\,|\psi\rangle\langle\psi| + \frac{p}{4}(|j,j\rangle\langle j,j| + 2\,|j,0\rangle\langle j,0| + |j,-j\rangle\langle j,-j|). \tag{5.3.18}$$

Unitary evolution of this dephased state for the Ising Hamiltonian (5.0.4) yields:

$$\begin{aligned}\hat{\rho}(t) = (1-p)\,|\psi(t)\rangle\langle\psi(t)| + \frac{p}{4}(|j,j\rangle\langle j,j| \otimes |\phi_j\rangle\langle\phi_j| \\ + 2\,|j,0\rangle\langle j,0| \otimes |\phi_0\rangle\langle\phi_0| + |j,-j\rangle\langle j,-j| \otimes |\phi_{-j}\rangle\langle\phi_{-j}|),\end{aligned} \tag{5.3.19}$$

which involves the states (5.1.4). In this expression, we have used the notation:

$$|\psi(t)\rangle = \frac{1}{2}(|j,j\rangle\,|\phi_j(t)\rangle + i\sqrt{2}\,|j,0\rangle\,|\phi_0(t)\rangle + |j,-j\rangle\,|\phi_{-j}(t)\rangle). \tag{5.3.20}$$

Applying the rotation $\hat{R}(\theta)$ using the z-axis projection $\hat{J}_z$ angular momentum operator as the generator of the rotation on the density operator yields:

$$\begin{aligned}\hat{\rho}_\theta(t) = (1-p)\,|\psi_\theta(t)\rangle\langle\psi_\theta(t)| + \frac{p}{4}(|j,j\rangle\langle j,j| \otimes |\phi_j\rangle\langle\phi_j| \\ + 2\,|j,0\rangle\langle j,0| \otimes |\phi_0\rangle\langle\phi_0| + |j,-j\rangle\langle j,-j| \otimes |\phi_{-j}\rangle\langle\phi_{-j}|),\end{aligned} \tag{5.3.21}$$

where we used the quantity:

$$|\psi_\theta(t)\rangle = \frac{1}{2}(e^{-2i\theta j}\,|j,j\rangle\,|\phi_j(t)\rangle + i\sqrt{2}\,|j,0\rangle\,|\phi_0(t)\rangle + e^{2i\theta j}\,|j,-j\rangle\,|\phi_{-j}(t)\rangle). \tag{5.3.22}$$

The diagonalization procedure of the density operator (5.3.21) yields the set of eigenvectors and eigenvalues:

$$\begin{cases} |\Psi_\theta\rangle = \frac{1}{\sqrt{2}}(e^{-i\theta j}\,|j,j\rangle\,|\phi_j\rangle - e^{i\theta j}\,|j,-j\rangle\,|\phi_{-j}\rangle) & \text{with eigenvalue } \lambda = \frac{p}{4} \\ |\Psi_\theta^+\rangle = N_+(e^{-i\theta j}\,|j,j\rangle\,|\phi_j\rangle + k_+\,|j,0\rangle\,|\phi_0\rangle + e^{i\theta j}\,|j,-j\rangle\,|\phi_{-j}\rangle) & \text{with eigenvalue } \lambda_+ = \frac{4-p+\Delta}{8} \\ |\Psi_\theta^-\rangle = N_-(e^{-i\theta j}\,|j,j\rangle\,|\phi_j\rangle + k_-\,|j,0\rangle\,|\phi_0\rangle + e^{i\theta j}\,|j,-j\rangle\,|\phi_{-j}\rangle) & \text{with eigenvalue } \lambda_- = \frac{4-p-\Delta}{8} \end{cases} \tag{5.3.23}$$

where we defined the quantities:

$$N_\pm = \frac{1}{\sqrt{1+|k_\pm|^2}} \qquad k_\pm = i\frac{p \pm \sqrt{p^2+16(1-p)^2}}{2\sqrt{2}(1-p)} \qquad \Delta = \sqrt{17p^2-32p+16} \tag{5.3.24}$$

The derivatives of these eigenvectors can be computed in a straightforward manner, to obtain:

$$\begin{cases} \partial_\theta\,|\Psi_\theta\rangle = \frac{-ij}{\sqrt{2}}(e^{-i\theta j}\,|j,j\rangle\,|\phi_j\rangle + e^{i\theta j}\,|j,-j\rangle\,|\phi_{-j}\rangle) \\ \partial_\theta\,|\Psi_\theta^\pm\rangle = -ijN_\pm(e^{-i\theta j}\,|j,j\rangle\,|\phi_j\rangle - e^{i\theta j}\,|j,-j\rangle\,|\phi_{-j}\rangle) \end{cases} \tag{5.3.25}$$

Thus, to compute the positive contribution (5.1.15) of the QFI, we need to insert the following inner products:

$$\langle\partial_\theta\Psi_\theta|\partial_\theta\Psi_\theta\rangle = j^2, \qquad \langle\partial_\theta\Psi_\theta^\pm|\partial_\theta\Psi_\theta^\pm\rangle = \frac{8j^2(1-p)^2}{\Delta(\Delta\pm p)}, \tag{5.3.26}$$

which gives the final expression:

$$F_+(\theta) = 2j^2. \tag{5.3.27}$$

The negative contribution (5.1.16) only requires the inner products:

$$\langle\Psi_\theta|\partial_\theta\Psi_\theta^\pm\rangle = \langle\Psi_\theta^\pm|\partial_\theta\Psi_\theta\rangle = -ij\sqrt{2}N_\pm, \tag{5.3.28}$$

since other combinations vanish. Hence, we obtain:

$$F_-(\theta) = -2j^2p\frac{8-5p}{5-2p}. \tag{5.3.29}$$

Consequently, the total quantum Fisher information reads:

$$F_Q(\theta) = \frac{5}{2}N^2\frac{(1-p)^2}{5-2p}, \tag{5.3.30}$$

which displays Heisenberg scaling. The total QFI depends only on the dephasing probability and the size of the system N, which coincides with numerical observations, as seen in Figure 5.11.

5.4 Dephasing after rotation (x/y-axis)

Surprisingly enough, both the tetrahedron and GHZ probe states share the exact same QFI behavior in Scenario 2 and 3 in Figure 5.1 where dephasing occurs before or after the rotation transformation around the x/y axis. This result is surprising at first glance since the dephasing channel does not commute with the rotation operator for this choice of reference axis. Consequently, the state obtained after the two successive operations will be genuinely different. However, this does not imply that their quantum Fisher information will be distinct. In fact, it is trivial that given two generic density operators $\hat{\rho}_1, \hat{\rho}_2$, we have:

$$\hat{\rho}_1(\theta) = \hat{\rho}_2(\theta) \quad \Rightarrow \quad F_Q(\theta, \hat{\rho}_1(\theta)) = F_Q(\theta, \hat{\rho}_2(\theta)), \tag{5.4.1}$$

for a given parameter encoding transformation, owing to the spectral decomposition. However,

$$\hat{\rho}_1(\theta) \neq \hat{\rho}_2(\theta) \quad \not\Rightarrow \quad F_Q(\theta, \hat{\rho}_1(\theta)) \neq F_Q(\theta, \hat{\rho}_2(\theta)). \tag{5.4.2}$$

In our case, both the tetrahedron and the GHZ states are embedded in the family of pure states:

$$|\Psi\rangle = a\,|j, j\rangle + b\,|j, 0\rangle + c\,|j, -j\rangle\,, \tag{5.4.3}$$

where a, b, c are complex scalars that fulfill the normalization condition $|a|^2 + |b|^2 + |c|^2 = 1$. For a specific choice of these coefficients, the density operators obtained for both operator orderings can be computed according to:

$$\hat{\rho}_1(\theta) = \hat{R}(\theta)\mathcal{E}_{\text{deph}}(|\Psi\rangle\langle\Psi|, p)\hat{R}^\dagger(\theta), \tag{5.4.4}$$

$$\hat{\rho}_2(\theta) = \mathcal{E}_{\text{deph}}(\hat{R}(\theta)\,|\Psi\rangle\langle\Psi|\,\hat{R}^\dagger(\theta), p), \tag{5.4.5}$$

could be distinct, but with an equal QFI. However, finding conditions on a, b, c from $F_Q(\theta, \hat{\rho}_1(\theta)) = F_Q(\theta, \hat{\rho}_2(\theta))$ is not a trivial problem, at least if one assumes that at least two of these coefficients are non-zero, since we seek non-trivial states. Two conditions that seem to satisfy these requirements based on numerical simulations for $j = 2$ are:

$$|a| = |c|, \qquad ab^* + bc^* = 0. \tag{5.4.6}$$

One can verify that both of these conditions are met for the tetrahedron state and the GHZ state for this value of the spin. Obviously, the class of ket vectors obtained based on (5.4.6) only represents a specific subgroup contained in the subset of quantum states that verify $F_Q(\theta, \hat{\rho}_1(\theta)) = F_Q(\theta, \hat{\rho}_2(\theta))$, despite having different density operators for both of the transformations (5.4.4) and (5.4.5). However, finding this exact set is an arduous task.

Furthermore, note that the family of states found based on the conditions (5.4.6) is linked to anticoherence. Indeed, computing the mean value of the projections of the total angular momentum operator in this state yields :

$$\langle \hat{J}_x \rangle = \langle \hat{J}_y \rangle = 0, \qquad \langle \hat{J}_z \rangle = j(|a|^2 - |c|^2). \tag{5.4.7}$$

Hence, the family of ket vectors (5.4.3), together with the set of conditions (5.4.6) on the coefficients a, b, c, represents 1-AC states. However, there exist some states that are 1-AC and do not fulfill the condition for $F_Q(\theta, \hat{\rho}_1(\theta)) = F_Q(\theta, \hat{\rho}_2(\theta))$, since the second condition $ab^* + bc^* = 0$ can be violated.

5.5 Summary tables of observations

This section contains the relevant results for all the possible configurations for the ancilla-assisted protocols displayed in Figure 5.1. Indeed, we consider two types of transformations for parameter encoding: a rotation transformation with an angle θ and spin squeezing with a squeezing strength χ. Entanglement is realized through unitary evolution with the Ising Hamiltonian model and the isotropic model. The noise mechanisms that we consider are depolarization and dephasing. The Hamiltonian models used for the entanglement gate are the ZZ Hamiltonian and the isotropic Hamiltonian. Note that in the case of the ZZ Hamiltonian, the free energies of the probe and the ancilla do not reveal any significant improvement in precision enhancement. Finally, for each protocol, we consider the GHZ state, as well as the family of states containing the 2-AC tetrahedron state.

Parameter encoding operator : $\hat{R}(\theta, \mathbf{n}) = \exp\left(-i\theta(\hat{\mathbf{J}} \cdot \mathbf{n})\right)$			
Hamiltonian model : $\hat{H} = \omega_P(\hat{J}_z \otimes \hat{\mathbb{1}}) + \omega_{\text{anc}}(\hat{\mathbb{1}}_d \otimes \hat{\sigma}_z) + g(\hat{J}_z \otimes \hat{\sigma}_z)$			
Protocol configuration	Quantum channel	Quantum-advantaged axes	QFI-nondecreasing axes
Scenario 1	Depolarization	x, y, z	x, y
	Dephasing	z only	x, y
Scenario 2	Depolarization	z only	None
	Dephasing	z only	x, y
Scenario 3	Depolarization	z only	None
	Dephasing	z only	x, y

Table 5.1: Summary table of the observations for every scenario of Figure 5.1 for the GHZ probe state, for rotation sensing and the Ising Hamiltonian model.

Parameter encoding operator : $\hat{S}(\chi, \mathbf{n}) = \exp\left(-i\chi(\hat{\mathbf{J}} \cdot \mathbf{n})^2\right)$			
Hamiltonian model : $\hat{H} = \omega_P(\hat{J}_z \otimes \hat{\mathbb{1}}) + \omega_{\text{anc}}(\hat{\mathbb{1}}_d \otimes \hat{\sigma}_z) + g(\hat{J}_z \otimes \hat{\sigma}_z)$			
Protocol configuration	Quantum channel	Quantum-advantaged axes	QFI-nondecreasing axes
Scenario 1	Depolarization	None	None
	Dephasing	None	x, y
Scenario 2	Depolarization	None	None
	Dephasing	None	x/y
Scenario 3	Depolarization	None	None
	Dephasing	None	x, y

Table 5.2: Summary table of the observations for every scenario of Figure 5.1 for the GHZ probe state, for spin squeezing and the Ising Hamiltonian model.

Parameter encoding operator : $\hat{R}(\theta, \mathbf{n}) = \exp\left(-i\theta(\hat{\mathbf{J}} \cdot \mathbf{n})\right)$			
Hamiltonian model : $\hat{H}_{\text{iso}} = h(\hat{J}_x \otimes \hat{\sigma}_x + \hat{J}_y \otimes \hat{\sigma}_y + \hat{J}_z \otimes \hat{\sigma}_z)$			
Protocol configuration	Quantum channel	Quantum-advantaged axes	QFI-nondecreasing axes
Scenario 1	Depolarization	z	None
	Dephasing	z	x, y
Scenario 2	Depolarization	z	None
	Dephasing	None	x, y
Scenario 3	Depolarization	z	None
	Dephasing	z	x, y

Table 5.3: Summary table of the observations for every scenario of Figure 5.1 for the GHZ probe state, for rotation sensing and the isotropic Hamiltonian model.

Parameter encoding operator : $\hat{S}(\chi, \mathbf{n}) = \exp\left(-i\chi(\hat{\mathbf{J}} \cdot \mathbf{n})^2\right)$			
Hamiltonian model : $\hat{H}_{\text{iso}} = h(\hat{J}_x \otimes \hat{\sigma}_x + \hat{J}_y \otimes \hat{\sigma}_y + \hat{J}_z \otimes \hat{\sigma}_z)$			
Protocol configuration	Quantum channel	Quantum-advantaged axes	QFI-nondecreasing axes
Scenario 1	Depolarization	None	z
	Dephasing	None	x, y, z
Scenario 2	Depolarization	None	None
	Dephasing	None	x, y
Scenario 3	Depolarization	None	None
	Dephasing	None	None

Table 5.4: Summary table of the observations for every scenario of Figure 5.1 for the GHZ probe state, for spin squeezing and the isotropic Hamiltonian model.

Parameter encoding operator : $\hat{R}(\theta, \mathbf{n}) = \exp\left(-i\theta(\hat{\mathbf{J}} \cdot \mathbf{n})\right)$			
Hamiltonian model : $\hat{H} = \omega_P(\hat{J}_z \otimes \hat{\mathbb{1}}) + \omega_{\text{anc}}(\hat{\mathbb{1}}_d \otimes \hat{\sigma}_z) + g(\hat{J}_z \otimes \hat{\sigma}_z)$			
Protocol configuration	Quantum channel	Quantum-advantaged axes	QFI-nondecreasing axes
Scenario 1	Depolarization	x, y, z	x, y
	Dephasing	x, y, z	x, y
Scenario 2	Depolarization	x, y, z	None
	Dephasing	x, y, z	x, y
Scenario 3	Depolarization	x, y, z	None
	Dephasing	x, y, z	x, y

Table 5.5: Summary table of the observations for every scenario of Figure 5.1 for the family of states containing the tetrahedron state, for rotation sensing and the Ising Hamiltonian model.

Parameter encoding operator : $\hat{S}(\chi, \mathbf{n}) = \exp\left(-i\chi(\hat{\mathbf{J}} \cdot \mathbf{n})^2\right)$			
Hamiltonian model : $\hat{H} = \omega_P(\hat{J}_z \otimes \hat{\mathbb{1}}) + \omega_{\text{anc}}(\hat{\mathbb{1}}_d \otimes \hat{\sigma}_z) + g(\hat{J}_z \otimes \hat{\sigma}_z)$			
Protocol configuration	Quantum channel	Quantum-advantaged axes	QFI-nondecreasing axes
Scenario 1	Depolarization	x, y, z	x, y
	Dephasing	x, y, z	x, y
Scenario 2	Depolarization	x, y, z	None
	Dephasing	x, y, z	x, y
Scenario 3	Depolarization	x, y, z	None
	Dephasing	x, y, z	x, y

Table 5.6: Summary table of the observations for every scenario of Figure 5.1 for the family of states containing the tetrahedron state, for spin squeezing and the Ising Hamiltonian model.

Parameter encoding operator : $\hat{R}(\theta, \mathbf{n}) = \exp\left(-i\theta(\hat{\mathbf{J}} \cdot \mathbf{n})\right)$			
Hamiltonian model : $\hat{H}_{\text{iso}} = h(\hat{J}_x \otimes \hat{\sigma}_x + \hat{J}_y \otimes \hat{\sigma}_y + \hat{J}_z \otimes \hat{\sigma}_z)$			
Protocol configuration	Quantum channel	Quantum-advantaged axes	QFI-nondecreasing axes
Scenario 1	Depolarization	x, y, z	None
	Dephasing	x, y, z	x, y
Scenario 2	Depolarization	x, y, z	None
	Dephasing	None	x, y
Scenario 3	Depolarization	x, y, z	None
	Dephasing	x, y, z	x, y

Table 5.7: Summary table of the observations for every scenario of Figure 5.1 for the family of states containing the tetrahedron state, for rotation sensing and the isotropic Hamiltonian model.

Parameter encoding operator : $\hat{S}(\chi, \mathbf{n}) = \exp\left(-i\chi(\hat{\mathbf{J}} \cdot \mathbf{n})^2\right)$			
Hamiltonian model : $\hat{H}_{\text{iso}} = h(\hat{J}_x \otimes \hat{\sigma}_x + \hat{J}_y \otimes \hat{\sigma}_y + \hat{J}_z \otimes \hat{\sigma}_z)$			
Protocol configuration	Quantum channel	Quantum-advantaged axes	QFI-nondecreasing axes
Scenario 1	Depolarization	x, y, z	None
	Dephasing	x, y, z	x, y, z
Scenario 2	Depolarization	x, y, z	None
	Dephasing	None	x, y
Scenario 3	Depolarization	x, y, z	None
	Dephasing	x, y, z	x, y

Table 5.8: Summary table of the observations for every scenario of Figure 5.1 for the family of states containing the tetrahedron state, for spin squeezing and the isotropic Hamiltonian model.

5.6 Numerical construction of estimators

In this section, we aim to numerically construct an estimator of an unknown rotation angle that is encoded in a parameter family of states $\hat{\rho}(\theta)$ in a rotation sensing setup for a defined axis $\mathbf{n}$. To this end, we numerically implement the optimal measurement by taking advantage of the simulation speed provided by computers.

5.6.1 Optimal measurement

Let us numerically construct an estimator based on the optimal measurement approach introduced in section 4.3. We first choose an arbitrary probe state and specify a quantum protocol (noise-free or noisy) that will allow us to encode an unknown parameter θ that we wish to estimate. Using the density operator obtained at the final step of the protocol, we can compute its corresponding eigenvectors and eigenvalues in order to calculate the symmetric logarithmic derivative. We then use the optimal measurement framework by diagonalizing the SLD to find the projectors $\hat{\Pi}_k$ composed of its eigenstates. The key idea is to simulate a quantum measurement, giving a random measurement outcome k, where k indexes the eigenbasis of the SLD. According to Born's rule, each measurement outcome is associated with a certain realization probability p_k that we can compute explicitly using projectors $\hat{\Pi}_k$ and the final quantum state. We repeat this process (from state preparation to measurement), which we refer to as a "shot", a large number of times n_s shots, in order to construct a count vector consisting of the number of counts n_k associated with the number of times the outcome k has been drawn. Using these quantities, we can numerically implement the maximum likelihood estimation method by computing the log likelihood function $l(\theta)$ and maximizing it. This yields an ML estimator $\tilde{\theta}_{\mathrm{ML}}$. This entire process constitutes one trial. Carrying out N_t trials will therefore yield N_t ML estimators, from which we can compute the empirical average and compare it to the true value of the parameter originally encoded. This method is summarized in Figure 5.12

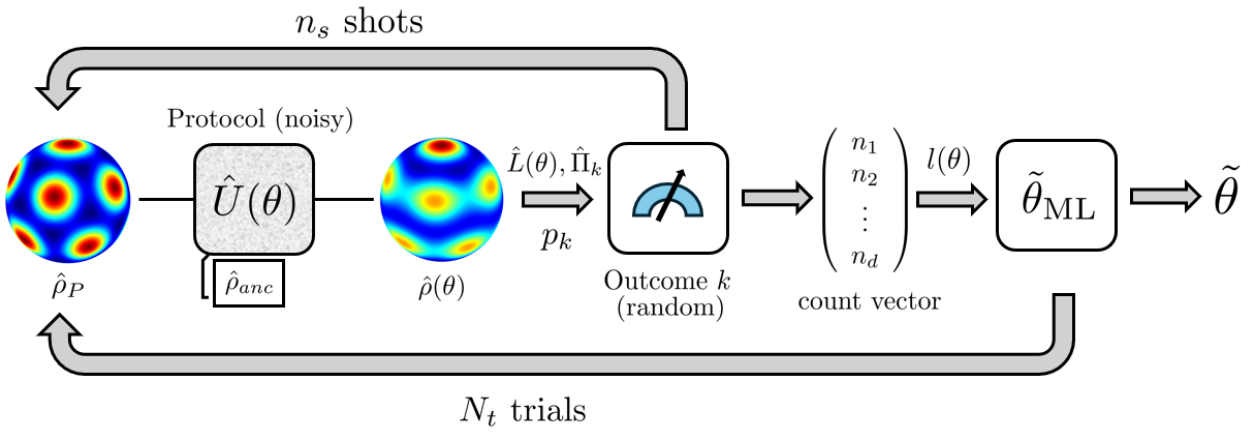

Figure 5.12: Visual representation of the process used to numerically compute an estimator in rotation sensing. A probe state is used in a noisy (ancilla-assisted) quantum protocol to encode the physical parameter θ. A count vector is derived from n_s shots using the optimal measurement process in order to construct an estimator based on the maximum likelihood method. N_t trials of this process are conducted to obtain the empirical mean of the set of estimators obtained.

We can explicitly implement this method for the first ancilla-assisted protocol in section 5.1.1 by choosing the GHZ state ($N = 4$) as the probe state, which will be depolarized with probability p,

and then entangled with an ancilla qubit state using the Ising Hamiltonian model. The parameter is encoded through a rotation of a small angle θ using the generator $\hat{J}_z$. In this scenario, we can compute the mean estimator $\tilde{\theta}$ and study the influence of the depolarizing strength on the precision of estimation, since increasing the depolarizing strength p degrades the total amount of information that we can extract from the system. Figure 5.13 displays the distribution of estimators for this case.

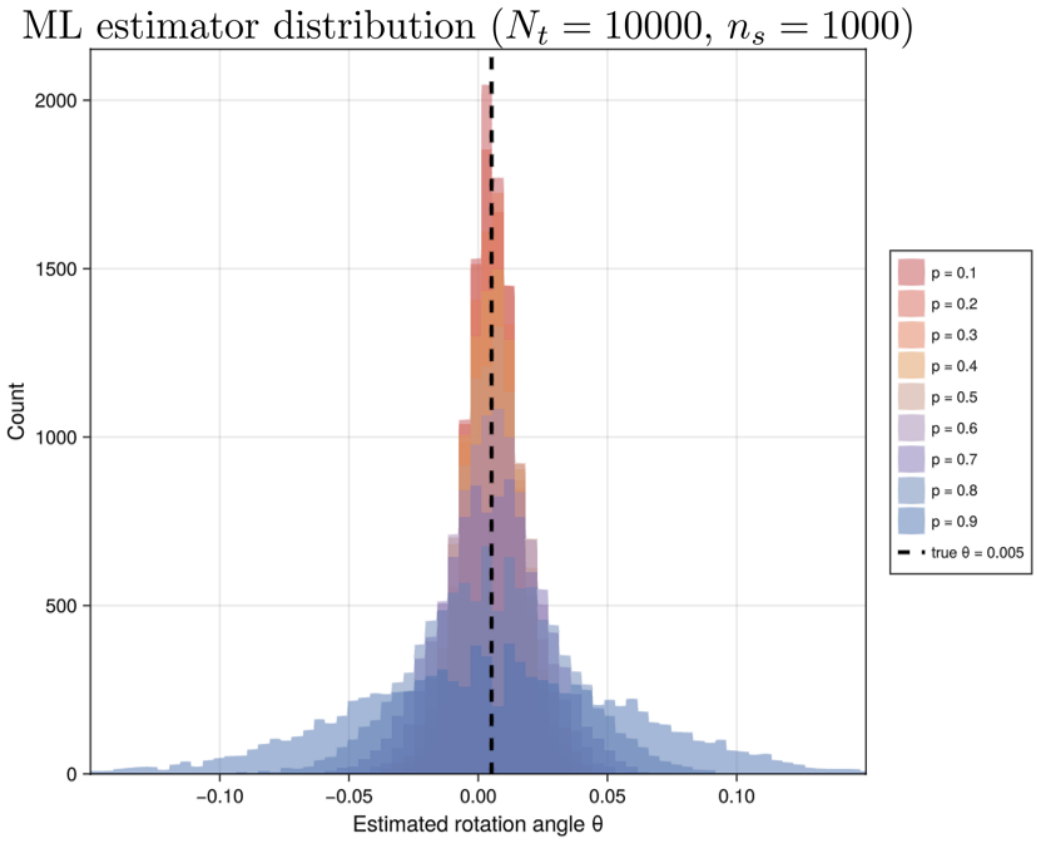

Figure 5.13: Estimator distribution based on optimal measurement and the maximum likelihood estimator construction method for 10 000 trials, and several values of depolarization probability, ranging from 0.1 to 0.9. Each trial computes an estimator of the unknown rotation angle with a true value $\theta = 0.005$ which is highlighted by a dashed line in black. Hence, the sum of the counts correspond exactly to the number of trials, and each trial consists of 1000 random draws. This specific histogram is based on the first protocol introduced in section 5.1.1, for a rotation of angle θ around the z-axis and the depolarized GHZ probe state for $N = 4$.

From Figure 5.13, we can conclude that depolarization has a negative effect on the performance of the estimation for the unknown parameter θ. Indeed, as the depolarizing strength p increases, the ML estimator distribution covers a broader range of values centered around the true value $\theta = 0.005$. This coincides with the results found in section 5.1.1, since the quantum Fisher information is strictly decreasing as a function of p when choosing the reference axis $\mathbf{n} = \mathbf{e}_z$. This observation is supported by Figure 5.14 since the empirical variance associated with the empirical mean of the ML estimators increases drastically as p approaches 1 for full depolarization. Moreover, the empirical mean of $\tilde{\theta}$ takes values that become increasingly distant from the true value of $\tilde{\theta}$, especially near full depolarization.

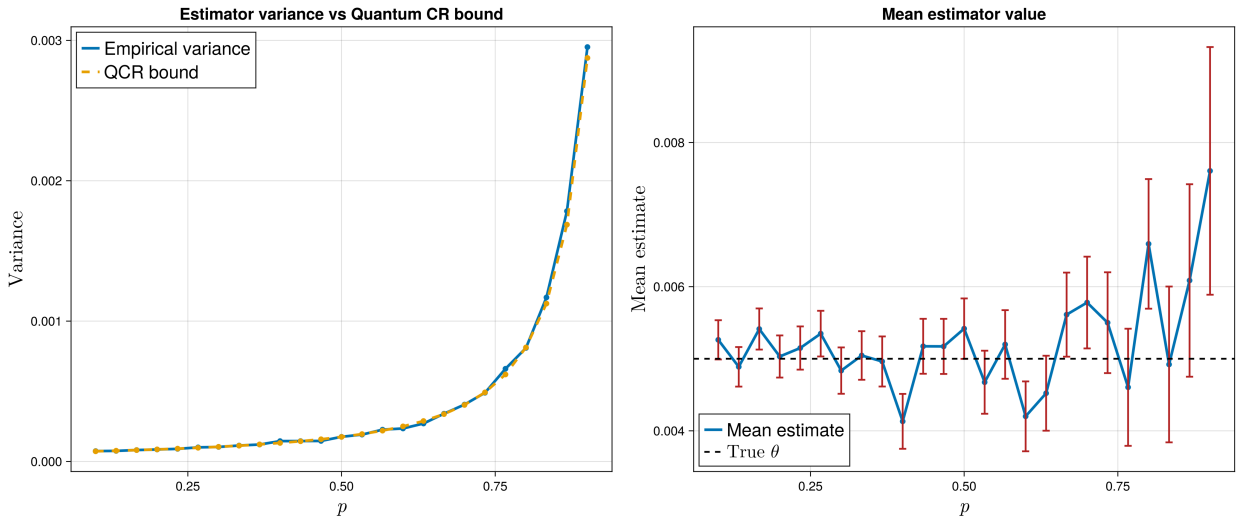

Figure 5.14: Left panel: Empirical variance of the estimator $\tilde{\theta}$ obtained at the end of 1000 trials for 1000 shots each, for various values of the depolarizing strength p between 0 and 1. The achievable precision is highlighted in gold by the QCR bound. Right panel: The empirical mean of the estimator $\tilde{\theta}$ obtained at the end of 1000 trials for 1000 shots each, for various values of the depolarizing strength p between 0 and 1. The empirical variance is underscored by red error bars, and the true value of the rotation angle is highlighted by a black dashed line in black. Both of these plots are based on the first protocol presented in section 5.1.1, for the GHZ state ($N = 4$) for rotation sensing with the convenient choice $\mathbf{n} = \mathbf{e}_z$.

Chapter 6

Beyond single-parameter estimation

A central problem in modern research concerns the natural extension of the single-parameter estimation theory that we employed in this master's thesis. Indeed, the general framework beyond the single parameter estimation is the *multiparameter estimation theory*, whose goal is to estimate $M > 1$ parameters $\theta_1, \ldots, \theta_M$ that represent physical quantities (for example, the cartesian components of the magnetic field), often expressed using the vector [61]:

$$\boldsymbol{\theta} = (\theta_1, \ldots, \theta_M)^T. \tag{6.0.1}$$

These parameters are encoded into a quantum state such that we define the parameter family:

$$\{\hat{\rho}(\boldsymbol{\theta}) : \boldsymbol{\theta} \in \boldsymbol{\Theta} \subseteq \mathbb{R}^M\}, \tag{6.0.2}$$

where $\boldsymbol{\Theta}$ is the parameter space. Naturally, we can infer that this set of unknown quantities can be evaluated by constructing a set of estimators, grouped into the vector:

$$\tilde{\boldsymbol{\theta}} = (\tilde{\theta}_1, \ldots, \tilde{\theta}_M)^T, \tag{6.0.3}$$

after a measurement set $\mathbf{x} = (x_1, \ldots, x_M)$. In multiparameter estimation theory, the classical Fisher information no longer represents a scalar. In fact, for a measurement outcome x distributed according to $p(x|\boldsymbol{\theta})$, the Fisher information is described by a symmetric and positive matrix, whose elements read [77]:

$$(\mathbf{F}_{\mathbf{x}}(\boldsymbol{\theta}))_{ij} = \int d\mathbf{x} \frac{\partial \ln(p(x|\boldsymbol{\theta})}{\partial \theta_i} \frac{\partial \ln(p(x|\boldsymbol{\theta})}{\partial \theta_j}. \tag{6.0.4}$$

In the same spirit, we define the *quantum Fisher information matrix (QFIM)*, whose elements are defined by [77]:

$$(\mathbf{F}_Q(\hat{\rho}_{\boldsymbol{\theta}}, \boldsymbol{\theta}))_{ij} = \frac{1}{2}\mathrm{Tr}\left(\hat{\rho}_\theta(\hat{L}_i\hat{L}_j + \hat{L}_j\hat{L}_i)\right), \tag{6.0.5}$$

where $\hat{L}_i$ represents the symmetric logarithmic derivative for the parameter θ_i, and it is defined according to the differential equation [61]:

$$\frac{\partial}{\partial \theta_i}\hat{\rho}(\boldsymbol{\theta}) = \frac{1}{2}\{\hat{\rho}_{\boldsymbol{\theta}}, \hat{L}_i\}, \tag{6.0.6}$$

for the parameter family of quantum states $\hat{\rho}(\boldsymbol{\theta})$. The diagonal terms of the QFIM matrix quantify how sensitive the quantum state $\hat{\rho}(\theta)$ is to the parameter θ_i, whereas the off-diagonal terms represent statistical couplings between distinct parameters θ_i and θ_j. In other words, they indicate the

potential presence of correlations. For the case of pure states $\hat{\rho}_{\boldsymbol{\theta}} = |\psi_{\boldsymbol{\theta}}\rangle \langle\psi_{\boldsymbol{\theta}}|$, the QFIM elements reduce to the expression [60]:

$$(\mathbf{F}_Q(\hat{\rho}_{\boldsymbol{\theta}}, \boldsymbol{\theta}))_{ij} = 4\mathrm{Re}(\langle\partial_{\theta_i}\psi_{\boldsymbol{\theta}}|\partial_{\theta_j}\psi_{\boldsymbol{\theta}}\rangle) + 4\langle\partial_{\theta_i}\psi_{\boldsymbol{\theta}}|\psi_{\boldsymbol{\theta}}\rangle\langle\partial_{\theta_j}\psi_{\boldsymbol{\theta}}|\psi_{\boldsymbol{\theta}}\rangle, \tag{6.0.7}$$

where we used the notation:

$$|\partial_{\theta_j}\psi_{\boldsymbol{\theta}}\rangle = \frac{\partial}{\partial\theta_j}|\psi_{\boldsymbol{\theta}}\rangle. \tag{6.0.8}$$

6.1 The multiparametric quantum Cramér-Rao bound

The fundamental precision limit in single parameter estimation, set by the quantum Cramér-Rao bound, is also defined in the multiparameter framework. However, in the same spirit as for the QFI, the QCRB in multiparameter estimation is written in matrix form [60, 78]:

$$\mathbf{Cov}(\tilde{\boldsymbol{\theta}}) \geq \frac{1}{N}(\mathbf{F}_{\mathbf{x}}(\boldsymbol{\theta}))^{-1} \geq \frac{1}{N}(\mathbf{F}_Q(\boldsymbol{\theta}))^{-1}, \tag{6.1.1}$$

where N represents the number of independent repetitions of a measurement process carried out on the physical system, and where the covariance matrix is defined as [60]:

$$(\mathbf{Cov}(\tilde{\boldsymbol{\theta}}))_{ij} \equiv \mathrm{Cov}(\tilde{\theta}_i, \tilde{\theta}_j) = \mathbb{E}\left[(\tilde{\theta}_i - \mathbb{E}[\tilde{\theta}_i])(\tilde{\theta}_j - \mathbb{E}[\tilde{\theta}_j])\right], \tag{6.1.2}$$

where the diagonal elements correspond to the variance of the estimator $\tilde{\theta}_i$ by definition:

$$\mathrm{Var}(\tilde{\theta}_j) = \mathbb{E}\left[(\tilde{\theta}_i - \mathbb{E}[\tilde{\theta}_i])^2\right], \tag{6.1.3}$$

where for biased estimators, we have $\mathbb{E}[\tilde{\theta}_i] = \theta_i$ as a reminder. Hence, this matrix directly quantifies the correlations between the parameters and is linked to the QFIM by the quantum Cramér-Rao bound. In practice, we often use a weighted sum of the variances to find the total error. Hence, by defining a positive weight matrix $\mathbf{W}$ whose purpose is to quantify the relevance degree of the uncertainty of the various parameters in the specified problem, we can formulate the QCRB as [79]:

$$\mathrm{Tr}(\mathbf{W}\mathbf{Cov}(\tilde{\boldsymbol{\theta}})) \geq \mathrm{Tr}(\mathbf{W}(\mathbf{F}_Q(\boldsymbol{\theta}))^{-1}). \tag{6.1.4}$$

6.2 The incompatibility problem

A crucial problem that naturally arises in multiparameter estimation is the concept of incompatibility. Although the quantum Cramér Rao-bound defines the maximal theoretical precision achievable, in practice, the latter bound is not always reachable because the measurements that are optimal for estimating different parameters may be mutually incompatible. Indeed, in single parameter estimation, the optimal measurement is the measurement that diagonalizes the SLD and maximizes the classical Fisher information. The singular nature of this optimization problem avoids any conflict, as opposed to the multiparameter case. Indeed, suppose we want to estimate a vector quantity composed of M parameters θ_i. We can assign an operator $\hat{L}_i$ to each parameter and perform the measurement that diagonalizes this particular SLD to obtain the optimal measurement for the parameter θ_i. However, we cannot simultaneously diagonalize multiple SLDs if they do not commute with each other. For example [78]:

$$[\hat{L}_i, \hat{L}_j] \neq 0, \tag{6.2.1}$$

for a given index $i \neq j$, the optimal measurement for θ_i will irreparably destroy information about θ_j and vise versa, which is known as the *incompatibility problem*. A classic example of incompatibility in multiparameter estimation is vector magnetometry [78] using a single qubit. Suppose we want to estimate the cartesian components of a magnetic field $\mathbf{B} = (B_x, B_y, B_z)$. We prepare a qubit in a fixed $|\psi_0\rangle$ state. We consider the following unitary evolution after time t:

$$|\psi(B_x, B_y, B_z; t)\rangle = e^{-\frac{i}{2\hbar}t(B_x\hat{\sigma}_x + B_y\hat{\sigma}_y + B_z\hat{\sigma}_z)} |\psi_0\rangle . \tag{6.2.2}$$

For a very weak magnetic field, we can write this transformation as:

$$|\psi(B_x, B_y, B_z; t)\rangle = \left(\hat{\mathbb{1}} - \frac{it}{2\hbar}(B_x\hat{\sigma}_x + B_y\hat{\sigma}_y + B_z\hat{\sigma}_z)\right) |\psi_0\rangle . \tag{6.2.3}$$

Once evaluated at zero, the derivatives of this state with respect to the components of the magnetic field can be written as:

$$\frac{\partial}{\partial B_i} |\psi\rangle = -\frac{i}{2\hbar}\hat{\sigma}_i |\psi_0\rangle . \tag{6.2.4}$$

By defining $\hat{\rho} = |\psi\rangle \langle\psi|$, we can compute the SLD $\hat{L}_i$ using the differential equation:

$$\partial_{B_i}\hat{\rho} = \frac{1}{2}(\hat{\rho}\hat{L}_i + \hat{L}_i\hat{\rho}), \tag{6.2.5}$$

from which we deduce:

$$\hat{L}_i = 2\left(|\partial_{B_i}\psi\rangle \langle\psi| + |\psi\rangle \langle\partial_{B_i}\psi|\right). \tag{6.2.6}$$

Evaluating this expression at zero for the magnetic field yields:

$$\hat{L}_i = -\frac{i}{\hbar}[\hat{\sigma}_i, \hat{\rho}_0], \tag{6.2.7}$$

where $\hat{\rho}_0 = |\psi_0\rangle \langle\psi_0|$. Using the Bloch representation of the qubit on the Bloch sphere, we can write:

$$[\hat{\sigma}_i, \hat{\rho}_0] = -i(\mathbf{n} \times \hat{\boldsymbol{\sigma}})_i, \tag{6.2.8}$$

for any $\mathbf{n} \in \mathbb{R}^3$ with $|\mathbf{n}| = 1$. Hence, we deduce that the SLDs can be written as:

$$\hat{L}_i = -\frac{1}{\hbar}(\mathbf{n} \times \hat{\boldsymbol{\sigma}})_i. \tag{6.2.9}$$

In other words, the symmetric logarithmic derivatives associated with the cartesian components of the magnetic field are linear combinations of Pauli matrices, which are the generators of the *su(2)* algebra. We can choose for example $\mathbf{n} = (1, 0, 0)$ (which is equivalent to preparing the qubit initially in the $|+\rangle$ state), we get:

$$\hat{L}_x = 0, \qquad \hat{L}_y = -\frac{\hat{\sigma}_z}{\hbar}, \qquad \hat{L}_z = \frac{\hat{\sigma}_y}{\hbar}. \tag{6.2.10}$$

Owing to the commutation relations of the Pauli matrices, the SLD $\hat{L}_y$ and $\hat{L}_z$ do not commute. This non-commutativity directly leads to the incompatibility problem. Indeed, no single measurement can achieve the ultimate precision for all three components of the magnetic field simultaneously.

6.3 The quantum Holevo Cramér-Rao bound

As emphasized previously, the incompatibility problem that arises in multiparameter estimation represents an inevitable obstacle if one wishes to perform a measurement achieving the highest precision possible. Consequently, in such situations, the quantum Cramér-Rao bound may not be simultaneously achievable for all parameters in the problem considered. To remedy this central problem in the field of multiparameter estimation, Alexander Holevo introduced a new type of bound called the *Holevo Cramér-Rao bound (HCRB)*, which is based on scalar optimization for a given positive-definite weighting matrix. Indeed, for any unbiased estimator $\tilde{\boldsymbol{\theta}}$ and a weight matrix $\mathbf{W}$, the weighted trace of the covariance matrix is bounded by the Holevo bound [80]:

$$\mathrm{Tr}(\mathbf{W}\mathbf{Cov}(\tilde{\boldsymbol{\theta}})) \geq C_H(\mathbf{W}, \hat{\rho}(\tilde{\boldsymbol{\theta}})), \tag{6.3.1}$$

where the Holevo bound C_H is defined as [80–82]:

$$C_H(\mathbf{W}, \hat{\rho}(\tilde{\boldsymbol{\theta}})) = \min_{\hat{X}_1,\ldots,\hat{X}_M} \left[\mathrm{Tr}(\mathbf{W}\mathbf{A}(\hat{\mathbf{X}})) + \left|\left|\sqrt{\mathbf{W}}\mathbf{B}(\hat{\mathbf{X}})\sqrt{\mathbf{W}}\right|\right|\right], \tag{6.3.2}$$

where the norm in this definition denotes the trace norm (the sum of the absolute values of the eigenvalues), which mathematically penalizes the non-commutativity between the Hermitian operators $\hat{X}_j$ representing the estimator operators, on which we consider the optimization process. These operators satisfy the unbiasedness condition [77]:

$$\mathrm{Tr}\left(\frac{\partial\hat{\rho}}{\partial\theta_j}\hat{X}_k\right) = \delta_{jk}, \tag{6.3.3}$$

as well as:

$$\mathrm{Tr}\left(\hat{\rho}\hat{X}_j\right) = 0, \tag{6.3.4}$$

where we defined the matrices $\mathbf{A}(\hat{\mathbf{X}})$ and $\mathbf{B}(\hat{\mathbf{X}})$ as the real part and the imaginary part of the quantity [80]:

$$Z_{jk} = \mathrm{Tr}(\hat{\rho}\hat{X}_j\hat{X}_k), \tag{6.3.5}$$

which can be seen as the total quantum correlation matrix element between the estimation operators. Hence, we can write the real part as:

$$(\mathbf{A}(\hat{\mathbf{X}}))_{jk} = \mathrm{Re}(Z_{jk}) = \frac{1}{2}\mathrm{Tr}(\hat{\rho}\{\hat{X}_j\hat{X}_k\}), \tag{6.3.6}$$

which represents the classical variance and the imaginary part:

$$(\mathbf{B}(\hat{\mathbf{X}}))_{jk} = \mathrm{Im}(Z_{jk}) = \frac{1}{2i}\mathrm{Tr}(\hat{\rho}[\hat{X}_j\hat{X}_k]), \tag{6.3.7}$$

as the quantum incompatibility penalty. We are now able to establish a hierarchy between the precision bounds of multiparameter estimation. In fact, for any valid quantum measurement strategy, we have the following relation:

$$\mathrm{Tr}(\mathbf{W}\mathbf{Cov}(\tilde{\boldsymbol{\theta}})) \geq C_H(\mathbf{W}, \hat{\rho}(\tilde{\boldsymbol{\theta}})) \geq \mathrm{Tr}(\mathbf{W}(\mathbf{F}_Q(\boldsymbol{\theta}))^{-1}). \tag{6.3.8}$$

The Holevo bound appears as an intermediate bound compared to the QCRB unless the matrix $\mathbf{B}(\hat{\mathbf{X}})$ vanishes, indicating no apparent incompatibility. This can be done by checking that all SLDs commute for every index combination or by checking the weak commutativity (or average

compatibility) condition, which is less restrictive on the operators themselves due to the average imposed by the trace [78]:

$$\mathrm{Tr}(\hat{\rho}[\hat{L}_i, \hat{L}_j]) = 0. \tag{6.3.9}$$

At first glance, the Holevo bound appears as a more restrictive bound that will never surpass the QCRB. However, due to the incompatibility problem, the optimal measurement is often a mathematical mirage that cannot be reached in multi-parameter setups. On the other hand, the Holevo bound is always asymptotically achievable, since the latter remains valid even when optimal measurements for different parameters are incompatible, which offers a tremendous advantage on the practical aspect.

Conclusion

Throughout this master's thesis, we have studied parameter estimation in quantum metrology in the presence of noise, focusing in particular on spin rotation detection and spin squeezing in spin systems. We analyzed how different noise mechanisms lead to information loss and how this affects the estimation precision that can be achieved with spin-state probes, including in several ancilla-assisted single-parameter estimation protocols. Within this broader metrological framework, anticoherence is examined as a relevant intrinsic resource of spin systems (either as the probe or as the ancilla state), with the aim of clarifying how it influences noise robustness and the resulting metrological gain.

We began in Chapter 1 by reviewing the fundamental mathematical concepts underlying quantum mechanics, with a focus on the density operator framework. This formalism provides a convenient and rigorous description of quantum systems, particularly in scenarios where environmental coupling must be taken into account. In addition, we introduced the concept of linear maps, which constitute the mathematical foundation for the implementation of quantum channels in ancilla-assisted quantum protocols in Chapter 5.

In Chapter 2, we focused on spin systems, which provide the underlying framework for this work. We introduced fundamental concepts, including the standard angular momentum basis, alongside specific examples of spin states such as symmetric Dicke states and coherent states. These states are subsequently employed to construct mathematical tools within angular momentum theory, namely the Wigner-D matrix, the Majorana representation, and the Husimi Q function. These tools are extremely useful and serve two main purposes: they simplify complex expressions during the analytical derivation of the quantum Fisher information (QFI) in Chapter 5, and they offer excellent means to visualize the intrinsic symmetry of specific spin states. Finally, this chapter introduces the fundamental notion of anticoherent states, which represent highly non-classical isotropic states that serve as the natural counterpart to coherent states. This concept is further extended via t-anticoherence, complemented by a measure to quantify this property.

Chapter 3 provided a comprehensive overview of single-parameter estimation theory, formally defining fundamental precision scaling limits, specifically the standard quantum limit (SQL) and the Heisenberg limit (HL), alongside the mechanisms of parameter encoding in quantum states. Furthermore, we introduced three distinct methodologies for constructing an estimator of an unknown parameter θ encoded within the density operator of the investigated quantum system. Central concepts of quantum metrology are also covered, with special emphasis on the QFI and its mathematical properties, as well as the quantum Cramér-Rao bound, which dictates the fundamental limit of estimation precision.

Chapter 4 addressed noisy metrology, specifically analyzing the role of anticoherent states in rotation amplitude estimation and demonstrating that these states serve as optimal quantum rotosensors. Furthermore, to simulate environmental coupling in the ancilla-assisted quantum protocols presented in Chapter 5, two noise mechanisms were introduced: the depolarization channel, which represents a uniform source of white noise, and the dephasing channel, which induces directional

noise. Under the influence of these quantum channels, the optimal measurement was explicitly derived for both the Greenberger-Horne-Zeilinger (GHZ) state and the tetrahedron 2-anticoherent state within a rotation sensing protocol. Finally, we introduced the concept of sub-optimal measurement, which offers a experimentally viable alternative based on Husimi sampling that is easily implementable under realistic laboratory conditions, in contrast to the traditional approach used in optimal measurement, which relies in most of the cases in the projective measurement in highly entangled states (coming from the eigenvectors of the SLD).

Chapter 5 investigated both numerically and analytically ancilla-assisted protocols in noisy metrology, utilizing the GHZ state alongside a family of spin states that includes the tetrahedron state. By examining various configurations based on the stage at which noise occurs, we classified the scaling behavior of the QFI with respect to the system size N. This investigation revealed that anticoherent states constitute highly valuable resources to fight depolarization and dephasing, due to their non-classical nature and their rotation-preserving structure, a property we formalize by defining a criterion based on the anticoherence order t. The summary tables provided back up this observation and support the fact that anticoherent states serve as excellent probes in various quantum protocols. Furthermore, the optimal measurement was explored both analytically and numerically. In the latter case, we implemented the Maximum Likelihood Estimation (ML) method to quantify the sensitivity of the GHZ state when employed as a probe state in noisy, ancilla-assisted schemes.

Finally, Chapter 6 introduced the multiparameter estimation framework, naturally extending the estimation paradigm to a set of unknown parameters rather than a single physical quantity. Furthermore, we highlighted the parameter incompatibility problem that inherently arises when simultaneously estimating multiple quantities, as well as its limitations on estimation precision, as dictated by the Holevo quantum Cramér-Rao bound.

Ultimately, this work opens the way for future implementations of increasingly sophisticated quantum metrology protocols. Future research could, for instance, extend the ancilla-assisted protocols explored in this master's thesis to the multiparameter regime, thereby relating estimation precision to the quantum Holevo Cramér-Rao bound (HCRB) and possibly mapping the parameter incompatibility problem to anticoherence when utilizing these exotic spin states as a quantum resource. Furthermore, a broader range of noise mechanisms could be investigated by modeling additional distinct quantum channels acting on the qudit across multiple stages of the protocol. Finally, exploring increasingly larger spin-j systems could help establish a definitive link between higher orders of anticoherence and the resulting metrological gain.

Appendix A

Deriving Wigner's formula for the small d-matrix

In this section, we focus on deriving the explicit mathematical expression of the small Wigner d-matrix elements (2.3.5). There are various ways to write the coefficients of this matrix and various methods for deriving them in the literature. The proof given below is inspired by the formalism suggested by Sakurai and Napolitano [83]. The approach is based on *Julian Schwinger's boson (harmonic oscillator) representation* of angular momentum. The key idea is to introduce two independent harmonic oscillators with creation/annihilation operators $(\hat{a}, \hat{a}^\dagger)$ and $(\hat{b}, \hat{b}^\dagger)$, satisfying the usual bosonic commutation relations:

$$\begin{cases} [\hat{a}, \hat{a}^\dagger] = \hat{\mathbb{1}} \\ [\hat{b}, \hat{b}^\dagger] = \hat{\mathbb{1}} \end{cases} \qquad \begin{cases} [\hat{a}, \hat{b}^\dagger] = 0 \\ [\hat{b}, \hat{a}^\dagger] = 0 \end{cases} \tag{A.0.1}$$

In this framework, we rewrite the ladder operators $\hat{J}_\pm$ and $\hat{J}_z$ using these annihilation and creation operators according to :

$$\hat{J}_+ = \hbar \hat{a}^\dagger \hat{b}, \qquad \hat{J}_- = \hbar \hat{b}^\dagger \hat{a}, \qquad \hat{J}_z = \frac{\hbar}{2}(\hat{a}\hat{a}^\dagger - \hat{b}\hat{b}^\dagger). \tag{A.0.2}$$

The total boson number operator is defined as $\hat{N} = \hat{a}\hat{a}^\dagger + \hat{b}\hat{b}^\dagger$ and its eigenvalue N is related to the spin number j through $N = 2j$, defining the number of bosons. We are interested in computing the expression:

$$d^{(j)}_{m',m}(\beta) = \langle j, m' | \hat{R}_y(\beta) | j, m \rangle \,. \tag{A.0.3}$$

Using the creation and annihilation operators of both harmonic oscillators again, one can define the standard spin states as:

$$|j, m\rangle = \frac{(\hat{a}^\dagger)^{j+m} (\hat{b}^\dagger)^{j-m}}{\sqrt{(j+m)!(j-m)!}} |0\rangle \,, \tag{A.0.4}$$

where we defined the vacuum state $|0\rangle$ as $\hat{a}\,|0\rangle = \hat{b}\,|0\rangle = 0$. The d-matrix coefficients can therefore be written as:

$$d^{(j)}_{m',m}(\beta) = \frac{\langle 0 |\, \hat{a}^{j+m'} \hat{b}^{j-m'} \hat{R}_y(\beta) (\hat{a}^\dagger)^{j+m} (\hat{b}^\dagger)^{j-m} \hat{R}^\dagger_y(\beta) \hat{R}_y(\beta) \,| 0 \rangle}{\sqrt{(j+m')!(j-m')!(j+m)!(j-m)!}}. \tag{A.0.5}$$

Moreover, one can rewrite the rotation operator $\hat{R}_y(\beta) = e^{-\frac{i}{\hbar}\beta \hat{J}_y}$ according to the transformations of the ladder operators, owing to (2.2.6) and (A.0.2):

$$\hat{R}_y(\beta) = e^{-\frac{\beta}{2}(\hat{a}^\dagger \hat{b} - \hat{b}^\dagger \hat{a})}. \tag{A.0.6}$$

Using this operator, we can define the following transformations:

$$\hat{A}(\beta) = \hat{R}_y(\beta)\hat{a}^\dagger \hat{R}_y^\dagger(\beta), \qquad \hat{B}(\beta) = \hat{R}_y(\beta)\hat{b}^\dagger \hat{R}_y^\dagger(\beta). \tag{A.0.7}$$

Differentiating both relations with respect to the Euler angle β yields:

$$\frac{d\hat{A}(\beta)}{d\beta} = -\frac{i}{\hbar}\hat{R}_y(\beta)[\hat{J}_y, \hat{a}^\dagger]\hat{R}_y^\dagger(\beta), \qquad \frac{d\hat{B}(\beta)}{d\beta} = -\frac{i}{\hbar}\hat{R}_y(\beta)[\hat{J}_y, \hat{b}^\dagger]\hat{R}_y^\dagger(\beta). \tag{A.0.8}$$

Hence, we need to compute the following commutators:

$$[\hat{a}^\dagger \hat{b} - \hat{b}^\dagger \hat{a}, \hat{a}^\dagger] = -\hat{b}^\dagger, \qquad [\hat{a}^\dagger \hat{b} - \hat{b}^\dagger \hat{a}, \hat{b}^\dagger] = \hat{a}^\dagger. \tag{A.0.9}$$

Inserting both commutators in (A.0.8) yields two coupled differential equations:

$$\frac{d\hat{A}(\beta)}{d\beta} = \frac{1}{2}\hat{B}(\beta), \qquad \frac{d\hat{B}(\beta)}{d\beta} = -\frac{1}{2}\hat{A}(\beta). \tag{A.0.10}$$

We can solve both equations by writing the system:

$$\frac{d}{d\beta}\begin{pmatrix}\hat{A}\\ \hat{B}\end{pmatrix} = \begin{pmatrix}0 & \frac{1}{2}\\ -\frac{1}{2} & 0\end{pmatrix}\begin{pmatrix}\hat{A}\\ \hat{B}\end{pmatrix}, \tag{A.0.11}$$

together with the set of initial conditions $\hat{A}(0) = \hat{a}^\dagger$ and $\hat{B}(0) = \hat{b}^\dagger$. This leads us to the solutions:

$$\hat{A}(\beta) = \cos\left(\frac{\beta}{2}\right)\hat{a}^\dagger + \sin\left(\frac{\beta}{2}\right)\hat{b}^\dagger, \qquad \hat{B}(\beta) = -\sin\left(\frac{\beta}{2}\right)\hat{a}^\dagger + \cos\left(\frac{\beta}{2}\right)\hat{b}^\dagger. \tag{A.0.12}$$

which shows us that the pair of creation operators $(\hat{a}^\dagger, \hat{b}^\dagger)$ transform as a spinor under a SU(2) matrix. Using both operators and the unitary property of $\hat{R}_y(\beta)$, one can easily show that the following relation holds :

$$\hat{R}_y(\beta)(\hat{a}^\dagger)^{j+m}(\hat{b}^\dagger)^{j-m}\hat{R}_y^\dagger(\beta) = \hat{A}^{j+m}\hat{B}^{j-m} \tag{A.0.13}$$

For simplicity, let us define $c = \cos\left(\frac{\beta}{2}\right)$ and $s = \sin\left(\frac{\beta}{2}\right)$, as variables of the angle β where the dependence on β is implicit. (A.0.5) becomes :

$$d^{(j)}_{m',m}(\beta) = \frac{\langle 0|\, \hat{a}^{j+m'}\hat{b}^{j-m'}(c\hat{a}^\dagger + s\hat{b}^\dagger)^{j+m}(-s\hat{a}^\dagger + c\hat{b}^\dagger)^{j-m}\,|0\rangle}{\sqrt{(j+m')!(j-m')!(j+m)!(j-m)!}} \tag{A.0.14}$$

From this expression, it is clear that within the brackets, only the terms with a total power equal to $j+m$ and $j-m$ for $\hat{a}^\dagger$ and $\hat{b}^\dagger$, respectively, will survive according to:

$$\langle 0|\hat{a}^p\hat{b}^q(\hat{a}^\dagger)^{p'}(\hat{b}^\dagger)^{q'}|0\rangle = p!q!\delta_{p,p'}\delta_{q,q'}. \tag{A.0.15}$$

Hence, we can use the binomial theorem to compute explicitly the powers of $\hat{A}$ and $\hat{B}$:

$$(c\hat{a}^\dagger + s\hat{b}^\dagger)^{j+m} = \sum_{k=0}^{j+m} \binom{j+m}{k} c^k s^{j+m-k} (\hat{a}^\dagger)^k (\hat{b}^\dagger)^{j+m-k}, \tag{A.0.16}$$

$$(-s\hat{a}^\dagger + c\hat{b}^\dagger)^{j-m} = \sum_{l=0}^{j-m} \binom{j-m}{l} c^{j-m-l} (-s)^l (\hat{a}^\dagger)^l (\hat{b}^\dagger)^{j-m-l}. \tag{A.0.17}$$

Since the product of both series will be proportional to terms $(\hat{a}^\dagger)^{k+l}(\hat{b}^\dagger)^{2j-k-l}$, the two following equalities must therefore hold:

$$\begin{cases} k + l = j + m' \\ 2j - k - l = j - m' \end{cases} \tag{A.0.18}$$

which yields the condition $l = j + m' - k$. Since both of the two sums in the product of series are not independent, the numerator in (A.0.14) can be rewritten using the condition on index l and (A.0.15) as:

$$(j+m')!(j-m')! \sum_k (-1)^{j+m'-k} \binom{j-m}{j+m'-k} \binom{j+m}{k} c^{2k-m-m'} s^{2j-2k+m+m'}, \tag{A.0.19}$$

where the sum covers values of k such that none of the factorial terms are negative. By writing explicitly the binomial coefficients, we obtain an expression for the Wigner small d-matrix elements:

$$\begin{aligned} d^{(j)}_{m',m}(\beta) = {} & \sqrt{(j+m')!(j-m')!(j+m)!(j-m)!} \\ & \times \sum_k \frac{(-1)^{j+m'-k}}{(j+m'-k)!(k-m-m')!k!(j+m-k)!} c^{2k-m-m'} s^{2j-2k+m+m'}. \end{aligned} \tag{A.0.20}$$

In order to recover the exact expression given in (2.3.6), the last step consists of changing the summation index to $t = j + m - k$. In this way, by replacing the variables c and s with their respective trigonometric functions, we obtain the so-called Wigner formula for the elements of the small d-matrix:

$$\begin{aligned} d^{(j)}_{m',m}(\beta) = {} & \sum_{k=k_{\min}}^{k_{\max}} \frac{(-1)^{k-m+m'} \sqrt{(j+m)!(j-m)!(j+m')!(j-m')!}}{(j+m-k)!(j-k-m')!(k-m+m')!k!} \\ & \times \left(\cos\frac{\beta}{2}\right)^{2j-2k+m-m'} \left(\sin\frac{\beta}{2}\right)^{2k-m+m'}, \end{aligned} \tag{A.0.21}$$

where we renamed the summation index by k to match (2.3.6). The exact array of values covering the summation index can be deduced form the index relations and the binomial expansions that were introduced. Hence, one finds:

$$k_{min} = \max(0, m - m'), \qquad k_{max} = \min(j + m, j - m'). \tag{A.0.22}$$

Bibliography

[1] V. Giovannetti, S. Lloyd, and L. Maccone, Science **306**, 1330 (2004).

[2] A. Dey, S. Mouradian, C. Lupo, and Z. Huang, Physical Review Letters **135**, 130802 (2025).

[3] Y. Dong, C. Feng, S.-C. Zhang, Y. Zheng, X.-D. Chen, G.-C. Guo, and F.-W. Sun, Physical Review Applied **19**, 064022 (2023).

[4] R. Kaubruegger and A. M. Kaufman, arXiv preprint arXiv:2512.02202 (2025).

[5] L. Pezze, A. Smerzi, M. K. Oberthaler, R. Schmied, and P. Treutlein, Reviews of Modern Physics **90**, 035005 (2018).

[6] J. Broz, *Quantum metrology with trapped ions*, Ph.D. thesis, UC, Berkeley (main) (2023).

[7] R. J. Lewis-Swan, J. Z. Castro, D. Barberena, and A. M. Rey, Physical Review Letters **132**, 163601 (2024).

[8] S. Boixo, A. Datta, M. J. Davis, A. Shaji, A. B. Tacla, and C. M. Caves, Physical Review A—Atomic, Molecular, and Optical Physics **80**, 032103 (2009).

[9] N. Arunkumar, K. S. Olsson, J. T. Oon, C. A. Hart, D. B. Bucher, D. R. Glenn, M. D. Lukin, H. Park, D. Ham, and R. L. Walsworth, Physical Review Letters **131**, 100801 (2023).

[10] T. Kielinski, P. O. Schmidt, and K. Hammerer, Science Advances **10**, eadr1439 (2024).

[11] X.-X. Zhang, R.-G. Zhou, and W.-S. Xu, Chinese Journal of Electronics **34**, 1172 (2025).

[12] N. Shettell, arXiv preprint arXiv:2201.01523 (2022).

[13] Y. Winsten, D. Cohen, and Y. Sagi, Physical Review A **110**, 043308 (2024).

[14] Z.-Y. Zhou, S.-L. Liu, S.-K. Liu, Y.-H. Li, D.-S. Ding, G.-C. Guo, and B.-S. Shi, Physical Review Applied **7**, 064025 (2017).

[15] W. Jia, V. Xu, K. Kuns, M. Nakano, L. Barsotti, M. Evans, N. Mavalvala, R. Abbott, I. Abouelfettouh, R. Adhikari, *et al.*, arXiv e-prints , arXiv (2024).

[16] J. Martin, S. Weigert, and O. Giraud, Quantum **4**, 285 (2020).

[17] E. Serrano-Ensástiga, C. Chryssomalakos, and J. Martin, Physical Review A **111**, 022435 (2025).

[18] D. V. Vasilyev, A. Shankar, R. Kaubruegger, and P. Zoller, arXiv preprint arXiv:2404.14194 (2024).

[19] A. Z. Goldberg and D. F. James, Physical Review A **98**, 032113 (2018).

[20] J. B. Brask, R. Chaves, and J. Kołodyński, Physical Review X **5**, 031010 (2015).

[21] D. Lallemand, *Noisy quantum metrology with spins*, Master's thesis, Université de Liège (2025).

[22] E. Schrödinger, in *Mathematical proceedings of the cambridge philosophical society*, Vol. 31 (Cambridge University Press, 1935) pp. 555–563.

[23] M. M. Wilde, *Quantum information theory* (Cambridge university press, 2013).

[24] M. A. Nielsen and I. L. Chuang, *Quantum computation and quantum information* (Cambridge university press, 2010).

[25] B. C. Hiesmayr, C. Popp, and T. C. Sutter, International Journal of Quantum Information **23**, 2530003 (2025).

[26] O. Stern, Zeitschrift für Physik **7**, 249 (1921).

[27] H. Zhou, J. Choi, S. Choi, R. Landig, A. M. Douglas, J. Isoya, F. Jelezko, S. Onoda, H. Sumiya, P. Cappellaro, *et al.*, Physical review X **10**, 031003 (2020).

[28] Q. Cao, G. T. Genov, Y. Chu, J. Cai, Y. Liu, A. Retzker, and F. Jelezko, arXiv preprint arXiv:2506.20416 (2025).

[29] J. Huang, M. Zhuang, and C. Lee, Applied Physics Reviews **11** (2024).

[30] J. I. Cirac and P. Zoller, Physical review letters **74**, 4091 (1995).

[31] M. H. Devoret and J. M. Martinis, Quantum Information Processing **3**, 163 (2004).

[32] D. Loss and D. P. DiVincenzo, Physical Review A **57**, 120 (1998).

[33] D. Jaksch, J. I. Cirac, P. Zoller, S. L. Rolston, R. Côté, and M. D. Lukin, Physical Review Letters **85**, 2208 (2000).

[34] J. Denis, *Bridging concepts of quantumness: Phase-space, entanglement and anticoherence in spin systems*, Ph.D. thesis, Universite de Liege (Belgium) (2025).

[35] EscherMath, Möbius strip ii (red ants) (1963), artwork information page for M.C. Escher's 1963 woodcut.

[36] T.-L. Ho, Physical review letters **81**, 742 (1998).

[37] G. L. Stamokostas and G. A. Fiete, Physical Review B **97**, 085150 (2018).

[38] C. Cohen-Tannoudji, B. Diu, and F. Laloë, *Quantum Mechanics, Volume 1: Basic Concepts, Tools, and Applications*, 2nd ed. (Wiley-VCH, 2020).

[39] R. Krischek, C. Schwemmer, W. Wieczorek, H. Weinfurter, P. Hyllus, L. Pezzé, and A. Smerzi, Physical review letters **107**, 080504 (2011).

[40] R. H. Dicke, Physical review **93**, 99 (1954).

[41] O. Giraud, D. Braun, D. Baguette, T. Bastin, and J. Martin, Physical Review Letters **114**, 080401 (2015).

[42] D. Baguette, T. Bastin, and J. Martin, arXiv preprint arXiv:1407.1738 (2014).

[43] C. Marconi, G. Müller-Rigat, J. Romero-Pallejà, J. Tura, and A. Sanpera, Reports on Progress in Physics **89**, 024001 (2026).

[44] E. Wigner, Zeitschrift für Physik **43**, 624 (1927).

[45] E. Wigner, (1931).

[46] V. K. Khersonskii, A. N. Moskalev, and D. A. Varshalovich, *Quantum theory of angular momemtum* (World Scientific, 1988).

[47] H. E. Haber, Properties of the wigner d-matrices, Physics 215 Course Handout, University of California, Santa Cruz (2018), accessed: June 9, 2026.

[48] E. Majorana, Il Nuovo Cimento (1924-1942) **9**, 43 (1932).

[49] A. U. Devi, Sudha, and A. Rajagopal, Quantum Information Processing **11**, 685 (2012).

[50] J. Zimba, Electronic Journal of Theoretical Physics (2006).

[51] D. Baguette and J. Martin, Physical Review A **96**, 032304 (2017).

[52] D. Baguette, F. Damanet, O. Giraud, and J. Martin, Physical Review A **92**, 052333 (2015).

[53] R. Pereira and C. Paul-Paddock, Journal of Mathematical Physics **58**, 062107 (2017).

[54] J. Denis, C. Read, and J. Martin, SciPost Physics Core **9**, 001 (2026).

[55] J. Martin, Library of spin anticoherent states, http://www.oq.ulg.ac.be/libspinACstates.html (2024), accessed: 2026-06-08.

[56] A. Z. Goldberg, A. B. Klimov, M. Grassl, G. Leuchs, and L. L. Sánchez-Soto, AVS Quantum Science **2** (2020).

[57] J. Denis, T. Lacaille, J. Martin, and E. Serrano-Ensástiga, arXiv preprint arXiv:2605.29436 (2026).

[58] J. M. E. Fraisse, *New concepts in quantum-metrology: From coherent averaging to Hamiltonian extensions*, Ph.D. thesis, U. Tubingen (2018).

[59] G. Tóth and I. Apellaniz, Journal of Physics A: Mathematical and Theoretical **47**, 424006 (2014).

[60] A. Z Goldberg, A. B Klimov, G. Leuchs, and L. L Sánchez-Soto, Journal of Physics: Photonics **3**, 022008 (2021).

[61] M. Szczykulska, T. Baumgratz, and A. Datta, Advances in Physics: X **1**, 621 (2016).

[62] A. Candeloro, Z. Pazhotan, and M. G. Paris, Quantum Science and Technology **9**, 045045 (2024).

[63] R. Demkowicz-Dobrzański, J. Kołodyński, and M. Guţă, Nature communications **3**, 1063 (2012).

[64] M. G. Paris, International Journal of Quantum Information **7**, 125 (2009).

[65] M. Fadel, N. Roux, and M. Gessner, Reports on Progress in Physics **88**, 106001 (2025).

[66] B.-Y. Go, G. Gwak, Y.-D. Yoon, S. Lee, N. Treps, J. Park, and Y.-S. Ra, Optics Express **34**, 17346 (2026).

[67] Y. Li, L. Pezzè, M. Gessner, Z. Ren, W. Li, and A. Smerzi, Entropy **20**, 628 (2018).

[68] J. Liu, X.-X. Jing, W. Zhong, and X.-G. Wang, Communications in Theoretical Physics **61**, 45 (2014).

[69] S. Akhtarshenas, Journal of Physics A: Mathematical and Theoretical **40**, 11333 (2007).

[70] C. Invernizzi, M. Korbman, L. Campos Venuti, and M. G. Paris, Physical Review A—Atomic, Molecular, and Optical Physics **78**, 042106 (2008).

[71] B. Escher, R. L. de Matos Filho, and L. Davidovich, Nature Physics **7**, 406 (2011).

[72] Y. Chen, Z. Wang, and S. Zhou, arXiv preprint arXiv:2605.08341 (2026).

[73] H. A. Loughlin, M. A. Guidry, J. Ding, M. Ono, M. L. Gall, B. Lou, E. Oelker, X. Yin, V. Sudhir, and N. Mavalvala, arXiv preprint arXiv:2509.25384 (2025).

[74] C. Zhang, P. Yu, A. Jadbabaie, and N. R. Hutzler, Physical Review Letters **131**, 193602 (2023).

[75] T. Konrad, A. Rouillard, M. Kastner, and H. Uys, Physical Review A **104**, 052614 (2021).

[76] Z. Bao and D. F. James, arXiv preprint arXiv:2605.24108 (2026).

[77] C. Shoukang, M. G. Genoni, and F. Albarelli, Communications Physics (2026).

[78] J. Liu, H. Yuan, X.-M. Lu, and X. Wang, Journal of Physics A: Mathematical and Theoretical **53**, 023001 (2020).

[79] G. Bressanini, M. G. Genoni, M. Kim, and M. G. Paris, Journal of Physics A: Mathematical and Theoretical **57**, 315305 (2024).

[80] S. Razavian, M. G. Paris, and M. G. Genoni, Entropy **22**, 1197 (2020).

[81] M. Zhou, H. Ma, L. Chen, W. Zhang, and C.-H. Yuan, arXiv preprint arXiv:2502.02855 (2025).

[82] F. Albarelli, J. F. Friel, and A. Datta, arXiv preprint arXiv:1906.05724 (2019).

[83] J. J. Sakurai and J. Napolitano, *Modern quantum mechanics* (Cambridge university press, 2020).